

# Removal Mechanisms of Protective Iron Carbonate Layer in Flowing Solutions

A dissertation presented to  
the faculty of  
the Russ College of Engineering and Technology of Ohio University

In partial fulfillment  
of the requirements for the degree  
Doctor of Philosophy

Yang Yang

August 2012

© 2012 Yang Yang. All Rights Reserved.

This dissertation titled  
Removal Mechanisms of Protective Iron Carbonate Layer in Flowing Solutions

by  
YANG YANG

has been approved for  
the Department of Chemical and Biomolecular Engineering  
and the Russ College of Engineering and Technology by

---

Srdjan Nesic

Professor of Chemical and Biomolecular Engineering

---

Dennis Irwin

Dean, Russ College of Engineering and Technology

## ABSTRACT

YANG, YANG, Ph.D., August 2012, Chemical Engineering

### Removal Mechanisms of Protective Iron Carbonate Layer in Flowing Solutions

Director of Dissertation: Srdjan Nestic

In the oil and gas industry, internal corrosion of carbon steel pipelines is commonly encountered during production and transportation. Iron carbonate is the main corrosion product layer in a CO<sub>2</sub> corrosion environment. The formation of a protective iron carbonate layer can protect the steel from further corrosion by acting as a diffusion barrier and also by covering portions of the steel surface. Partial removal of the protective iron carbonate layer can lead to severe localized corrosion by the galvanic effect established between layer-covered and layer-free areas. Therefore, it is very important to understand the mechanisms of protective iron carbonate layer removal. In the current study, two possible removal mechanisms were examined by experimental studies: mechanical removal by flow and chemical removal by dissolution.

Three types of experimental setups were used in order to examine whether the protective iron carbonate layer could be removed by flow. Small scale experiments were conducted in a glass cell with a rotating cylinder electrode setup and jet impingement setup. Although two different types of flow pattern were used, results showed that the protective iron carbonate layer was not affected by the flow and a thin yet adherent layer remained on the steel surface and protected the steel from corrosion. Furthermore, a medium scale thin channel flow cell system was designed and constructed, in order to conduct tests under more realistic flow conditions. It was once again proven that the iron

carbonate layer remained protective under the enhanced flow condition. In addition, the mechanical strength of the protective layer was characterized in tensile strength experiments. It appeared that the measured strength necessary to separate the protective iron carbonate layer from the steel substrate was on the order of  $10^6$  Pa. This value was a few orders of magnitude higher than the wall shear stress encountered in most realistic flow systems, which demonstrated that with only mechanical force exerted by flow, the protective iron carbonate layer cannot be damaged.

A qualitative study of iron carbonate dissolution was made using scanning electron microscopy. It was shown that the dissolution of the iron carbonate layer led to exposure of the underlying steel. Plate shaped iron carbonate was dissolved preferably as compared to prism shaped iron carbonate. Chemical dissolution of the protective iron carbonate layer was first tested in a glass cell with a rotating cylinder electrode setup. It was observed that the corrosion rate of the underlying steel increased as a consequence of the dissolution of the protective iron carbonate layer due to exposure to an under-saturated solution. With the capability of in situ measurement of mass change on the surface, the electrochemical quartz crystal microbalance was employed in the current study to monitor the iron carbonate dissolution rate directly. Quartz crystals coated with iron, gold and platinum were used. Finally a dissolution mechanism of iron carbonate was proposed.

Approved: \_\_\_\_\_

Srdjan Nesic

Professor of Chemical and Biomolecular Engineering

**DEDICATION**

*To*

*My parents, Shichun Yang and Guizhen Yang*

*My husband, Xuanping Tang*

*and all other family members*

*For their*

*Love, care and support*

## ACKNOWLEDGMENTS

I would like to express my sincere gratitude to my academic advisor, Dr. Srdjan Nesic, who guided me through the entire PhD program. He not only encouraged me to pursue a more challenging goal when I made good progress, but also supported me when I was going through a tough time in my research. Dr. Nesic was also a mentor in my life and he was always there when I needed help and advice. I became more professional and mature after working with him during the past few years of my PhD.

I would like to thank Mr. Bruce Brown, my project leader, for offering me a lot of support and advice in my research work. No matter how busy he was, he was always patient and tried to help me as much as he could. Great thanks go to Dr. Yoon-Seok Choi, Dr. David Young and Dr. Fernando Farelas. My research benefited greatly from my discussions with them. My appreciation also extends to Dr. Michael Prudich, Dr. Khairul Alam, Dr. Lauren McMills and Dr. David Ingram for reviewing my dissertation and serving on my PhD committee.

I would like to acknowledge Mr. Albert Schubert, Mr. Danny Cain, Mr. Cody Shafer, Mr. Steve Upton and Mr. Phil Bullington for their assistance in my experimental work. I also want to thank all the current and former fellow students, post-docs and visiting scholars for their kind support. They created a very friendly environment in the institute and I spent a wonderful time with them.

The support from all the staff at Venezia Tecnologie is also greatly appreciated. Special thanks go to Dr. Bernardo Molina, Ms. Maria Elena Gennaro, Mr. Marino

Battagliarin, Mr. Pier Paolo Zonta and Mr. Alessandro Cafissi for their support and contribution to this project.

My appreciation also goes to Mr. Richard Woollam, Dr. Durnie William, Mr. Jon Rogers and Dr. Hui Li for their supervision, guidance and support during my internship at BP America. Mr. Richard Woollam also contributed to my PhD project by providing valuable ideas and advice through our discussions.

Last but not least, I would like to acknowledge all the sponsoring companies for their financial support during my PhD work, which was part of the Corrosion Center Joint Industry Project (CC-JIP) at the Institute for Corrosion and Multiphase Technology.

**TABLE OF CONTENTS**

	Page
Abstract .....	3
Dedication .....	5
Acknowledgments.....	6
List of Tables .....	11
List of Figures .....	12
Chapter 1: Introduction.....	18
Chapter 2: Literature review .....	21
2.1 Carbon dioxide corrosion.....	21
2.1.1 Carbon dioxide corrosion mechanism .....	21
2.1.2 Factors influencing CO <sub>2</sub> corrosion.....	24
2.1.3 CO <sub>2</sub> corrosion modeling .....	26
2.2 Iron carbonate layer formation .....	27
2.2.1 Iron carbonate layer formation mechanism .....	27
2.2.2 Factors influencing iron carbonate layer formation.....	30
2.2.3 Iron carbonate precipitation kinetics.....	32
2.3 Mechanisms of protective iron carbonate layer removal.....	36
2.3.1 Mechanical removal mechanism.....	37
2.3.2 Chemical removal mechanism.....	42
Chapter 3: Research objectives.....	45
Chapter 4: Mechanical effect of flow on protective iron carbonate layer .....	47
4.1 Introduction.....	47

	9
4.2 Tests done in a glass cell with rotating cylinder electrode setup.....	48
4.2.1 Experimental method.....	48
4.2.2 Results and discussion.....	53
4.3 Tests done in a glass cell with jet impingement setup.....	57
4.3.1 Experimental method.....	57
4.3.2 Results and discussion.....	61
4.4 Tests done in the thin channel flow cell system.....	79
4.4.1 Experimental method.....	79
4.4.2 Results and discussion.....	84
4.5 Mechanical properties of the protective iron carbonate layer.....	88
4.5.1 Experimental method.....	88
4.5.2 Results and discussion.....	92
4.6 Discussion.....	104
4.7 Summary.....	105
Chapter 5: Chemical dissolution of protective iron carbonate layer.....	107
5.1 Introduction.....	107
5.2 Qualitative study of iron carbonate dissolution using SEM.....	107
5.2.1 Experimental method.....	107
5.2.2 Results and discussion.....	109
5.3 Iron carbonate formation and dissolution in a glass cell with a rotating cylinder electrode setup.....	116
5.3.1 Experimental method.....	116

	10
5.3.2 Results and discussion .....	117
5.4 Iron carbonate layer formation and dissolution in a glass cell with an electrochemical quartz crystal microbalance and a jet impingement setup.....	121
5.4.1 Calibration of electrochemical quartz crystal microbalance.....	121
5.4.2 Iron carbonate layer formation and dissolution on an iron coated quartz crystal .....	132
5.4.3 Iron carbonate layer formation and dissolution on a gold coated quartz crystal .....	141
5.4.4 Iron carbonate layer formation and dissolution on a platinum coated quartz crystal.....	150
5.5 Proposed mechanism of iron carbonate layer dissolution .....	160
5.6 Summary.....	165
Chapter 6: Conclusions and future work .....	166
6.1 Conclusions.....	166
6.2 Recommendations for future work .....	167
References.....	168
Appendix A: Additional tests of mechanical effect of flow conducted with rotating cylinder electrode.....	178
Appendix B: Additional tests of mechanical effect of flow conducted with quartz crystal microbalance and jet impingement.....	184

## LIST OF TABLES

	Page
Table 1. Equations for iron carbonate precipitation rate prediction (Sun, 2006). .....	34
Table 2. Comparison of estimated and measured mechanical properties of iron carbonate scales (Schmitt, et al., 1999). .....	39
Table 3. Text matrix for iron carbonate layer formation on carbon steel specimen. ....	51
Table 4. Chemical composition (wt%) of C1018. ....	51
Table 5. Text matrix for iron carbonate layer formation and removal in a glass cell with jet impingement setup. ....	60
Table 6. Text matrix for iron carbonate layer formation and removal in TCFC system. .	83
Table 7. Chemical composition of X65 steel (wt%).....	83
Table 8. Test matrix for layer formation test. ....	91
Table 9. Chemical composition of X52 and X65 steel (wt%). ....	91
Table 10. Text matrix for qualitative study of iron carbonate layer dissolution using SEM. ....	108
Table 11. Text matrix for iron carbonate layer dissolution in a glass cell with a rotating cylinder electrode setup. ....	117
Table 12. Test matrix for EQCM calibration.....	123
Table 13. Test matrix for the iron carbonate layer formation and dissolution on polished iron coated quartz crystal. ....	135
Table 14. Test matrix for iron carbonate layer formation and dissolution on a gold coated quartz crystal. ....	141
Table 15. Test matrix for the iron carbonate layer formation and dissolution on a platinum coated quartz crystal. ....	151
Table 16 Test matrix for layer formation and removal tests.....	179
Table 17. Test matrix for layer formation and removal test with iron coated quartz crystal. ....	185

## LIST OF FIGURES

	Page
Figure 1. Different stability regions of compound AB (Lasaga, 1998).....	29
Figure 2. Comparison of iron carbonate precipitation rate predictions from different authors at 80°C, using $A_s/V=1$ .....	35
Figure 3. Schematic illustration of the interaction between corrosion rate and solution saturation level (Dugstad, 1992).....	43
Figure 4. Schematic of glass cell with rotating cylinder electrode setup.....	50
Figure 5. Change of corrosion rate and supersaturation level during iron carbonate layer formation and mechanical removal test in glass cell with rotating cylinder electrode setup, layer formation: pH 6.6, 80°C, initial SS=300, stagnant; layer removal: pH 6.6, initial SS=4, 7000 rpm. ....	54
Figure 6. SEM images of specimen surface before and after mechanical removal test of iron carbonate layer in glass cell with rotating cylinder electrode setup, layer formation: pH 6.6, 80°C, initial SS=300, stagnant; layer removal: pH 6.6, initial SS=4, 7000 rpm..	56
Figure 7. Schematic of a glass cell with jet impingement setup (courtesy of Cody Shafer). .....	59
Figure 8. Change of corrosion rate and corrosion potential during layer formation and mechanical removal test in glass cell with jet impingement setup, layer formation: 80°C, pH 6.6, initial SS=300, stagnant, layer removal: pH 6.6, jet velocity 1.3 m/s. ....	62
Figure 9. SEM images taken after on specimen surface after iron carbonate layer formation, pH 6.6, 1 wt% NaCl, initial SS=300, 80°C, stagnant.....	63
Figure 10. Schematic illustration of hydrodynamic flow region of impinging jet distributed on specimen surface (Dawson & Shih, 1987).....	64
Figure 11. SEM images taken on carbon steel specimen surface after layer removal under jet impingement (wall jet region), pH 6.6, 1 wt% NaCl, initial SS=300, 80°C, jet flow velocity 1.3 m/s.....	66
Figure 12. SEM images taken on carbon steel specimen surface after layer removal under jet impingement (transition region), pH 6.6, 1 wt% NaCl, initial SS=300, 80°C, jet flow velocity 1.3 m/s.....	67
Figure 13. Corrosion rate and corrosion potential change of carbon steel sample under jet impingement, pH 6.6, 1 wt% NaCl, initial SS=300, jet flow rate 10.6 m/s, 80°C.....	68
Figure 14. SEM pictures taken after layer formation on carbon steel specimen surface. pH 6.6, 1 wt% NaCl, initial SS=300, 80°C, stagnant. ....	69
Figure 15. SEM and EDS images taken after layer removal under jet impingement on carbon steel specimen surface (wall jet region). pH 6.6, 1 wt% NaCl, initial SS=300, 80°C, jet flow velocity 10.6 m/s.....	71
Figure 16. SEM images taken after layer removal under jet impingement on carbon steel specimen surface (transition region). pH 6.6, 1 wt% NaCl, initial SS=300, 80°C, jet flow velocity 10.6 m/s.....	72
Figure 17. Corrosion rate and corrosion potential change of carbon steel sample under jet impingement, pH 7.0, 1 wt% NaCl, initial SS=0, jet flow rate 10.6 m/s, 80°C.....	74

Figure 18. SEM and EDS pictures taken before layer removal under jet impingement on carbon steel sample surface. pH 7.0, 1 wt% NaCl, initial SS=0, jet flow rate 10.6 m/s, 80°C.....	75
Figure 19. SEM and EDS images taken after layer removal under jet impingement on carbon steel sample surface. pH 7.0, 1 wt% NaCl, initial SS=0, jet flow rate 10.6 m/s, 80°C.....	76
Figure 20. SEM of cross section taken before layer removal under jet impingement on carbon steel sample surface. pH 7.0, 1 wt% NaCl, initial SS=0, jet flow rate 10.6 m/s, 80°C. “BEC” stands for backscattered electron beam. A secondary electron beam was used in all other images when it was not pointed out specifically.....	77
Figure 21. SEM images of cross section taken after layer removal under jet impingement on carbon steel specimen surface, pH 7.0, 1 wt% NaCl, initial SS=0, jet flow rate 10.6 m/s, 80°C.....	79
Figure 22. Flow chart of thin channel flow cell system.....	80
Figure 23. Schematic of assembled and exploded view of thin channel flow cell system test section.....	82
Figure 24. Change of corrosion rate and corrosion potential during the iron carbonate layer formation and mechanical removal test in TCFC, 80°C, pH 6.6, 1 wt% NaCl, initial SS=300, wall shear stress of flow 21 Pa. ....	86
Figure 25. SEM images of specimen surface before and after layer removal at 21 Pa, pH 6.6, 1 wt% NaCl, 80°C.....	87
Figure 26. Schematic of glass cell set-up for layer formation for mechanical property test of iron carbonate. ....	89
Figure 27. Mechanical strength test set-up with tensile machine. ....	90
Figure 28. Change of corrosion potential during iron carbonate layer formation process, 1 wt% NaCl, 80°C, pH 6.6, initial SS of FeCO <sub>3</sub> =300, applied anodic current=0.86 A/m <sup>2</sup> . ....	93
Figure 29. SEM images of surface (a, b) and cross sections (c, d) of the iron carbonate layer.....	94
Figure 30. Surfaces of stainless steel stud after adhesive strength test of adhesive F. ....	95
Figure 31. Cross section of iron carbonate layer with adhesive before mechanical strength test.....	96
Figure 32. Mechanical strength of iron carbonate layer on a carbon steel substrate for the case in which less than 10% of the iron carbonate failed. ....	97
Figure 33. SEM images of the sample surface after the test in which less than 10% of the iron carbonate failed (light grey areas). ....	98
Figure 34. SEM images of the stud surface after the test in which less than 10% of the iron carbonate failed (light grey areas). ....	98
Figure 35. Mechanical strength of iron carbonate layer on a carbon steel substrate for the case in which 10% - 50% of the iron carbonate surface failed.....	99
Figure 36. SEM images of the sample surface after the test in which 10% - 50% of the iron carbonate failed (light grey areas). ....	99
Figure 37. SEM images of the stud surface after the test in which 10% - 50% of the iron carbonate failed (light grey areas). Images (a) and (b) are from different locations on the stud surface. ....	100

Figure 38. Mechanical strength of iron carbonate layer on a carbon steel substrate for the case in which more than 50% of the iron carbonate surface failed. ....	101
Figure 39. SEM images of the sample surface after the test in which more than 50% of the iron carbonate failed (darker gray areas), showing small portions where the iron carbonate detached from the steel (lighter gray areas). ....	102
Figure 40. SEM images of the stud surface after the test in which more than 50% of the iron carbonate failed, showing iron carbonate detached from the sample.....	102
Figure 41. Cross section SEM images of the sample after the test in which more than of the iron carbonate failed, taken at a location where iron carbonate “broke”.....	103
Figure 42. SEM images of the specimen surface after layer formation at pH 6.6, 1 wt% NaCl, at 80°C, initial SS=300. ....	110
Figure 43. SEM image (X1000 BEC) of the specimen surface after iron carbonate dissolution by the first droplet of pH 2.0 test solution.....	110
Figure 44. SEM images of the specimen surface after iron carbonate dissolution by the second droplet of test solution with pH 2.0. ....	111
Figure 45. SEM images of the specimen surface after iron carbonate dissolution by the third droplet of test solution with pH 2.0.....	112
Figure 46. SEM and EDS images of the specimen surface after iron carbonate layer formation at pH 6.6, 1 wt% NaCl and 80°C. ....	113
Figure 47. SEM images of the specimen surface after dissolution by pH 3.8 test solution for 5 minutes. ....	113
Figure 48. SEM and EDS images of the specimen surface after dissolution by pH 3.8 test solution for 15 hours. ....	115
Figure 49. Change of corrosion rate and corrosion potential during iron carbonate layer formation (pH 6.6, initial S=300, stagnant) and dissolution (pH 5.6, initial S=0.3, 100 rpm) in 1 wt% NaCl at 80°C. Test was conducted with RCE glass cell setup. ....	118
Figure 50. SEM images of the iron carbonate layer before (pH 6.6, initial S=300, stagnant) and after dissolution (pH 5.6, initial S=0.3, 100 rpm) in 1 wt% NaCl at 80°C. Test was conducted with RCE glass cell setup.....	120
Figure 51. EQCM device (QCM200 from Stanford Research Systems).....	122
Figure 52. Quartz crystal coated with gold.....	122
Figure 53. Glass cell setup with EQCM (courtesy of Cody Shafer).....	123
Figure 54. Signal change of EQCM when exposed to 1 wt% NaCl (5 MHz, gold coated quartz crystal, 25°C).....	125
Figure 55. Signal change of EQCM when exposed to 1 wt% NaCl (5 MHz, gold coated quartz crystal, 80°C).....	126
Figure 56. Signal change of EQCM when exposed to 1 wt% NaCl without electrochemical measurement (5 MHz, 0.5 μm iron coated quartz crystal, 25°C). ....	127
Figure 57. EDS analysis of the iron (0.5 μm) coated quartz crystal after corrosion test. ....	128
Figure 58. Mass change of the iron coated quartz crystal when controlled by galvanostatic current (1 wt% NaCl, 25°C).....	129
Figure 59. Mass change of the iron coated quartz crystal when exposed to 1 wt% NaCl solution at 80°C.....	130

Figure 60. Mass change of the iron coated quartz crystal when controlled by galvanostatic corrosion at 80°C.....	130
Figure 61. Iron carbonate precipitation on the iron coated quartz crystal surface at pH 6.6, initial SS=0, 80°C, 1 wt% NaCl solution.....	131
Figure 62. SEM analysis of the iron carbonate layer formed on iron coated quartz crystal at pH 6.6, initial S=0, 80°C, 1 wt% NaCl solution. ....	132
Figure 63. Schematic of the glass cell setup with QCM and jet impingement (courtesy of Cody Shafer).....	134
Figure 64. Iron carbonate precipitation on an iron coated quartz crystal surface at pH 6.6, initial SS=600, 80°C, 1 wt% NaCl solution.....	137
Figure 65. SEM analysis of the iron carbonate film formed on an iron coated quartz crystal at pH 6.6, initial SS=120, 80°C, 1 wt% NaCl solution. ....	138
Figure 66. SEM analysis of the iron carbonate layer formed on carbon steel at pH 6.6, initial SS=300, 80°C, 1 wt% NaCl solution.....	138
Figure 67. Mass change of the iron crystal monitored by EQCM in layer formation and dissolution test under jet impingement, pH 6.6, initial SS=300, dissolution pH 5.8, 80°C, 1 wt% NaCl, jet velocity 1.3 m/s. ....	139
Figure 68. Change of corrosion rate and corrosion potential of the iron coated quartz crystal in iron carbonate layer formation and dissolution test under jet impingement, pH 6.6, initial SS=300, dissolution pH 5.8, 80°C, 1 wt% NaCl. ....	140
Figure 69. Iron carbonate precipitation on a gold coated quartz crystal at pH 6.6, initial SS=900, 80°C, 1 wt% NaCl solution. ....	142
Figure 70. SEM analysis of the iron carbonate layer formed on a gold coated quartz crystal at pH 6.6, initial SS=900, 80°C, 1 wt% NaCl solution. ....	143
Figure 71. EDS analysis of the iron carbonate layer formed on a gold coated quartz crystal at pH 6.6, initial SS=900, 80°C, 1 wt% NaCl solution. ....	143
Figure 72. Iron carbonate precipitation on polarized (-1000 mV) gold coated quartz crystal surface at pH 6.6, initial SS=900, 80°C, 1 wt% NaCl solution.....	144
Figure 73. SEM analysis of specimen surface after layer formation on polarized (-1000 mV) gold coated quartz crystal at pH 6.6, initial SS=900, 80°C, 1 wt% NaCl solution. ....	145
Figure 74. EDS analysis of the layer formed on a polarized (-1000 mV) gold coated quartz crystal surface at pH 6.6, initial SS=900, 80°C, 1 wt% NaCl solution.....	145
Figure 75. Iron carbonate precipitation on polarized (-700 mV) gold coated quartz crystal surface at pH 6.6, initial SS=120, 80°C, 1 wt% NaCl solution. ....	146
Figure 76. SEM analysis of the iron carbonate layer formed on a polarized gold coated quartz crystal at pH 6.6, initial SS=120, 80°C, 1 wt% NaCl solution. ....	147
Figure 77. EDS analysis of iron carbonate layer formed on polarized gold coated quartz crystal surface at pH 6.6, initial SS=120, 80°C, 1 wt% NaCl solution.....	147
Figure 78. Iron carbonate precipitation on a polarized (-700 mV) gold coated quartz crystal surface at pH 6.6, initial SS=900, 80°C, 1 wt% NaCl solution.....	148
Figure 79. SEM analysis of an iron carbonate film formed on a polarized gold coated quartz crystal at pH 6.6, initial SS=900, 80°C, 1 wt% NaCl solution. ....	148

Figure 80. Mass change of the gold crystal monitored by EQCM in film formation and dissolution test under jet impingement, jet velocity 1.3 m/s, pH 6.6, initial SS=300, dissolution pH 5.5 and pH 5.0, 80°C, 1 wt% NaCl.....	150
Figure 81. Blank surface of unpolished platinum coated quartz crystal at X1000. ....	153
Figure 82. Mass change of platinum quartz crystal monitored by EQCM during prism shaped iron carbonate layer formation test, pH 6.6, initial SS=300, 80°C, polarized at -700 mV, 1 wt% NaCl, stagnant. Polarization was started before additional ferrous ion was added to the solution.....	154
Figure 83. SEM images of specimen surface after prism shaped iron carbonate layer formation on platinum quartz crystal, pH 6.6, initial SS=300, 80°C, polarized at -700 mV, 1 wt% NaCl, stagnant. Polarization was started before additional ferrous ion was added to the solution.....	154
Figure 84. Mass change of platinum-coated quartz crystal monitored by EQCM for plate shaped iron carbonate layer formation test, pH 6.6, initial SS=300, polarized at -700 mV, 80°C, 1 wt% NaCl. Polarization was started after additional ferrous ion was added to the solution.....	155
Figure 85. SEM images of specimen surface after plate shaped iron carbonate layer formation on platinum coated quartz crystal, pH 6.6, initial SS=300, polarized at -700 mV, 80°C, 1 wt% NaCl. Polarization was started after additional ferrous ion was added to the solution.....	156
Figure 86. Mass change of the platinum quartz crystal monitored by EQCM in prism shaped iron carbonate layer formation and dissolution test, layer formation pH 6.6, initial SS=300, layer dissolution pH 5.0~5.5, 80°C, 1 wt% NaCl, jet flow rate 1.3 m/s. ....	158
Figure 87. SEM and EDS images of the specimen surface after prism shaped iron carbonate formation and dissolution on platinum-coated quartz crystal, layer formation: pH 6.6, initial SS=300, layer dissolution: pH 5.0~5.5, 80°C, 1 wt% NaCl, jet flow rate 1.3 m/s.....	159
Figure 88. Mass change of the platinum-coated quartz crystal monitored by EQCM for plate shaped iron carbonate layer formation and dissolution test, layer formation pH 6.6, initial SS=300, film dissolution pH 5.0~5.5, 80°C, 1 wt% NaCl, jet flow rate 1.3 m/s. ....	160
Figure 89. Dissolution rate change versus saturation level of iron carbonate as monitored by EQCM with platinum coated quartz crystal. Jet velocity for dissolution of prism shaped crystal was 2.0 m/s, 1.3 m/s and 0.6 m/s respectively. Jet velocity for dissolution of plate shaped crystal was 1.3 m/s.....	161
Figure 90. Dissolution rate change versus saturation level of iron carbonate as monitored by EQCM with platinum coated quartz crystal.....	164
Figure 91. Change of corrosion rate and corrosion potential during protective iron carbonate layer formation and mechanical removal test, layer formation: initial pH 6.3, initial SS=300, stagnant; layer removal: initial pH 6.1, initial SS=2, 1000 rpm, T=80°C, pCO <sub>2</sub> =0.53 bar, 1 wt% NaCl. ....	180
Figure 92. SEM images of top view of iron carbonate layer before and after removal process, layer formation: initial pH 6.3, initial SS=300, stagnant; layer removal: initial pH 6.1, initial SS=2, 1000 rpm, T=80°C, pCO <sub>2</sub> =0.53 bar, 1 wt% NaCl. ....	182

- Figure 93. SEM images of cross section of iron carbonate layer before and after removal process, layer formation: initial pH 6.3, initial SS=300, stagnant; layer removal: initial pH 6.1, initial SS=2, 1000 rpm, T=80°C, pCO<sub>2</sub>=0.53 bar, 1 wt% NaCl. .... 183
- Figure 94. Mass change during iron carbonate layer formation and removal test with EQCM and jet impingement, layer formation: pH 6.6, initial SS=300; layer removal: pH 6.6, slightly supersaturated, jet velocity 4.7 m/s. .... 186
- Figure 95. Change of corrosion rate and corrosion potential during iron carbonate layer formation and removal test with EQCM and jet impingement, layer formation: pH 6.6, initial SS=300; layer removal: pH 6.6, slightly supersaturated, jet velocity 4.7 m/s. .... 187
- Figure 96. EDS analysis of quartz crystal surface after iron carbonate layer formation and removal test with EQCM and jet impingement, layer formation: pH 6.6, initial SS=300; layer removal: pH 6.6, slightly supersaturated, jet velocity 4.7 m/s. .... 188

## CHAPTER 1: INTRODUCTION

Corrosion is defined as the degradation of metal due to its interaction with the environment. Corrosion is commonly encountered in our daily life, such as the rusting of a piece of steel. Without caution, corrosion can be severe and lead to catastrophic disasters. This is especially true during the production and transportation process in the oil and gas industry. From 1977-2007, among the 50 major engineering failures in the oil and gas industry, more than one third were due to corrosion or corrosion related process (Abduh, 2008). The failures in the oil and gas industry usually cause interruption of production, environmental pollution and sometimes even fatal damage. In 2006, there was an oil spill in the Prudhoe Bay oil field that BP Alaska operated, originated from a small hole on the wall of one of the pipelines, which was attributed to corrosion. The amount of leakage was estimated to be over 5,000 barrels of crude oil. More corrosion damage was detected thereafter and oil production had to be shut down for months in most of the Prudhoe Bay oil field. BP had to pay a large penalty and the oil price increased after this incident, since the Prudhoe Bay oil field is a major oil supplier for North America.

Oil and gas production and transportation involves a series of complex processes and corrosion issues are identified in many different forms. Corrosion resistant alloys, such as 13% Cr steel and stainless steel are commonly employed to combat corrosion problems in production tubing downhole. While, for flowlines that can extend up to thousands of miles, carbon steel is still the best choice due to cost vs. performance. Nowadays, other solutions to corrosion problems are getting more attention and

investments have been made to support the research projects related to corrosion issues found in the oil and gas industry. One such major project in the Institute for Corrosion and Multiphase Technology at Ohio University is the Corrosion Center Joint Industry Project (CCJIP), and is sponsored by about 20 major production and service companies from the oil and gas industry. This project strives to get fundamental understanding of different aspects of carbon steel corrosion. The research directions include, but are not limited to: mechanisms of localized CO<sub>2</sub> corrosion, the mechanisms of H<sub>2</sub>S corrosion, corrosion inhibition, and under-deposit corrosion, etc. The work presented below is a part of the CO<sub>2</sub> corrosion studies conducted within the CCJIP.

Corrosion takes place when the carbon steel surface is wetted with water, which usually entrains acidic gases, such as CO<sub>2</sub>. CO<sub>2</sub> corrosion is one of the most common corrosion environments in the oil and gas industry. For the past few decades, extensive studies have been made to understand CO<sub>2</sub> corrosion mechanism (Dugstad, 2006; Kermani & Morshed, 2003; Schmitt & Horstemeier, 2006). It is generally agreed that the general CO<sub>2</sub> corrosion has been well understood. However, it is localized corrosion that usually causes major failures and can have catastrophic consequences, due to the difficulties in prediction and detection of localized corrosion.

One important cause of localized CO<sub>2</sub> corrosion is failure of the protective iron carbonate layer which forms on the carbon steel surfaces under certain conditions. This layer can act as a diffusion barrier for corrosive species and also covers portions of the steel surface and thus provides protection to the underlying steel from corrosion. On the other hand, partial damage of the protective layer could expose part of the steel to the

corrosive environment, and a galvanic cell may be established between the layer-covered surface and layer-free surface, which leads to severe localized corrosion. Partial removal of protective iron carbonate can be attributed to two mechanisms: mechanical removal by flow and/or chemical removal by dissolution. However, the exact removal mechanisms of the protective iron carbonate layer are still not clear and therefore need further attention.

## CHAPTER 2: LITERATURE REVIEW

In order to explain the motivation behind this dissertation, a literature review related to the current research topic was grouped in three key areas: carbon dioxide corrosion, iron carbonate layer formation and mechanisms of protective iron carbonate layer removal. The main findings were summarized and the major gaps and issues were identified.

### 2.1 Carbon dioxide corrosion

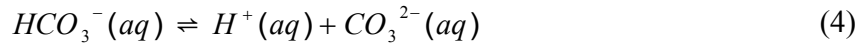
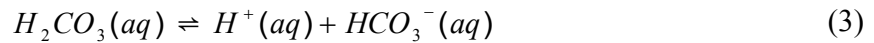
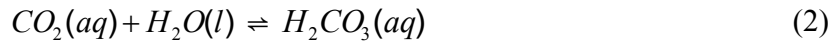
#### 2.1.1 Carbon dioxide corrosion mechanism

Carbon dioxide (CO<sub>2</sub>) corrosion, or so-called “sweet corrosion” of steel, is the most common corrosion environment encountered in the production and transportation of oil and gas. To combat this, corrosion resistant alloys could be employed. However, due to the cost/performance considerations, mild steel is still widely used for pipelines and plants in the oil and gas industry. When a water phase is in contact with the mild steel surface in the presence of corrosive species such as CO<sub>2</sub>, severe corrosion could occur and may lead to a failure. As corrosion has been recognized as a serious issue in the oil and gas industry in the past few decades, extensive studies have been made on the mechanism of CO<sub>2</sub> corrosion in order to improve the corrosion mitigation strategy.

CO<sub>2</sub> corrosion of mild steel is a complex process including chemical reactions in the bulk, electrochemical reactions on the steel surface and the transport of species to and from the bulk solution to the steel surface.

It is generally agreed that a given set of chemical reactions occurs in the aqueous solution in the CO<sub>2</sub> corrosion environment. CO<sub>2</sub> dissolves in water and forms carbonic

acid ( $H_2CO_3$ ), which partially dissociates and releases a proton ( $H^+$ ) and a bicarbonate ( $HCO_3^-$ ) ion, as shown in reactions (1) to (3). Furthermore, the bicarbonate ion will dissociate once more and release a carbonate ion ( $CO_3^{2-}$ ) and one more proton.



Because carbonic acid is a weak acid and it only dissociates partially, the  $CO_2$  corrosion environment is deemed as a buffering system and the equilibrium is dependent on temperature, the partial pressure of  $CO_2$  and the ionic strength of the aqueous solution. When the above reactions (plus water ( $H_2O$ ) dissociation (reaction (5))) are expressed in terms of equilibrium equations and the electroneutrality equation is added (Equation (6)), the concentration of each species at equilibrium can be calculated. The equilibrium constants of reactions (1) to (5) can be found in the literature (for a good summary see Nordsveen, Nesic, Nyborg, & Stangeland, 2003).

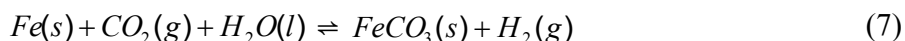


$$[H^+] + [X^+] = [HCO_3^-] + [CO_3^{2-}] + [OH^-] + [Y^-] \quad (6)$$

where  $X^+$  and  $Y^-$  stand for all other cations and anions presented in the solution, “[ ]” represents the equilibrium concentration of different species.

The overall electrochemical reaction that occurs on mild steel surface in the  $CO_2$  corrosion environment can generally be expressed as reaction (7), which is composed of

both an anodic reaction (iron dissolution) and a cathodic reaction (hydrogen reduction). Under certain conditions, a layer of solid iron carbonate ( $\text{FeCO}_3$ ) can form on the steel surface, which will be explained in detail later.



The mechanism of the anodic and cathodic reactions has been investigated by many researchers. The iron dissolution reaction can be written as in (8), in which iron is oxidized and two electrons are released.



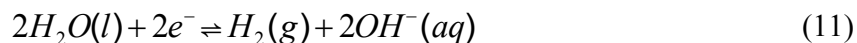
The mechanism of iron dissolution was first proposed by Bockris, Drazic, & Despic in 1961 and the study was followed by several researchers (de Waard & Milliams, 1975a; Hurlen, Gunvaldsen, Tunold, Blaker, & Lunde, 1984; Nescic, Thevenot, Crolet, & Drazic, 1996; Schmitt & Rothmann, 1978b). It was agreed that iron dissolution was achieved in a multiple-step fashion involving some intermediate species, with various reaction routes proposed.

There are two commonly believed cathodic reactions as shown in reactions (9) and (10).



When the solution pH is less than 4 in a  $\text{CO}_2$  aqueous environment, reaction (9) is the dominant reaction (Nescic & Postlethwaite, 1996), which represents the proton reduction. This is also the case in strong acid (e.g., hydrochloric acid, HCl) corrosion,

where the reaction rate is directly related to the pH of the bulk solution and the mass transfer rate of protons from the bulk to the metal surface. When the solution pH is higher than 4, reaction (10) was proposed by de Waard & Milliams (1975a, 1975b) to explain the experimental observations that corrosion rates are higher in a CO<sub>2</sub> buffered solution than in strong acids under the same pH value. However, as carbonic acid only dissociates partially and can serve as a reservoir of protons, it can also be explained that the buffering effect of the CO<sub>2</sub> system is the cause of the high corrosion rates. Although many studies have been conducted to clarify this topic (Bonis & Crolet, 1989; Gray, Anderson, Danysh, & Tremaine, 1989; Schmitt & Rothmann, 1978a), consensus has still not been achieved (Remita et al., 2008). When the solution pH is higher (pH > 5), water reduction as shown by reaction (11) also plays a role according to Nescic & Postlethwaite (1996).



### *2.1.2 Factors influencing CO<sub>2</sub> corrosion*

CO<sub>2</sub> corrosion is a complex process and can be affected by various factors. In the following, the main factors influencing CO<sub>2</sub> corrosion will be reviewed, including temperature, CO<sub>2</sub> partial pressure, solution pH and flow condition. Since there will be a section below, specifically focusing on the situation when the iron carbonate layers are present, only the layer-free situation will be discussed in the present section.

#### *2.1.2.1 Effect of temperature*

In nature, all chemical, electrochemical and mass transport processes involved in CO<sub>2</sub> corrosion are accelerated by the increase of temperature. Therefore it is expected

that the increase of corrosion rate will be observed at elevated temperatures. Experimental studies (de Waard & Milliams, 1975a; Gray, Anderson, Danysh, & Tremaine, 1990; Netic & Postlethwaite, 1996) have been conducted to understand the temperature effect, which has proved this assumption under the protective layer-free conditions. At low temperature, studies were also made to evaluate the corrosion behavior of mild steel between 1°C to 10°C (Fang, 2006) and the results showed that the corrosion rate significantly decreased.

#### 2.1.2.2 Effect of CO<sub>2</sub> partial pressure

Increase of CO<sub>2</sub> partial pressure can accelerate the rate of reaction (1) and therefore lead to an increase of carbonic acid concentration in the solution, which is favorable for carbonic acid reduction and at the same time produces more protons according to reactions (3) and (4). All of these effects lead to the increase of corrosion rate ultimately, which is in agreement with experimental findings (de Waard & Lotz, 1993; Videm & Dugstad, 1989a).

#### 2.1.2.3 Effect of pH

The effect of pH is more prevalent when the solution pH is less than 4, because reduction of proton is the dominant cathodic reaction and the corrosion rate is directly related to the H<sup>+</sup> concentration in the solution and/or the mass transfer rate of H<sup>+</sup> from the bulk to the steel surface (de Waard & Lotz, 1993; Netic & Postlethwaite, 1996).

#### 2.1.2.4 Effect of flow condition

The effect of flow is achieved by influencing the mass transport process of species to and from the steel surface. Therefore the enhanced flow conditions may lead to

increases in the corrosion rate. According to Videm & Dugstad (1989a), the relationship between corrosion rate and flow rate under fully developed turbulent flow conditions can be expressed in Equation (12).

$$\text{corrosion rate} = \text{constant}(\text{flow rate})^{0.8} \quad (12)$$

The above statement is valid for single phase flow, while the cases become more complicated under multiphase flow conditions, as corrosion is more related to the flow pattern and phase wetting regime (Nesic, Wang, Cai, & Xiao, 2004). The effect of flow on protective layers is not fully understood and is the topic of this work.

### *2.1.3 CO<sub>2</sub> corrosion modeling*

Based on extensive studies of CO<sub>2</sub> corrosion, predictive models have been developed to describe CO<sub>2</sub> corrosion under different conditions. The CO<sub>2</sub> corrosion prediction models available in the literature can be categorized by the way the model was constructed. One class of models are mechanistic models (Gray, et al., 1989; Pots, 1995; Nordsveen, et al., 2003) and they were based on the mechanistic understanding of the interrelated chemical, electrochemical and mass transport processes involved in the CO<sub>2</sub> corrosion. The other type of models are recognized as empirical/semi-empirical models (de Waard & Lotz, 1993; de Waard, Lotz, & Dugstad, 1995; de Waard & Milliams, 1975a, 1975b; Oddo & Tomson, 1999), which are mainly based on corrosion data from the laboratory and/or the field. Nyborg (2002) wrote an extensive review of the characteristics of most available CO<sub>2</sub> corrosion models and compared these models in terms of how the important factors in CO<sub>2</sub> corrosion were modeled, such as the effect of pH, the effect of protective corrosion product layers, the effect of oil wetting and so on.

Nesic (2007) provided a “state of the art” review of corrosion modeling and analyzed those important factors influencing internal corrosion of mild steel pipelines and discussed the mathematical modeling strategies.

## **2.2 Iron carbonate layer formation**

Iron carbonate and iron carbide ( $\text{Fe}_3\text{C}$ ) are the two forms of corrosion product commonly seen in the  $\text{CO}_2$  corrosion environment (Crolet, Olsen, & Wilhelmsen, 1994). The iron carbide layer, also known as cementite, actually is the skeleton of the steel and remains after the corrosion of ferrite. It usually appears to be a loose, porous layer and is characterized as unprotective or even detrimental to the steel underneath, because iron carbide is conductive so that the porous structure provides more surface area for cathodic reactions. Besides, a galvanic effect between the iron carbide covered and bare steel surface may initiate localized attack (Crolet, Thevenot, & Nesic, 1998; Nesic & Lunde, 1994;). Furthermore, local acidification in the iron carbide layer might also happen and lead to the increase of the corrosion rate (Crolet, et al., 1994). On the other hand, iron carbonate is more often reported as a protective layer provided that the morphology of iron carbonate is dense and the layer adherent to the steel. It is the type of iron carbonate known as “protective” which is the topic of the present study.

### *2.2.1 Iron carbonate layer formation mechanism*

Iron carbonate precipitation/dissolution can be written as in reaction (13). The precipitation reaction happens when the concentrations of  $\text{Fe}^{2+}$  and  $\text{CO}_3^{2-}$  ions exceed the solubility limit (or solubility product) of  $\text{FeCO}_3$ , which is defined by Equation (14):



$$K_{SP} = [Fe^{2+}][CO_3^{2-}] \quad (14)$$

where  $K_{SP}$  is the solubility product of iron carbonate, the square brackets “[ ]” represent the concentration of  $Fe^{2+}$  and  $CO_3^{2-}$  ions when the solution is in equilibrium with the solubility limit.  $K_{SP}$  is a function of temperature and ionic strength (I). The unified expression of  $K_{SP}$  as shown in Equation (15) was developed by Sun, Nestic, & Woollam (2009) based on the literature data.

$$\begin{aligned} \log K_{SP} = & -59.3498 - 0.041377T_k - \frac{2.1963}{T_k} + 24.5724\log(T_k) \\ & + 2.518I^{0.5} - 0.657I \end{aligned} \quad (15)$$

where  $K_{SP}$  is in  $\text{mol}^2/\text{L}^2$ ,  $T_k$  is temperature in Kelvin and I can be calculated with Equation (16).

$$I = \frac{1}{2} \sum_i c_i z_i^2 = \frac{1}{2} (c_1 z_1^2 + c_2 z_2^2 + \dots) \quad (16)$$

where  $c_i$  represents the concentration of each species in the solution (mol/L) and  $z_i$  is the charge of the species.

The saturation level, defined in Equation (17), is an important parameter in dealing with iron carbonate precipitation.

$$S = \frac{c_{Fe^{2+}} c_{CO_3^{2-}}}{K_{SP}} \quad (17)$$

The role of saturation level on precipitation can be demonstrated clearly in Figure 1 (Lasaga, 1998), which shows different stability regions of salt AB regarding the concentrations of  $A^+$  and  $B^-$ . There are four regions corresponding respectively to region

of dissolution, the region of seeded crystal growth, the region of heterogeneous nucleation and crystal growth and the region of homogeneous nucleation and crystal growth.

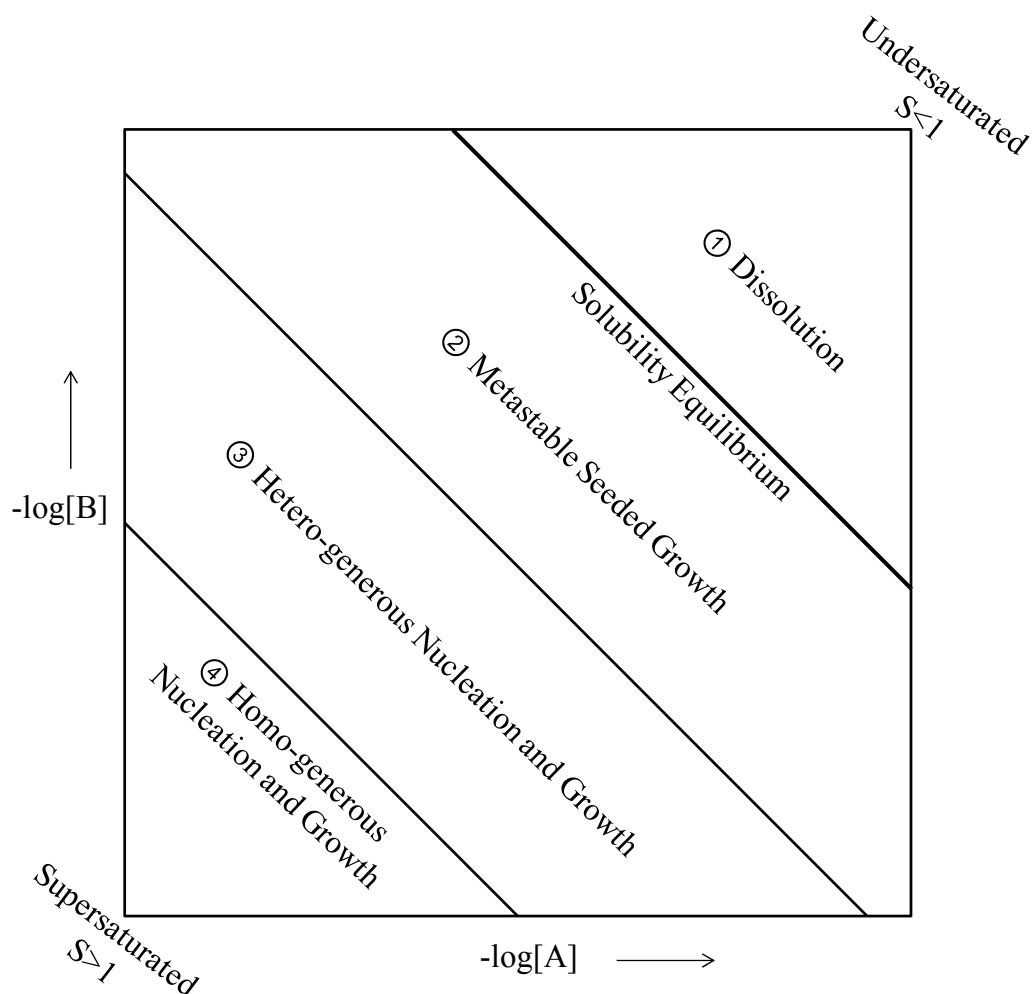


Figure 1. Different stability regions of compound AB (Lasaga, 1998)

When  $S < 1$ , the solution is undersaturated and iron carbonate dissolution becomes possible, corresponding to region ① in Figure 1. When  $S > 1$ , the solution is supersaturated regarding iron carbonate and precipitation happens. Depending upon the

degree of supersaturation (SS, equal to  $S$  when  $S > 1$ ), precipitation of iron carbonate can fall into region ②, ③ or ④ and corresponds to nucleation and/or crystal growth.

In fact, the key role of saturation level in iron carbonate formation has long been identified (Dugstad, 1992). The importance of the saturation level near the steel surface was discussed by Nescic & Lee (2003). Moreover, an effort was also made to understand the role of nucleation and crystal growth according to the saturation level of iron carbonate close to the steel surface (M. Gao, Pang, & Gao, 2011).

There is also another important concept, scaling tendency, as introduced by van Hunnik, Pots, & Hendriksen (1996). Scaling tendency (ST) is defined as the ratio between iron carbonate precipitation rate (PR) and mild steel corrosion rate (CR) expressed in the same units, as shown in Equation (18).

$$ST = \frac{PR}{CR} \quad (18)$$

It was suggested by the author that a protective iron carbonate layer formation is only possible when ST is higher than the critical value, which depends on the steel composition and the environment. When ST is much higher than 1, a protective iron carbonate layer can be formed. Nescic & Lee (2003) successfully employed the concept of surface and bulk scaling tendency to predict the growth of iron carbonate layer.

### *2.2.2 Factors influencing iron carbonate layer formation*

The effect of several important factors on CO<sub>2</sub> corrosion under the layer-free condition was explained earlier in this Chapter. In this section, the effect of those abovementioned factors on iron carbonate layer formation will be summarized.

#### 2.2.2.1 Effect of temperature

As can be seen in Equation (15), the solubility limit decreases as temperature increases. Therefore at higher temperatures, with the same amount of ferrous and carbonate ions in the solution, the saturation level is higher than at lower temperatures. Iron carbonate precipitation kinetics are then accelerated and the iron carbonate layer formation is more favorable. A protective iron carbonate layer can slow down the corrosion process by serving as a diffusion barrier and covering part of the steel surface. This has been observed by in many studies (de Waard & Milliams, 1975a; Dugstad, 1992; Dugstad, Hemmer, & Siersten, 2001; Gray, et al., 1990). Since temperature has conflicting effects on electrochemical corrosion reactions and iron carbonate precipitation (the former accelerate the attack and the latter retards it), it was expected that the corrosion rate would show a maximum value as temperature increases, which is actually the case. However, if the temperature is rather low (around 25°C or lower), protective iron carbonate formation is so slow that a layer could not be found even at high supersaturation and long exposure times (Berntsen, Seiersten, & Hemmingsen, 2011; Nestic & Lunde, 1994).

#### 2.2.2.2 Effect of CO<sub>2</sub> partial pressure

If other conditions remain the same (temperature, pH, etc.), the concentration of carbonate and bicarbonate can be increased due to the increase of CO<sub>2</sub> partial pressure, which consequently leads to an increase of saturation level with respect to iron carbonate. Therefore iron carbonate layer formation is accelerated and corrosion of the steel surface

is limited, which was observed in experimental studies (de Moraes, Shadley, Chen, & Rybicki, 2000).

#### 2.2.2.3 Effect of pH

The solution pH is a key parameter in iron carbonate formation, due to the fact that pH is directly related to  $\text{CO}_3^{2-}$  concentration and therefore affecting the saturation level of iron carbonate (Chokshi, Sun, & Nescic, 2005; Dugstad, 1992; Videm & Dugstad, 1989b).

#### 2.2.2.4 Effect of flow condition

An increase of flow velocity leads to an enhanced mass transfer process, and the released ferrous ions due to corrosion can be more easily carried away from the steel surface, which lowers the saturation level at the surface and slows down iron carbonate precipitation. Considering the higher corrosion rate experienced under increased flow velocity, the scaling tendency becomes lower. Therefore under high flow velocity, it is more difficult to form a protective layer.

Once a protective iron carbonate layer is developed the question is whether it will remain protective. It was reported that under highly turbulent flow conditions, the protective iron carbonate layer could be damaged and lead to severe localized corrosion. A detailed review of this phenomenon will be presented later in this Chapter.

#### *2.2.3 Iron carbonate precipitation kinetics<sup>1</sup>*

As already introduced, various corrosion prediction models are available; however, how to account for the effect of protective layers is a key component of

---

<sup>1</sup> The content in this section has been incorporated into a co-authored manuscript prepared by Woollam, R., Yang, Y., and Nescic, S.

successful corrosion rate prediction, since the presence of protective iron carbonate layer can significantly slow down the corrosion rate. As demonstrated earlier, scaling tendency is an important parameter in predicting whether a protective iron carbonate layer can form under specific conditions and it thus plays a vital role in corrosion modeling (Nesic & Lee, 2003). Therefore it is very important to characterize iron carbonate precipitation kinetics.

Several studies (Greenberg & Tomson, 1992; Johnson & Tomson, 1991; Sun & Nesic, 2008; van Hunnik, et al., 1996) were made on iron carbonate precipitation kinetics. The experimental method used by Johnson & Tomson (1991), Greenberg & Tomson (1992) and van Hunnik, et al. (1996) to characterize precipitation rates was based on the measurement of the consumption of ferrous ion concentration in the bulk solution. The study of Sun & Nesic (2008) obtained precipitation rates by the weight change measurement of the precipitated iron carbonate on the corroding steel specimen. Semi-empirical equations for precipitation rate prediction were derived by all the researchers using the same general form:

$$PR = k_r \frac{A_s}{V} K_{SP} \sigma(S) \quad (19)$$

where  $k_r$  is the reaction constant,  $A_s/V$  is the surface area (specimen) to volume (test solution) ratio and  $\sigma(S)$  is the driving force function. Based on their experimental results, the parameters and function form in Equation (19) were determined for each study, as shown in Table 10.

Table 1. Equations for iron carbonate precipitation rate prediction (Sun, 2006).

Authors	Equations	Constants
Johnson & Tomson (1991)	$PR\left(\frac{mol}{m^3 \cdot s}\right) = e^{A - \frac{B}{RT_K}} \frac{A_s}{V} K_{sp} \{(S)^{0.5} - 1\}^2$	A: 56.3 B: 127.3
Greenberg & Tomson (1992)	$PR\left(\frac{mol}{m^3 \cdot s}\right) = e^{A - \frac{B}{RT_K}} \frac{A_s}{V} K_{sp} \{(S)^{0.5} - 1\}^2$	A: 44.4 B: 95.8
van Hunnik, et al. (1996)	$PR\left(\frac{mol}{m^3 \cdot s}\right) = e^{A - \frac{B}{RT_K}} \frac{A_s}{V} K_{sp} (S - 1)(1 - S^{-1})$	A: 52.4 B: 119.8
Sun & Nesic (2008)	$PR\left(\frac{mol}{m^3 \cdot s}\right) = e^{A - \frac{B}{RT_K}} \frac{A_s}{V} K_{sp} (S - 1)$	A: 28.2 B: 64.9

When comparing the predictions made with the above equations, large discrepancies are seen for precipitation rates. As shown in Figure 2, the predicted precipitation rates span more than two orders of magnitude, with the prediction made by Sun & Nesic (2008) being distinctly different from the other three. This was also pointed out by Sun (2006).

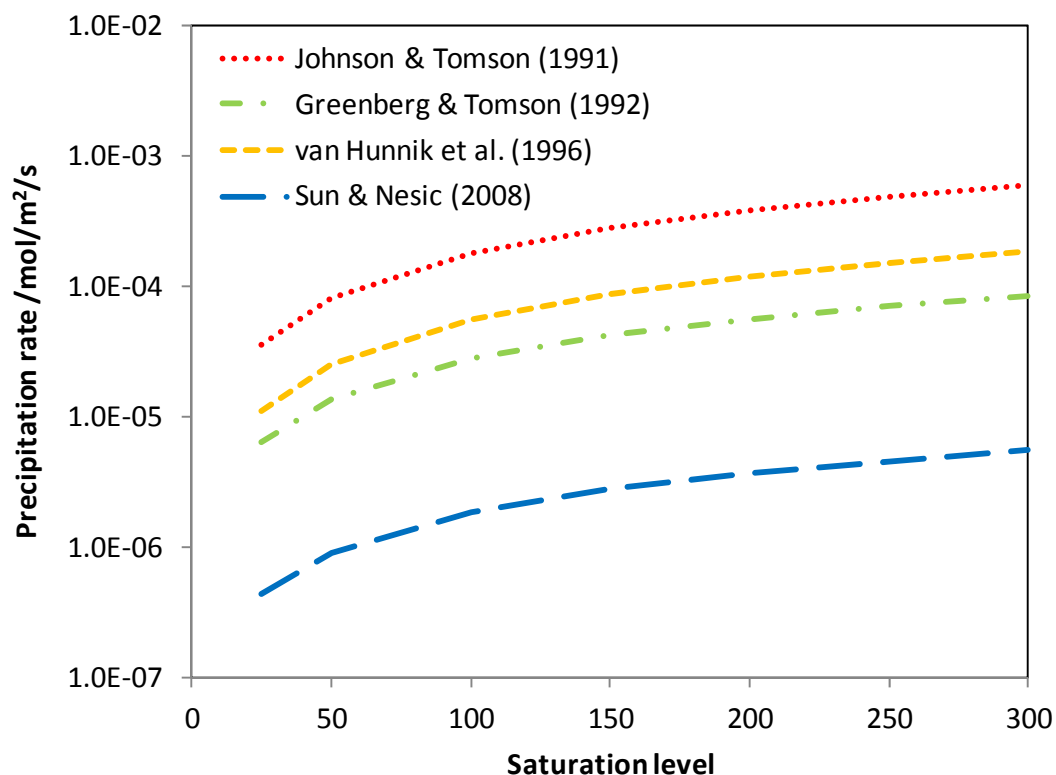


Figure 2. Comparison of iron carbonate precipitation rate predictions from different authors at 80°C, using  $A_s/V=1$ .

It was claimed by Sun & Nestic that the difference was due to the different experimental methods, as the other three studies were based on the ferrous ion consumption method, which might lead to overestimation of precipitation rate by including the precipitation on the various surfaces exposed to the bulk solution. The assumption might be true for the study of van Hunnik, et al. (1996), since high saturation levels (of the order of  $10^3$ ) was used in their experiments, which corresponds to region ③ and/or ④ in Figure 1, where nucleation and growth in the bulk solution could cause the overestimation of precipitation rate.

However, this explanation is not applicable for the other two studies. The experiments were conducted with seeded iron carbonate crystals at very low saturation level ( $S < 2$ ) by Johnson & Tomson (1991) and Greenberg & Tomson (1992). Referring back to Figure 1 (Lasaga, 1998), at very low saturation level (region ②) only crystal growth is possible so there should be no nucleation in the bulk solution (Nancollas, 1979). Conversely, in Sun & Nescic's (2008) study, the saturation level ranges from 10 to 300, therefore iron carbonate precipitation covers the ②, ③ and ④ regions and involves both nucleation and crystal growth. Based on the above analysis, it can be seen that the reason for the discrepancy observed in precipitation rate prediction (as seen in Figure 2), could be attributed to the fact that different stages of precipitation (nucleation and crystal growth) were measured in the studies shown above.

### **2.3 Mechanisms of protective iron carbonate layer removal**

Formation of a protective iron carbonate layer on the steel surface could slow down the corrosion rate of the underlying metal. On the other hand, if the protective layer is damaged by any means, the steel substrate would be exposed to the corrosive environment and cause initiation of localized corrosion. It was proven that under specific conditions, a galvanic cell could be established between the iron carbonate layer covered surface and the layer-free surface, which then led to severe localized corrosion (Han, Brown, & Nescic, 2010; Xia, Chou, & Szklarska-Smialowska, 1989). Therefore, how the protective iron carbonate layer is removed became the key point crucial in understanding of initiation and propagation of localized corrosion in the CO<sub>2</sub> corrosion environment. As seen in the literature (details described below), two possible mechanisms are responsible

for protective iron carbonate layer removal by flow: mechanical removal and chemical removal by dissolution.

### *2.3.1 Mechanical removal mechanism*

The effect of hydrodynamic flow on the protectiveness of the iron carbonate layer has been debated for years. Studies have been made in order to identify under what conditions the layer could be removed and what was the key parameter that characterized the resistance of the iron carbonate layer to mechanical damage by flow. The motivation behind this was the belief that the partial damage of the protective layer by flow could lead to localized corrosion, and this phenomenon was given a special name: flow induced localized corrosion (FILC).

In the work presented by Schmitt, Gudde, & Strobel-Effertz (1996), a failure mode diagram for iron carbonate scales was constructed based on theoretical considerations for failure mechanism analysis, along with assumptions of iron carbonate scale properties according to the data available for oxide scales. The critical value of fracture strains and stresses was evaluated based on the failure diagram of iron carbonate, and appeared to be in good agreement with experimental results. It was concluded that the flow induced localized corrosion in the presence of iron carbonate layer was due to the increase of intrinsic stress inside the layer as the layer formed, which could exceed the critical stresses for iron carbonate layer fracture and spalling. In addition, the authors claimed that the contribution of flow turbulence was to prevent re-formation of the spalled iron carbonate layer, rather than directly remove the protective layer and the wall shear stress was too small to remove the scale.

A direct measurement of the mechanical properties of iron carbonate layer was made later by Schmitt, Mueller, & Strobel-Effertz (1999). The results are shown in Table 2. In agreement with the earlier study (Schmitt, et al., 1996), the intrinsic strength of iron carbonate scales was attributed as the cause of scale spalling. This piece of work was considered as the first attempt of characterizing the mechanical properties of iron carbonate layer. However, there were still many issues worth being considered. For example, when using the microindentation method to measure the Young's modulus and Vickers hardness of the iron carbonate scale, the specimen covered with iron carbonate was polished before the measurement, as seen in the SEM images shown in the original paper. The author did not mention anything about the detailed procedure for preparing the iron carbonate specimen or whether the results could be affected by the test procedure, which made the validity of the results questionable. In addition, for adhesion strength measurement, there were also no details of what was observed during the measurement, which brought up the question of whether the measured value truly reflected the scale adhesion strength, because the contact of the adhesive used in the measurement with the steel substrate could significantly interfere with the measured value.

Table 2. Comparison of estimated and measured mechanical properties of iron carbonate scales (Schmitt, et al., 1999).

Parameter	Estimated	Measured
Surface fracture energy, $\gamma$ (N/m)	3.0	no
Young's modulus, E (GPa)	150	125 <sup>a</sup>
Fracture stress, $\sigma_y$ (MPa)	1400 (single crystal)	75 - 100 <sup>b</sup> 230-720 <sup>c</sup>
Fracture strain, $\epsilon_y$ ( $\times 10^{-3}$ )	9.33	1.8 - 5.6 <sup>c</sup>
Intrinsic stress, $\sigma_{sc}$ (MPa)	-(200 - 200)	-(20 - 50) <sup>d</sup> -90 $\pm$ 40 <sup>e</sup>
Intrinsic stress intensity, $K_{res}$ ( $\text{Pa} \cdot \text{m}^{1/2}$ )	No	110~136 <sup>a</sup>
Limiting scale thickness, h (m)	$1.46 \times 10^{-6}$	No
Critical strain, $\epsilon_{crit}$	$2.5 \times 10^{-4}$	$5.3 \times 10^{-4}$ <sup>f</sup>
Adhesion, $\sigma_{ad}$ (MPa)	no	8.4 - 18.3 <sup>a</sup>
Hardness (Vickers), $H_v$ (MPa)	no	220 - 650 <sup>a</sup>

<sup>a</sup> Microindentation method. <sup>b</sup> Scale thickness 80  $\mu\text{m}$ ; 0.2  $\gamma$ . <sup>c</sup> 4-point loading test.

<sup>d</sup> dilatometric measurement. <sup>e</sup> X-ray diffraction. <sup>f</sup> Micro-3-point-bend measurement.

Schmitt & Mueller (1999) showed some experimental results obtained with a jet impingement setup. They provided a different mechanism of flow induced localized corrosion in the presence of protective iron carbonate layer. It was claimed that the “micro-turbulences” in the near-wall region caused pressure changes and led to cyclic loading on the scale, which was responsible for the “fatigue” cracking of the scales. Critical wall shear stress was used as the parameter to identify the onset of flow induced localized corrosion. However, further proof of the existence of “micro-turbulences” as well as “fatigue” is needed to support the above mechanism.

K. Gao et al. (2008) conducted experiments to study the mechanical properties of the corrosion product scale formed under different flow velocities and CO<sub>2</sub> partial pressures. The uniform and localized corrosion rates were correlated with the interfacial fracture toughness of the scale, which was claimed as the parameter characterizing the resistance of the scale to mechanical flow damage. However, in their tests, the flow characteristics were not mentioned, which is an important aspect in evaluating flow induced localized corrosion. The water chemistry was not characterized at all in the experiments, not to mention the saturation level of iron carbonate, which was essential in ensuring that no effect of chemical dissolution contributed to the scale removal. Moreover, the solution was composed of other ions, such as Ca<sup>2+</sup> and Mg<sup>2+</sup>, which also formed precipitates with CO<sub>3</sub><sup>2-</sup>. In that case, it was very important to document the saturation level of FeCO<sub>3</sub>, as it could be affected by the co-precipitation of other insoluble compounds in the solution. In addition, the uniform corrosion rate measurements were done by weight loss method, which can only quantify the integrated corrosion rate over the whole period of the test and therefore can be very misleading in characterizing the protectiveness of the corrosion product layer at the end of the test. Therefore, their conclusions were questionable.

Another study published by Ruzic, Veidt, & Nestic (2006a) showed experimental work done in a glass cell with rotating cylinder electrode setup under single phase turbulent flow conditions. Protective iron carbonate layer was formed before the increase of rotating speed. Partial breakdown of the layer was observed at high rotating speed. However, at the beginning of iron carbonate layer formation, an anodic current of 28.39

mA (equivalent of 87.6 mm/year corrosion rate) was applied to the steel specimen for 4 hours. Although the author claimed the process was reproducible and led to a thicker film, the method itself is highly un-realistic. In addition, in this type of setup it is difficult, if not impossible, to avoid vibration and centrifugal forces which affect the stresses experienced by the iron carbonate layer. Therefore it is doubtful whether the observations made based on this type of film removal could be comparable with other studies.

Nesic & Lunde (1994) conducted a series of flow loop experiments to investigate CO<sub>2</sub> corrosion under severe flow condition. In their study, protective iron carbonate layer was formed in supersaturated solutions at 80°C and pH 5.5 under single phase flow conditions with disturbance and gas-liquid two phase flow with slug flow regime. Based on the experimental results, it was claimed by the authors that the protective layer appeared to be “very robust and resistive to severe flow conditions” (Nesic & Lunde, 1994). However, antimony was detected in the corrosion product layer which could improve the protectiveness of the layer. Therefore, the conclusion was questionable.

From the above analysis of the main studies related to the effect of hydrodynamic flow on protective iron carbonate layer, it was shown that there has been no consensus reached yet with respect to how and why the protective iron carbonate layer was damaged by flow. Little work was done to characterize the mechanical properties of iron carbonate layer, as the process is not trivial.

### 2.3.2 Chemical removal mechanism

It is known that iron carbonate dissolves when the solution is undersaturated, which is the backward reaction in the precipitation/dissolution reaction (13). Iron carbonate dissolution is an important phenomenon in CO<sub>2</sub> corrosion as the protectiveness of the iron carbonate layer can be damaged and lead to exposure of the steel substrate.

The effect of iron carbonate dissolution on mild steel corrosion in CO<sub>2</sub> environment was first documented by Dugstad in 1992 in his study on the importance of supersaturation in CO<sub>2</sub> corrosion. He illustrated the interaction between corrosion rate and solution saturation level as in Figure 3 (Dugstad, 1992) and used it to explain the initiation of mesa attack at high temperatures. At the beginning of the test (point A), steel was exposed to iron-free water and a high corrosion rate was observed. As corrosion proceeded, more ferrous ions were released and the saturation level increased. The solution eventually became supersaturated and led to the formation of protective iron carbonate layer (point B). The saturation level decreased towards the solubility limit due to the consumption of ferrous ion by precipitation. When the layer was damaged (point C) locally, it could not be easily repaired because the saturation level was low, and this would initiate localized corrosion. If a large area of iron carbonate layer was damaged, corrosion rate increased releasing sufficient iron into solution so that a layer could be reformed.

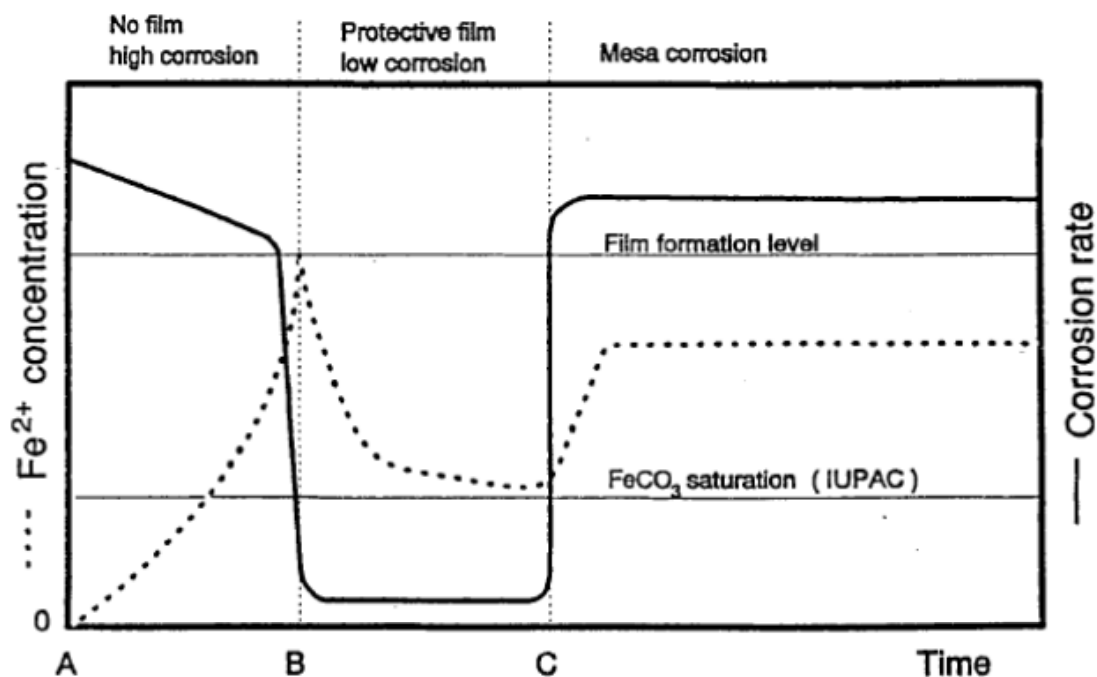


Figure 3. Schematic illustration of the interaction between corrosion rate and solution saturation level (Dugstad, 1992).

Ruzic, Veidt, & Nescic (2006b) investigated the effect of iron carbonate dissolution on CO<sub>2</sub> corrosion, following their study of mechanical removal (Ruzic, et al., 2006a). Based on the experimental results, a mass transfer controlled mechanism was proposed. As pointed out already, the procedure of iron carbonate layer formation in their study involved anodic polarization for 4 hours with large current, which resulted in a very unrealistic iron carbonate layer.

In the geological field, since carbonates are very commonly seen as minerals on earth, extensive studies have been made to understand their mechanism of dissolution (Duckworth & Martin, 2004a, 2004b; Morse, 1983; Morse & Arvidson, 2002; Plummer, Parkhurst, & Wigley, 1979). Dissolution kinetics of iron carbonate was studied in a range

of temperatures and pressures (Benezeth, Dandurand, & Harrichoury, 2009; Dresel, 1989; Golubev, Bénézeth, Schott, Dandurand, & Castillo, 2009; Greenberg & Tomson, 1992; Pokrovsky & Schott, 2002; Testemale et al., 2009; van Cappellen, Charlet, Stumm, & Wersin, 1993). The effects of environmental conditions, such as the presence of oxygen (Duckworth & Martin, 2004a, 2004b) and chromate (Tang & Martin, 2011), were also investigated. It was suggested that the dissolution of iron carbonate was a surface reaction controlled process. In all of the studies, samples of siderite mineral were used, in either the form of a single crystal, powder or polycrystalline.

Despite the fact that some work was done related to iron carbonate dissolution in the geological area, there is very little information available which is directly related to CO<sub>2</sub> corrosion and specifically to conditions seen in the oil and gas industry. One difference is related to the presence of a steel substrate in corrosion which is not present in the geological systems. The nature and amount of minor components (contaminants) in solid iron carbonate are different for the two systems. Finally, it is not common to investigate the direct effect of flow in studies coming from the geological area.

### CHAPTER 3: RESEARCH OBJECTIVES

Localized corrosion mechanism is of great interest in CO<sub>2</sub> corrosion study. One of the possible scenarios is that, initiation of localized corrosion can be introduced by partial removal of the protective iron carbonate layer formed on the carbon steel surface. Based on the literature review of previous research, the removal mechanism of protective iron carbonate layer is still unclear, which becomes the motivation behind the current study.

In the present work, experimental studies will be made to understand how and why removal of the protective iron carbonate layer happens. This is achieved by investigating separately the effect of mechanical removal and chemical dissolution on the protective iron carbonate layer in flowing solutions.

The effect of flow will be investigated in single phase flow with various experimental configurations and techniques to understand the effect of hydrodynamic forces alone on protective iron carbonate layers. The various tasks are:

- Develop a reproducible protective iron carbonate layer on carbon steel surface in CO<sub>2</sub> corrosion environment.
- Investigate the flow effect on protective layer in small scale experimental setups, such as glass cell with a rotating cylinder setup and a glass cell with a jet impingement setup.
- Design and construct a medium scale flow loop (thin channel flow cell), which can enable testing under more realistic flow conditions.
- Study the flow effect on protective iron carbonate layer in the medium scale flow loop.

- Measure the adhesion strength between protective iron carbonate layer and steel substrate.
- Evaluate the possibility of mechanical removal by flow according to the experimental results.

The effect of chemical dissolution on the protective iron carbonate layer will be studied both qualitatively and quantitatively. The following tasks are included:

- Observe the qualitative changes of the protective iron carbonate layer during dissolution by using surface analysis tools, such as SEM.
- Study the effect of chemical dissolution of the protective iron carbonate layer on carbon steel corrosion using a rotating cylinder setup.
- Adapt a new technique, electrochemical quartz crystal microbalance (EQCM), to directly quantify in situ mass change due to iron carbonate formation and dissolution.
- Propose a mechanism for iron carbonate dissolution.

Portions of the work presented in this dissertation were published previously in the co-authored papers (Han, Yang, Brown, & Nescic, 2007; Han, Yang, Brown, & Nescic, 2008; Han, Nescic, Yang, & Brown, 2011; Yang, Brown, & Nescic, 2008; Yang, Brown, Nescic, Gennaro, & Molinas, 2010).

## CHAPTER 4: MECHANICAL EFFECT OF FLOW ON PROTECTIVE IRON CARBONATE LAYER<sup>2</sup>

### 4.1 Introduction

As introduced in Chapter 2, a protective iron carbonate layer can form in CO<sub>2</sub> corrosion environments under certain conditions. However, partial damage to the protective iron carbonate layer could lead to severe localized corrosion. It was brought up in the literature review that one of the possible scenarios is that turbulent flow plays an important role in damaging the protective layer. In order to investigate the effect of flow on the protective iron carbonate layer, a series of experiments were conducted with different experimental configurations to observe the change of the protectiveness of the iron carbonate layer. First a protective iron carbonate layer was built under flow with low intensity and then different types of flow condition were introduced. In addition, the mechanical property of iron carbonate layer was also evaluated and the feasibility of damaging the protectiveness of the iron carbonate layer by flow was assessed.

In order to create a well established and defined flow condition, both small scale glass cell and medium scale flow loop were used in the current study. The glass cell is commonly used in small scale experimental studies. It is normally set up as a three-electrode system, including reference electrode, counter electrode and working electrode. Different flowing conditions can be achieved by slight modification, such as by using a rotating cylinder electrode setup or a jet impingement setup. For a medium scale flow loop testing, a completely new test setup, the thin channel flow cell (TCFC), was

---

<sup>2</sup> Portions of the work presented in this Chapter were published in the co-authored papers (Han, et al., 2007; Han, et al., 2008; Yang, et al., 2010).

designed and constructed to create a more realistic flow condition compared with small scale configurations. Finally, a tensile machine was used to evaluate the mechanical properties of the protective iron carbonate layer. Detailed information of the abovementioned test setups will be given later.

For the hydrodynamic tests, the wall shear stress will be used as the parameter to compare the flow condition encountered in various experimental configurations. This is not seen as a problem, as in undisturbed single phase flow (such as rotating cylinder electrode setup and thin channel flow cell system), there is good correlation among wall shear stress, mass transfer coefficient, and flow turbulence. For jet impingement flow condition, this also holds true in the wall jet region, while special attention will be paid to the stagnant region and transition region when analyzing the experimental results.

## **4.2 Tests done in a glass cell with rotating cylinder electrode setup**

### *4.2.1 Experimental method*

#### 4.2.1.1 Test setup

A glass cell with rotating cylinder electrode setup is shown in Figure 4, which was a three electrode system. A saturated Ag/AgCl electrode connected with Luggin capillary was used as the reference electrode. A concentric ring made from platinum wire served as the counter electrode. The working electrode was a cylindrical carbon steel specimen with 5.4 cm<sup>2</sup> exposed surface area. The temperature of the test solution was achieved by immersing a thermo probe connected to a heater controller. CO<sub>2</sub> gas inlet and outlet were used to purge CO<sub>2</sub> gas before and during the test to maintain a saturated CO<sub>2</sub> corrosion environment. A pH probe was immersed into the solution to monitor the

pH change during the test. The ferrous iron concentration was measured by taking samples of the test solution and testing with a spectrophotometer. The working electrode was mounted onto a shaft that can rotate at different speeds by connecting to a motor. An additional identical test specimen was mounted onto a stationary shaft at the beginning of the test and was removed from the solution after layer formation process, which was inspected by scanning electron microscope (SEM) to confirm the repeatability of the layer formation and also to compare with the working electrode after layer removal. A potentiostat was used to make electrochemical measurements during the test. Open circuit potential (OCP) was monitored and corrosion rate (CR) was measured using linear polarization resistance (LPR) technique. Electrochemical impedance spectroscopy (EIS) was used to measure the solution resistance in order to more accurately estimate the corrosion resistance of the working electrode. Unless specifically pointed out, the parameters of the electrochemical measurement in other tests remained the same as they are described for this test.

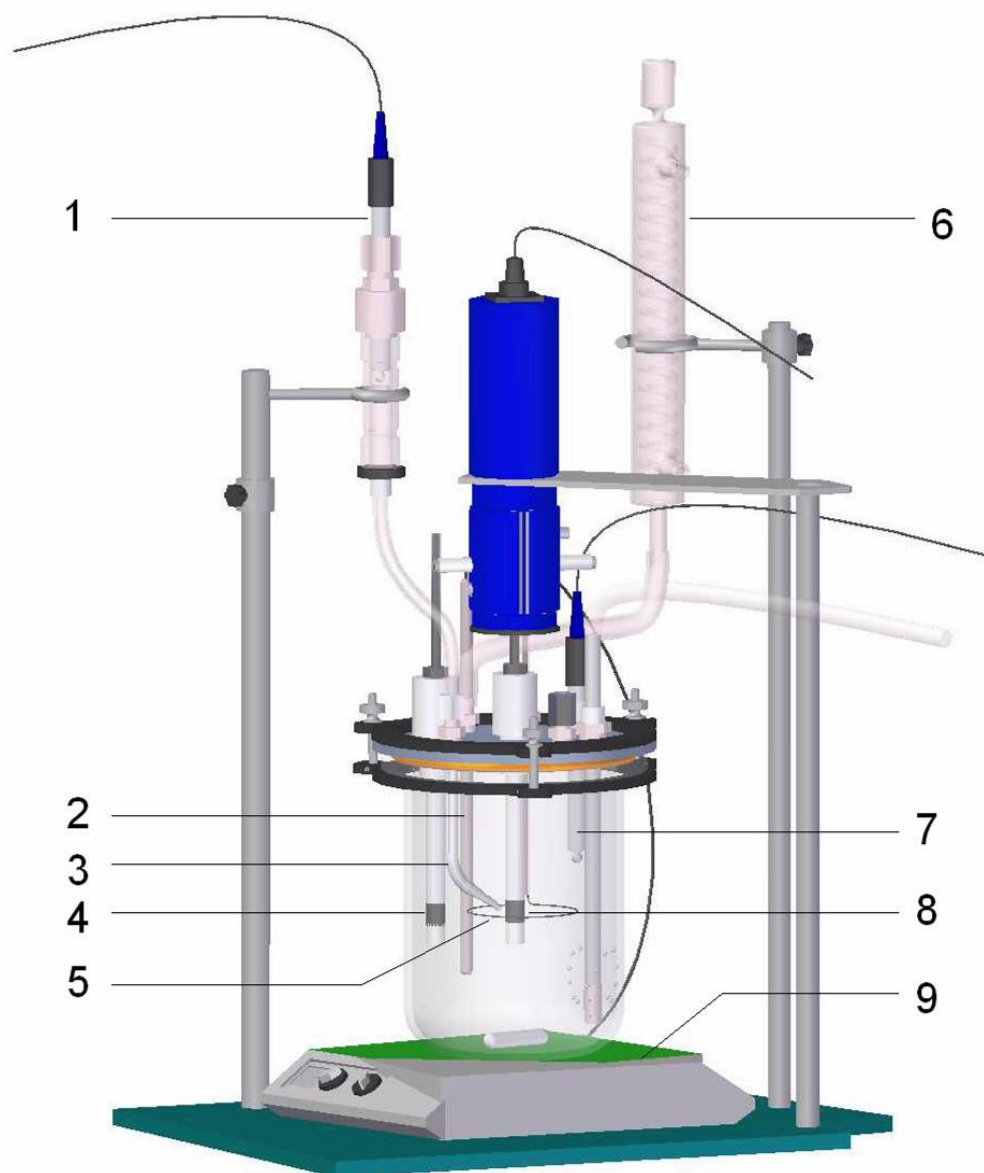


Figure 4. Schematic of glass cell with rotating cylinder electrode setup.  
1-reference electrode; 2- thermo probe; 3-Luggin capillary; 4-additional cylinder specimen; 5-counter electrode; 6-condenser; 7-pH probe; 8-working electrode (rotating cylinder); 9-heater.

#### 4.2.1.2 Test matrix

The test matrix of iron carbonate layer formation and removal with carbon steel specimen in CO<sub>2</sub> environment is shown in Table 3. The composition of C1018 is shown in Table 4.

Table 3. Text matrix for iron carbonate layer formation on carbon steel specimen.

Parameter	Layer formation	Layer removal
Material	Carbon steel C1018	
Test solution	1 wt% NaCl	
Temperature	80°C	
CO <sub>2</sub> partial pressure	0.52 bar	
Solution pH	6.6	
Initial supersaturation of FeCO <sub>3</sub>	300	
Rotating speed	0	7000 rpm
Wall shear stress	0	45 Pa
LPR	±5 mV vs E <sub>oc</sub> (0.125 mV/s)	
EIS	±5 mV vs E <sub>oc</sub> (1 mHz-100 kHz)	

Table 4. Chemical composition (wt%) of C1018.

C	Mn	Si	P	S	Cr	Cu	Ni	Mo	Al	Fe
0.19	0.83	0.22	0.015	0.013	0.13	0.16	0.016	0.042	0.004	Balance

#### 4.2.1.3 Test procedure

A test solution was prepared in the glass cell by adding 1 wt% of NaCl into 2 liters of de-ionized water. After being well mixed, the test solution was deoxygenated by continuously being purged with a CO<sub>2</sub> gas flow for at least 2 hours before test was started. At the same time, the solution was heated to 80°C and stabilized. After the desired temperature was achieved, the pH of the test solution was measured with a calibrated pH meter. NaHCO<sub>3</sub> solution with 1 M concentration was prepared and deaerated before adding into the test solution to adjust the pH to the designated value. The cylindrical C1018 test specimens (composition as shown in Table 4) were polished with 200, 400, 600 grit sand paper sequentially and cooled by isopropyl alcohol simultaneously to remove the heat generated during the polishing procedure. The two test specimens were then washed with deionized water and isopropyl alcohol in an ultrasonic cleaner to remove the debris on the surface after polishing and dried with blower. One test specimen was mounted on the shaft of the rotator and the other specimen was used as comparison for initial surface condition after iron carbonate layer formation. The test specimens were then immersed into the prepared test solution.

In order to accelerate the iron carbonate layer formation process, the ferrous ion concentration in the test solution was raised by adding deoxygenated FeCl<sub>2</sub>·4H<sub>2</sub>O solution to increase the supersaturation level of iron carbonate. Corrosion rate of the working electrode was monitored using LPR continuously during the test as iron carbonate was developing on the steel surface. When the corrosion rate became stable

and below 0.1 mm/year, the layer formation process was finished. The additional specimen was removed from the solution and rinsed with isopropyl alcohol, dried and stored properly for surface analysis using SEM. The rotating speed of the working electrode was then adjusted to 7000 rpm and corrosion rate was monitored continuously. When the experiment was finished, the specimen was taken out from the solution and rinsed, dried and stored. During the test, pH of the solution and ferrous ion concentration were measured regularly and recorded. Supersaturation level of iron carbonate was calculated based on the calculation using pH and ferrous ion concentration.

#### *4.2.2 Results and discussion*

The flow effect on protective iron carbonate layer was tested in a glass cell with rotating cylinder setup. The change of corrosion rate and supersaturation level of the solution during the test is shown in Figure 5. At the beginning of the test, the solution was kept at a high supersaturation of 300 with respect to iron carbonate, in order to build a layer on the steel surface in a short amount of time. As shown in the graph, the corrosion rate of the steel gradually decreased to a very low value (less than 0.1 mm/year), because a layer of protective iron carbonate layer formed on the steel surface and served as a diffusion barrier and also covered portions of the surface. The supersaturation level regarding iron carbonate also decreased from 300 to around 4 due to the precipitation of iron carbonate on the steel surface and in the bulk solution, which consumed the ferrous ion that was released from the steel specimen due to corrosion and the ferrous ion that was added to the solution at the beginning of the test. When the protective layer of iron carbonate was built and corrosion rate decreased to less than 0.1

mm/year and stabilized, the additional cylindrical specimen was taken out for surface analysis using SEM as shown in Figure 6. The rotating cylinder electrode then was rotated at 7000 rpm and the shear stress ( $\tau_{RCE}$ ) on the rotating cylinder surface was 45 Pa as calculated from Equation (20) (Eisenberg, Tobias, & Wilke, 1954):

$$\tau_{RCE} = 0.0791 Re_{RCE}^{-0.3} \rho r_{RCE}^2 \omega^2 \quad (20)$$

$$Re_{RCE} = \frac{2\omega r_{RCE}^2}{\gamma} \quad (21)$$

where  $\tau_{RCE}$  is the wall shear stress on rotating electrode surface,  $Re_{RCE}$  is the Reynolds number,  $\rho$  is the density of the solution,  $r_{RCE}$  is the radius of the cylinder,  $\omega$  is the angular velocity,  $\gamma$  is the kinematic viscosity of the solution.

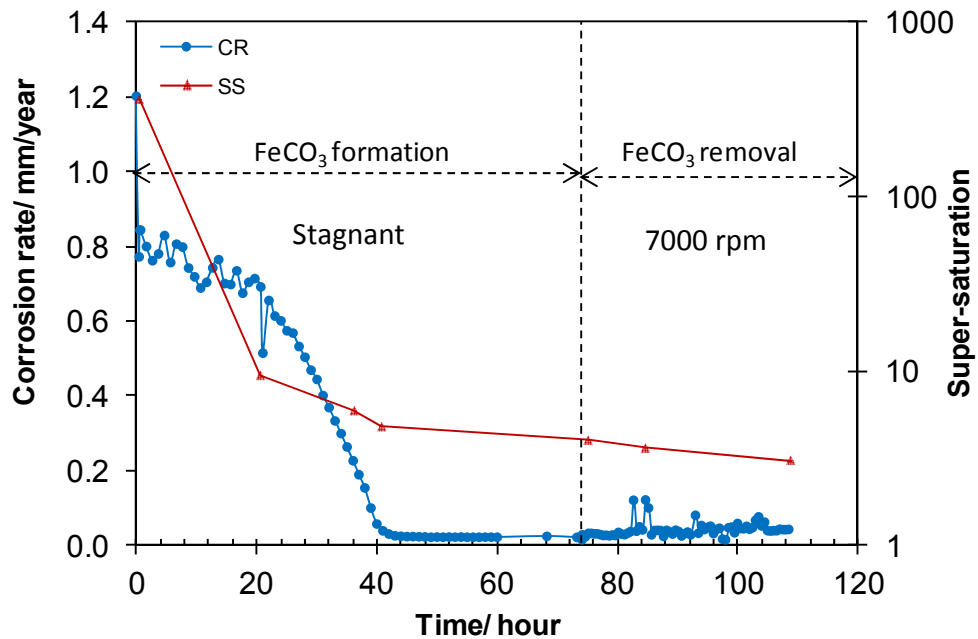
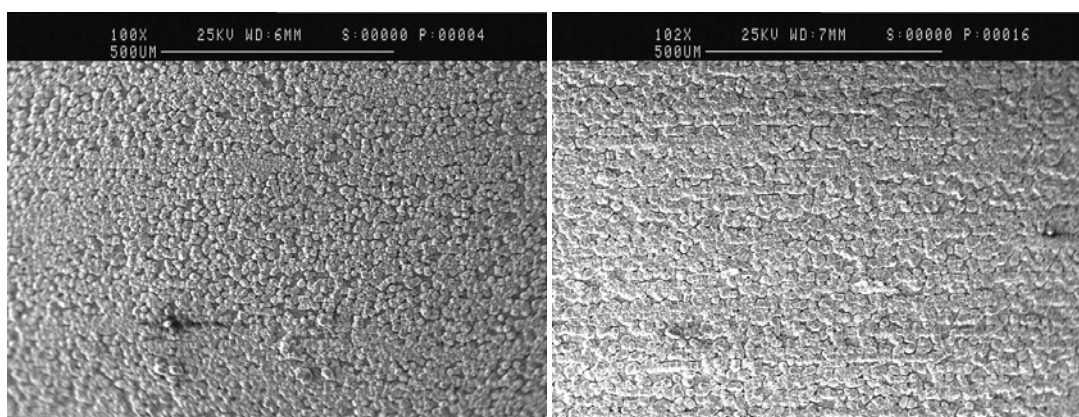


Figure 5. Change of corrosion rate and supersaturation level during iron carbonate layer formation and mechanical removal test in glass cell with rotating cylinder electrode setup, layer formation: pH 6.6, 80°C, initial SS=300, stagnant; layer removal: pH 6.6, initial SS=4, 7000 rpm.

As can be seen from Figure 5, when the working electrode was rotated at 7000 rpm, the test solution remained slightly supersaturated, which ensured that there was limited precipitation and no dissolution of iron carbonate. It was noticed that the corrosion rate showed some fluctuations (probably related to the vibration of the rotating shaft at high speed), but remained low and stable at less than 0.1 mm/yr, which indicated that the iron carbonate layer still remained highly protective. When comparing the specimen surface between “before” and “after” the layer removal at 7000 rpm as shown in Figure 6, it can be seen that there was not much difference in the appearance of the layer surface and most part of the specimen surface was covered with iron carbonate layer both before and after the layer removal process. In other words, there was no mechanical “removal” and the protective layer was not affected by the increased wall shear stress created by flow.



(a) X100 before 7000 rpm

(b) X100 after 7000 rpm

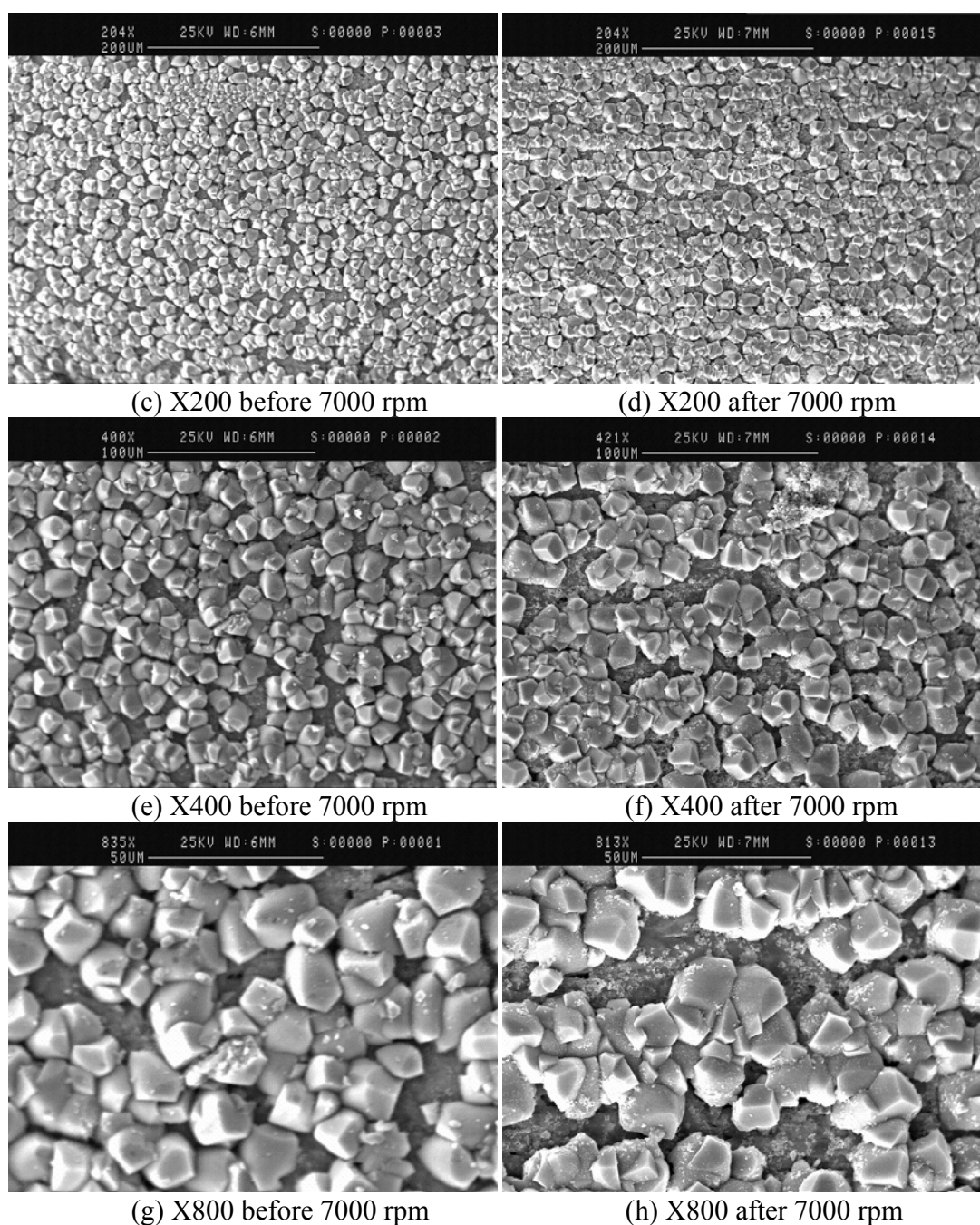


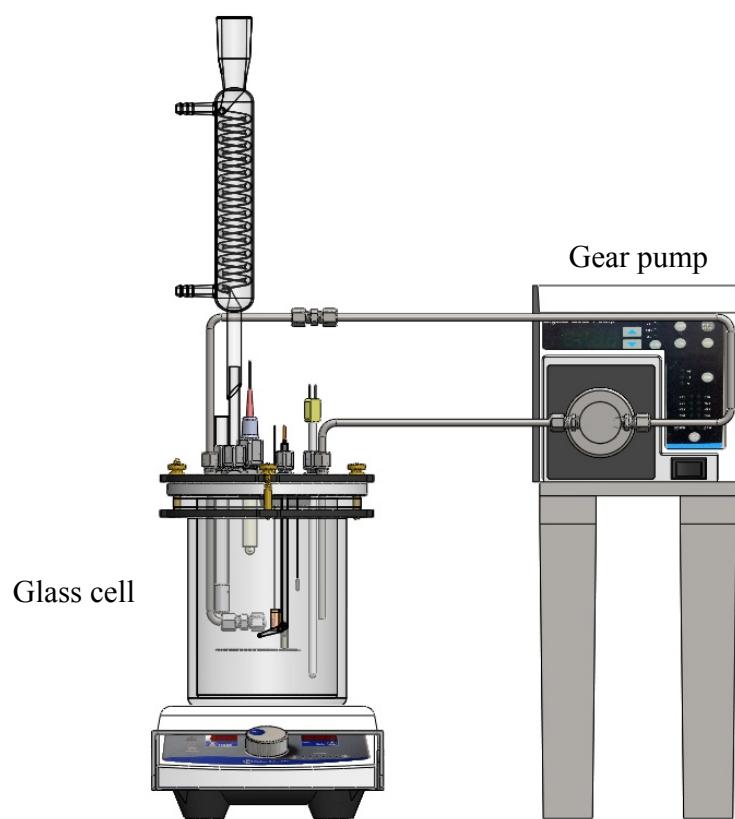
Figure 6. SEM images of specimen surface before and after mechanical removal test of iron carbonate layer in glass cell with rotating cylinder electrode setup, layer formation: pH 6.6, 80°C, initial SS=300, stagnant; layer removal: pH 6.6, initial SS=4, 7000 rpm.

### **4.3 Tests done in a glass cell with jet impingement setup**

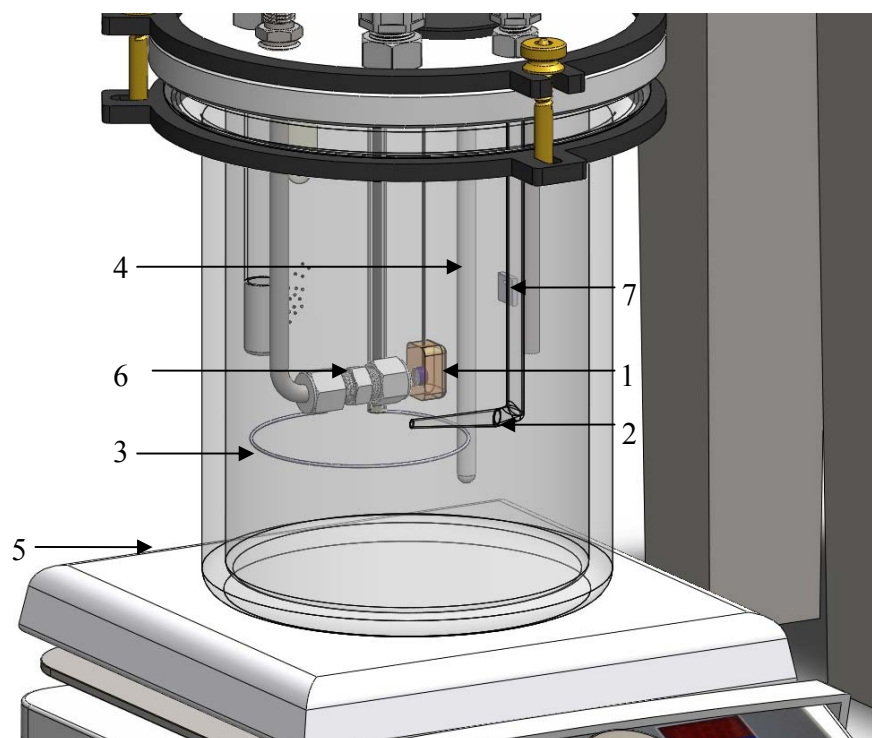
#### *4.3.1 Experimental method*

##### 4.3.1.1 Test setup

In order to test under more severe turbulent flow conditions, and to avoid centrifugal forces, a submerged jet impingement test setup was constructed, as shown in Figure 7. The working electrode was a circular carbon steel specimen (exposed surface area 1.4 cm<sup>2</sup>) electrically connected with copper wire and sealed in epoxy. A concentric platinum ring served as the counter electrode. A saturated Ag/AgCl reference electrode was externally connected to the cell *via* a Luggin capillary through a porous vicor-tip. A pH meter was used to monitor the solution pH during the test. The test solution in the glass cell was circulated by a gear pump through quarter inch tubing to the jet nozzle. The diameter of the jet nozzle was 1 mm and the distance from the jet nozzle to the specimen surface was 5 mm.



(a) The complete setup



(b) Zoom in of glass cell

Figure 7. Schematic of a glass cell with jet impingement setup (courtesy of Cody Shafer). 1-working electrode (circular specimen sealed in epoxy); 2-Luggin capillary; 3-counter electrode 4-thermo probe; 5-heater; 6-jet impingement; 7-additional carbon steel specimen.

#### 4.3.1.2 Test matrix

The test matrix of iron carbonate formation and removal tests conducted in glass cell with jet impingement setup is shown in Table 5.

Table 5. Text matrix for iron carbonate layer formation and removal in a glass cell with jet impingement setup.

Parameter	Layer formation	Layer removal
Material	Carbon steel C1018	
Test solution	1 wt% NaCl	
Temperature	80°C	
CO <sub>2</sub> partial pressure	0.52 bar	
Solution pH	6.6; 7.0	
Initial supersaturation of FeCO <sub>3</sub>	300; 0	
Wall shear stress	0	4 Pa; 175 Pa

#### 4.3.1.3 Test procedure

Two liters of 1 wt% NaCl solution was prepared and deoxygenated with CO<sub>2</sub> for at least two hours before the specimen was immersed into the solution. During this time, the gear pump was also running and the test solution was circulated through the tubing in order to completely deoxygenate the jet impingement flow loop. Simultaneously, the solution was heated to 80°C. The solution pH was measured using a pH meter and adjusted to the designated pH value by adding deaerated 1 M NaHCO<sub>3</sub> solution. The circulation through the gear pump was stopped. Test specimens (with one additional carbon steel specimen) were prepared with the same procedure shown earlier for the test done in the glass cell with rotating cylinder electrode setup. Test specimens were immersed into the solution and the open circuit potential was monitored. The corrosion rate was also measured by LPR and solution resistance was measured by EIS. An

additional ferrous ion source was added to the solution when necessary according to the test matrix. The solution was held stagnant during the iron carbonate layer formation process. When the corrosion rate decreased to less than 0.1 mm/year, the layer formation process was finished. The additional test specimen was taken out of the solution and stored properly for surface analysis. The gear pump was started and the jet velocity was adjusted to the desired value according to the test matrix. The corrosion rate and corrosion potential were measured during the layer removal process. The ferrous ion concentration was measured regularly during the test. When the test was finished, the jet flow was stopped and the test specimen was taken out from the solution for surface analysis with scanning electron microscope (SEM) and energy dispersive X-Ray spectrometer (EDS).

#### *4.3.2 Results and discussion*

##### *4.3.2.1 Layer formation at pH 6.6 and layer removal at 1.3 m/s jet velocity*

Figure 8 shows the change of corrosion rate and corrosion potential of a carbon steel sample (C1018) under a jet flow with a 1.3 m/s average jet velocity. Initially the corrosion rate was around 0.8 mm/year and corrosion potential was about -680 mV. A layer of protective iron carbonate was formed on the specimen surface due to the high supersaturation level, which resulted in the decrease of corrosion rate. Supersaturation with respect to iron carbonate decreased from 300 to around 28 due to the consumption of ferrous ion by iron carbonate precipitation. When the corrosion rate decreased to about 0.1 mm/year, the layer formation process was finished, the additional specimen was taken out and SEM was used to take images of the layer surface, as shown in Figure 9.

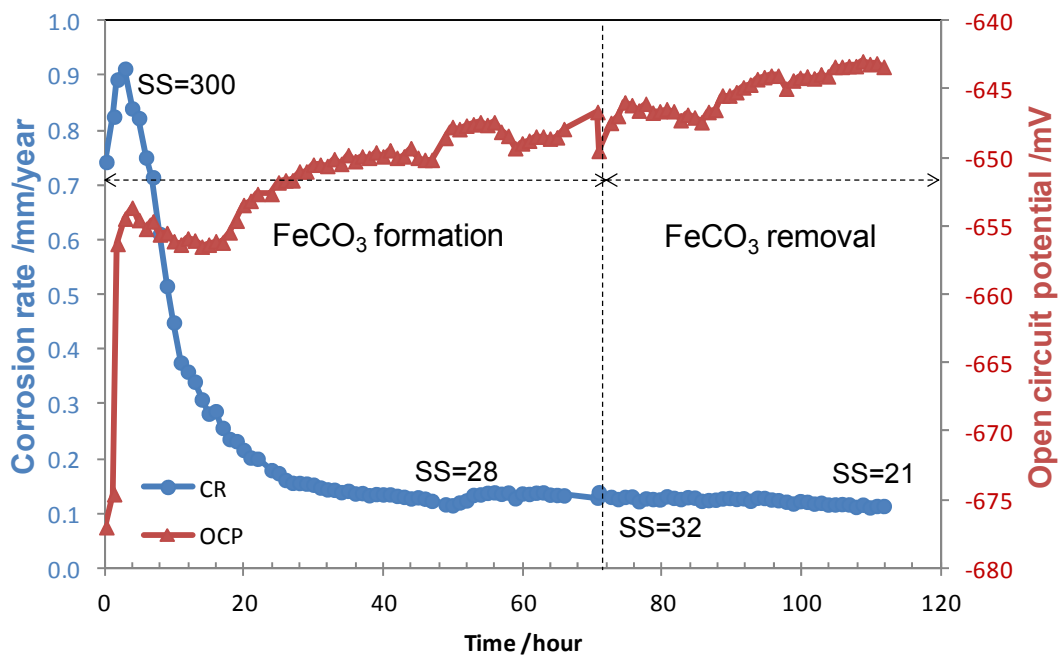


Figure 8. Change of corrosion rate and corrosion potential during layer formation and mechanical removal test in glass cell with jet impingement setup, layer formation: 80°C, pH 6.6, initial SS=300, stagnant, layer removal: pH 6.6, jet velocity 1.3 m/s.

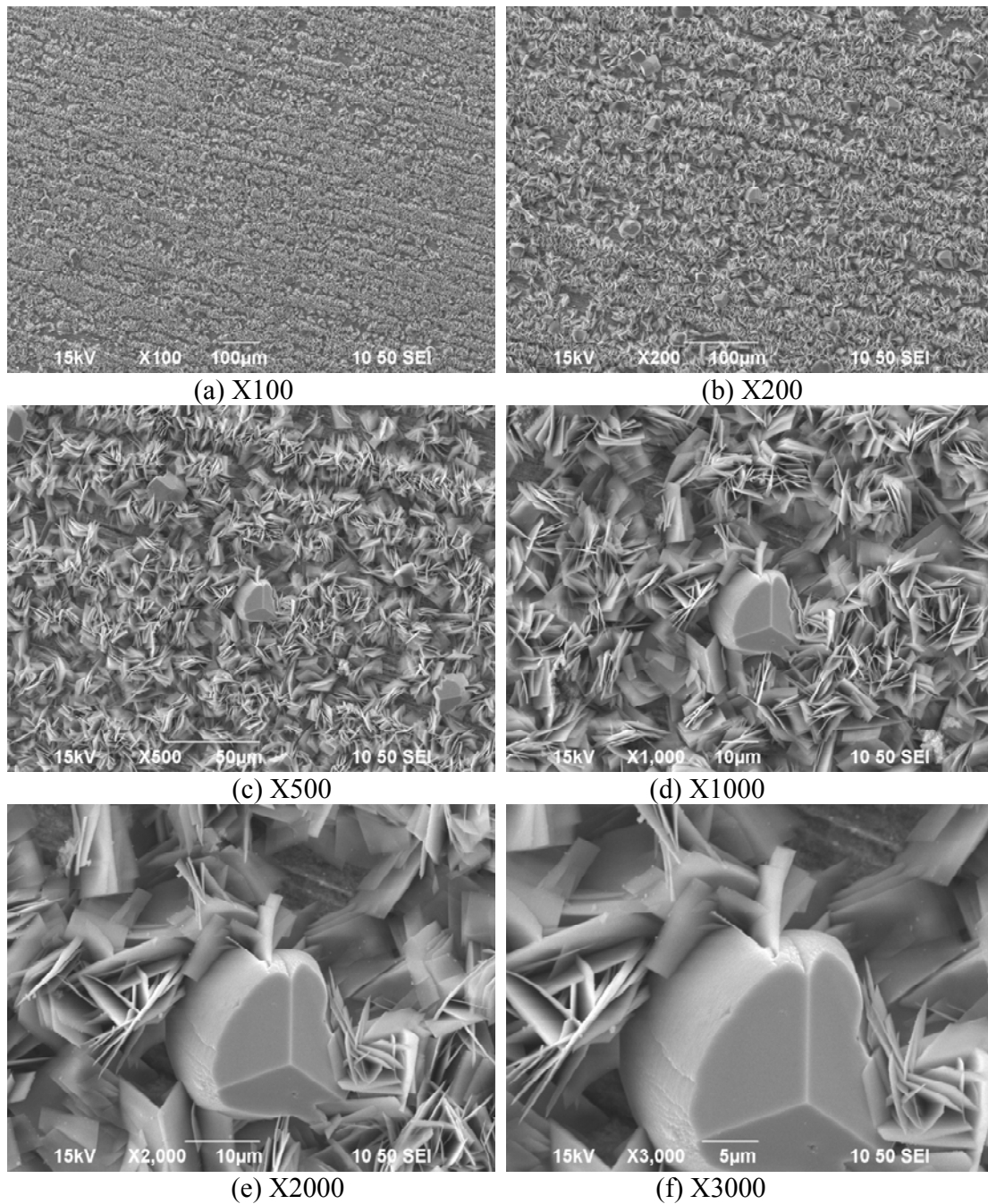


Figure 9. SEM images taken after on specimen surface after iron carbonate layer formation, pH 6.6, 1 wt% NaCl, initial SS=300, 80°C, stagnant.

An impinging jet flow with 1.3 m/s jet velocity was started after the protective iron carbonate layer was formed and the supersaturation of iron carbonate remained

around 30. The jet flow distributed on the specimen surface can be characterized with three flow region with respect to the radial distance from the center line of the jet flow, stagnant region, transition region and wall jet region as illustrated in Figure 10.

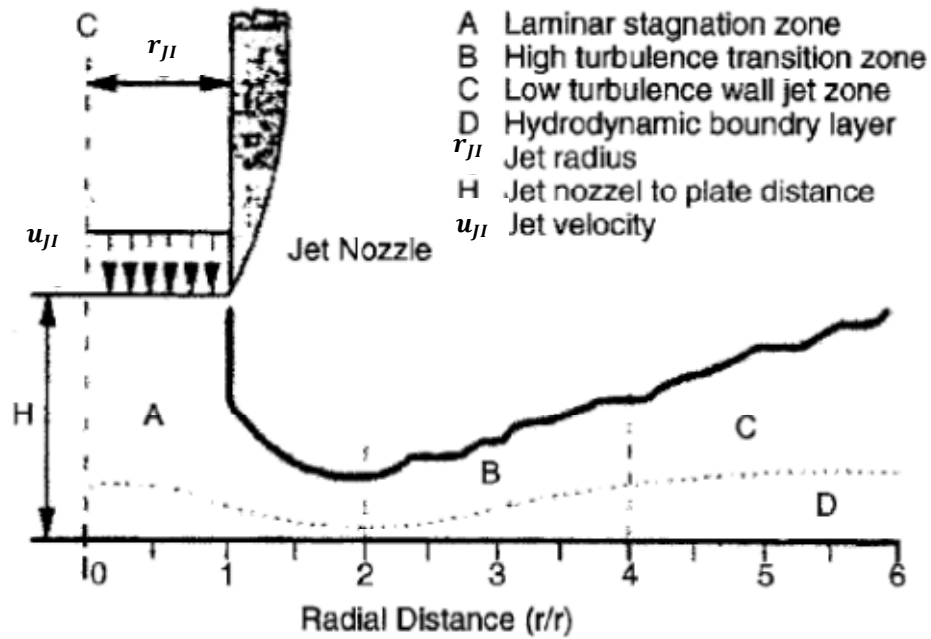


Figure 10. Schematic illustration of hydrodynamic flow region of impinging jet distributed on specimen surface (Dawson & Shih, 1987).

The shear stress in wall jet region can be calculated using the following equation (Giralt & Trass, 1975; Giralt & Trass, 1976):

$$\tau_{JI} = 0.179\rho u_{JI}^2 Re_{JI}^{-0.182} \left(\frac{r}{r_{JI}}\right)^{-2.0} \quad (22)$$

$$Re_{JI} = \frac{2r_{JI}u_{JI}}{\gamma} \quad (23)$$

where  $\tau_{JI}$  is the wall shear stress created by jet impingement flow,  $Re_{JI}$  is the Reynolds number,  $\rho$  is the density of the solution,  $r_{JI}$  is the radius of the jet nozzle,  $r$  is the distance

from the jet flow center line,  $u_{JI}$  is the flow velocity at the jet nozzle,  $\gamma$  is the kinematic viscosity of the solution.

As observed in Figure 8, after the 1.3 m/s jet flow (maximum shear stress in wall jet region equal to 4 Pa) was started, there was no significant change in corrosion rate and the corrosion potential also stayed at the same level. It was suggested that the increased jet flow did not affect the protectiveness of the iron carbonate layer. SEM images taken with different magnifications after the test was finished further proved the above hypothesis, as shown in Figure 11 (wall jet region) and Figure 12 (transition region). There was an evenly covered iron carbonate layer on the surface and the appearance of the layer was very similar to what was seen in Figure 9.

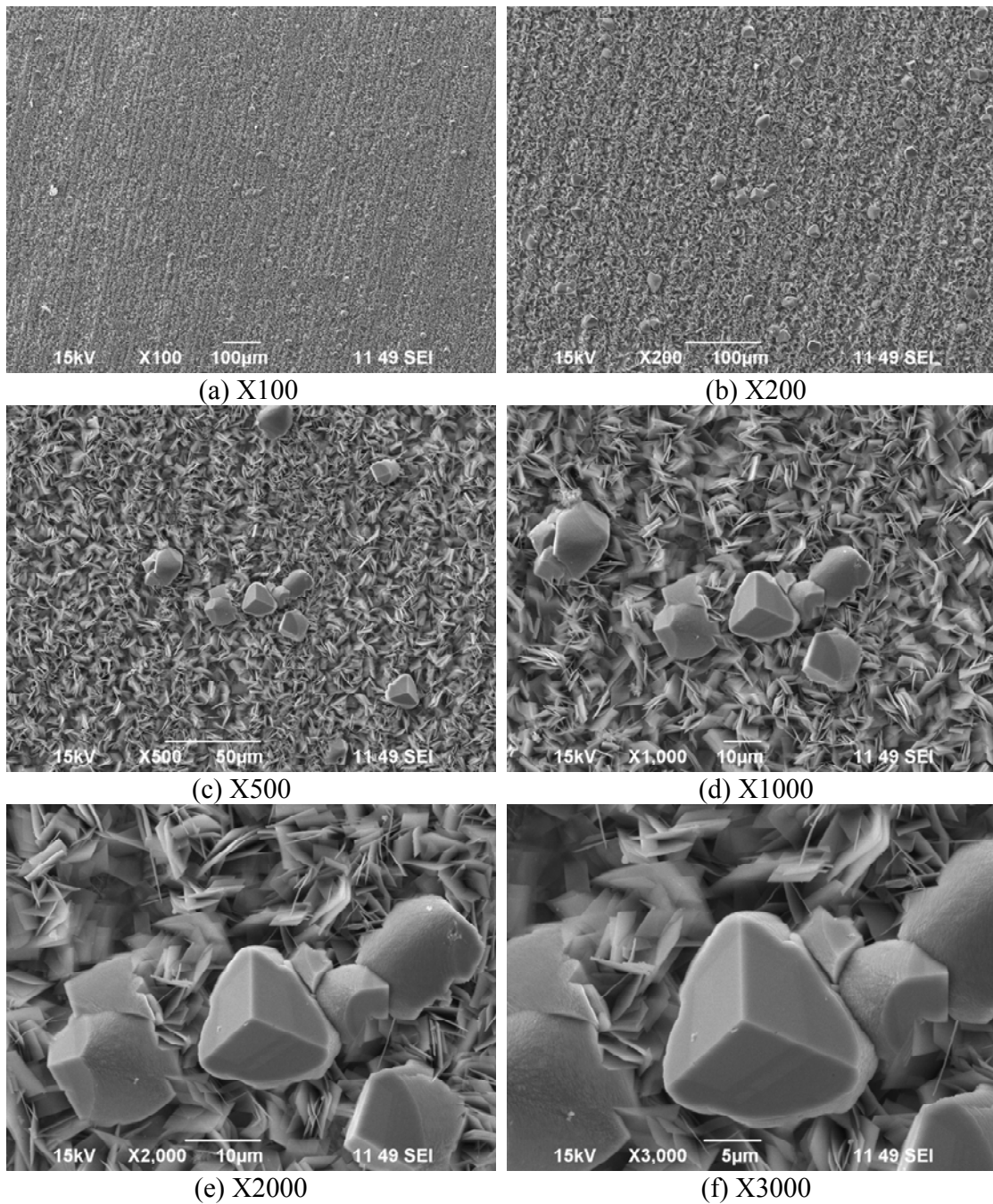


Figure 11. SEM images taken on carbon steel specimen surface after layer removal under jet impingement (wall jet region), pH 6.6, 1 wt% NaCl, initial SS=300, 80°C, jet flow velocity 1.3 m/s.

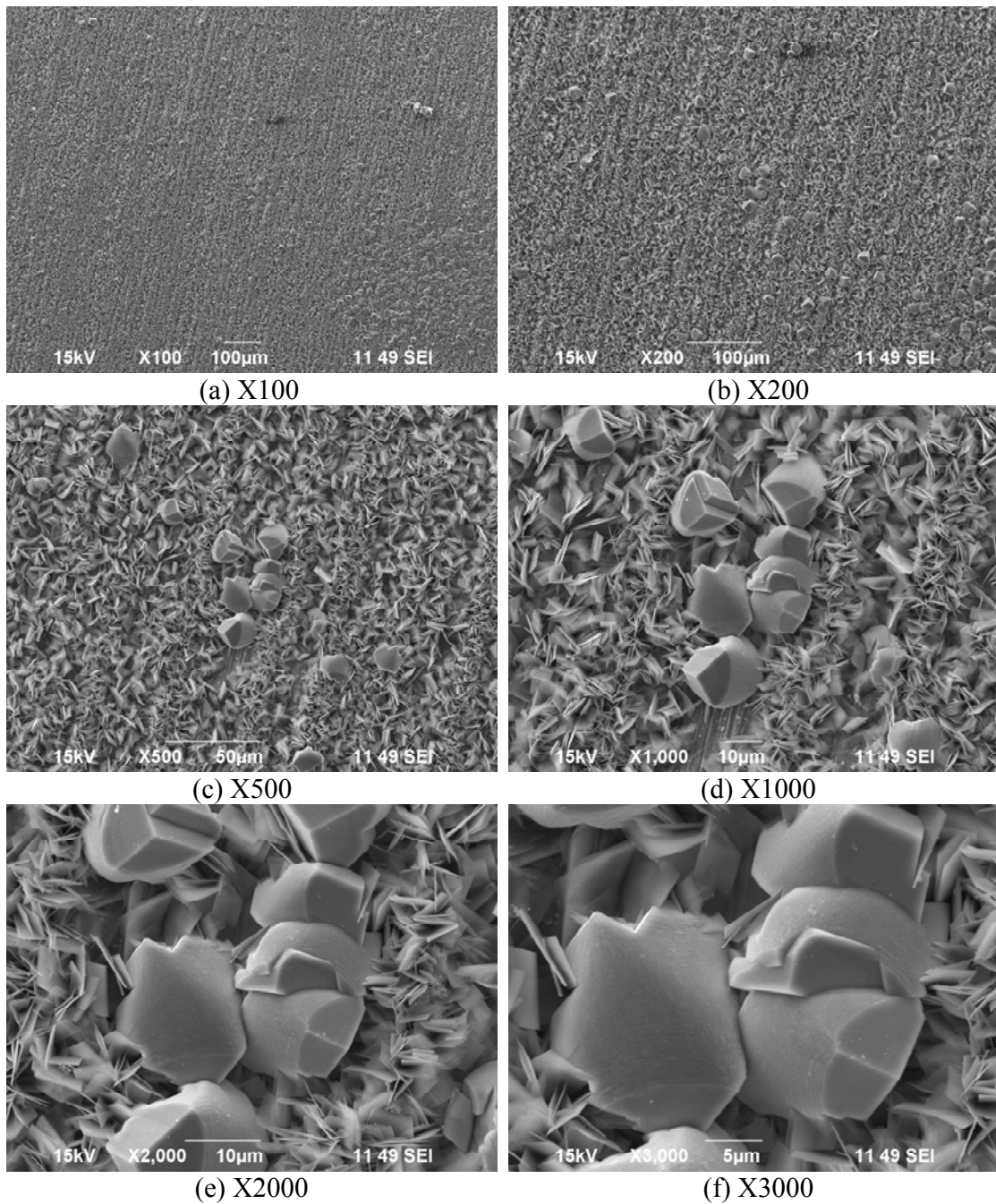


Figure 12. SEM images taken on carbon steel specimen surface after layer removal under jet impingement (transition region), pH 6.6, 1 wt% NaCl, initial SS=300, 80°C, jet flow velocity 1.3 m/s.

#### 4.3.2.2 Layer formation at pH 6.6 and layer removal at 10.6 m/s jet velocity

In order to further prove the results, a higher jet flow rate was used in another jet impingement test. The change of corrosion rate and corrosion potential is shown in Figure 13. The layer formation condition was the same as in previous tests. The corrosion rate decreased and the corrosion potential increased when the protective iron carbonate layer formed on the steel surface. The supersaturation of the solution spontaneously decreased to around 10 after 40 hours and maintained under this condition. SEM pictures were taken on the sample surface after the layer formed and are shown in Figure 14. An evenly covered iron carbonate layer was observed on the specimen surface.

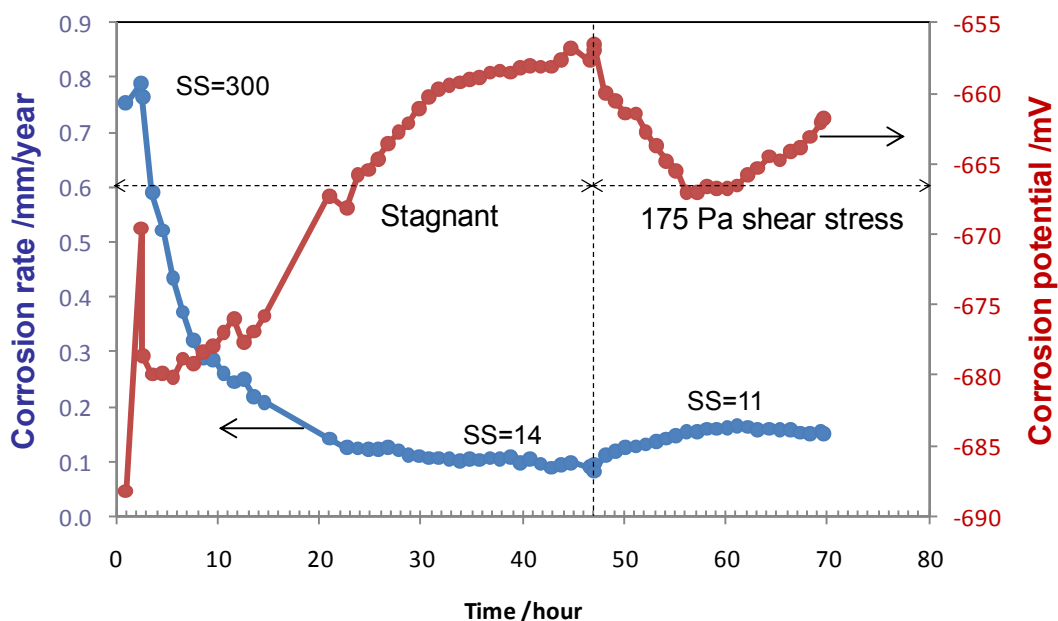


Figure 13. Corrosion rate and corrosion potential change of carbon steel sample under jet impingement, pH 6.6, 1 wt% NaCl, initial SS=300, jet flow rate 10.6 m/s, 80°C.

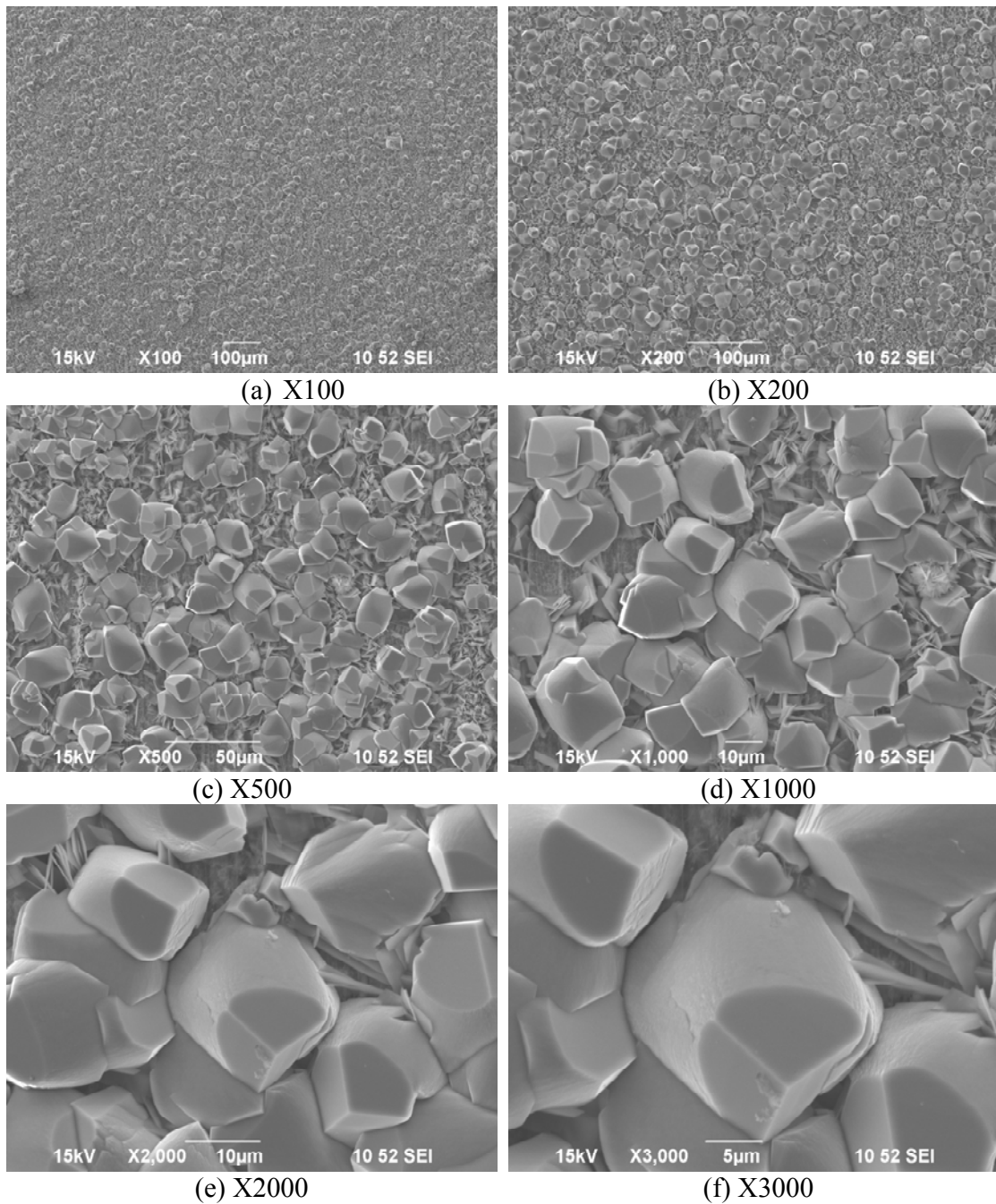
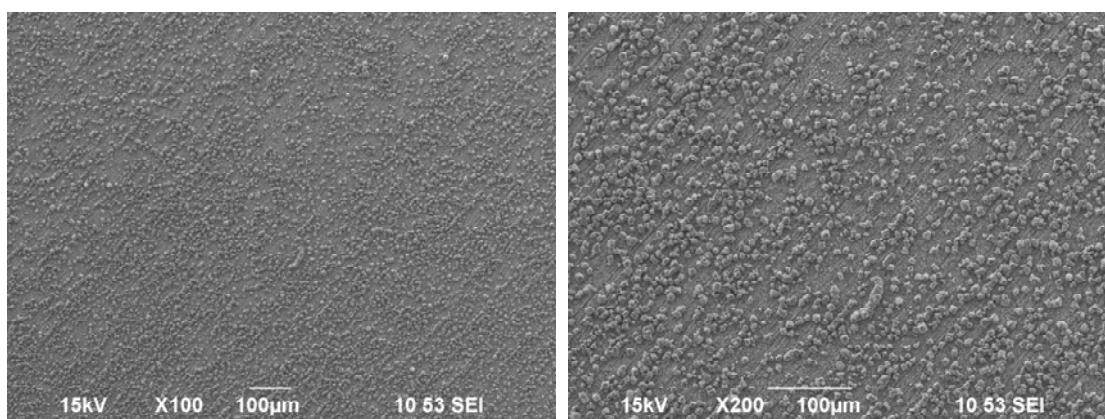


Figure 14. SEM pictures taken after layer formation on carbon steel specimen surface. pH 6.6, 1 wt% NaCl, initial SS=300, 80°C, stagnant.

When the layer formation process was finished, a jet flow with 10.6 m/s was started, which is equal to 175 Pa maximum wall shear stress in the wall jet region of the

jet impingement flow on the specimen surface. As shown in the graph, the corrosion rate just increased a little, from 0.1 mm/year to about 0.15 mm/year and stayed stable. This suggested that the iron carbonate layer remained protective under the highly turbulent jet flow. Figure 15 and Figure 16 show the SEM images (X100 to X3000) taken on the specimen surface in the wall jet region and transition region respectively. The appearance of the specimen surface was similar in these figures, featuring a loss of both the prism shaped and the plate shaped iron carbonate. Note that in the close up SEM images (Figure 15 f), some of the support structures for the flake shape iron carbonate can be observed in the area between the prism shapes indicating the “underlying thin adhesive layer” was still intact. As can be seen in Figure 15 (g) (h) on the EDS pictures, there were Fe, C and O peaks detected by EDS, which is supporting the notion that the adhesive thin layer is composed of iron carbonate, which provided protection to the underneath carbon steel surface when the large size iron carbonate were removed by the jet flow.



(a) X100

(b) X200

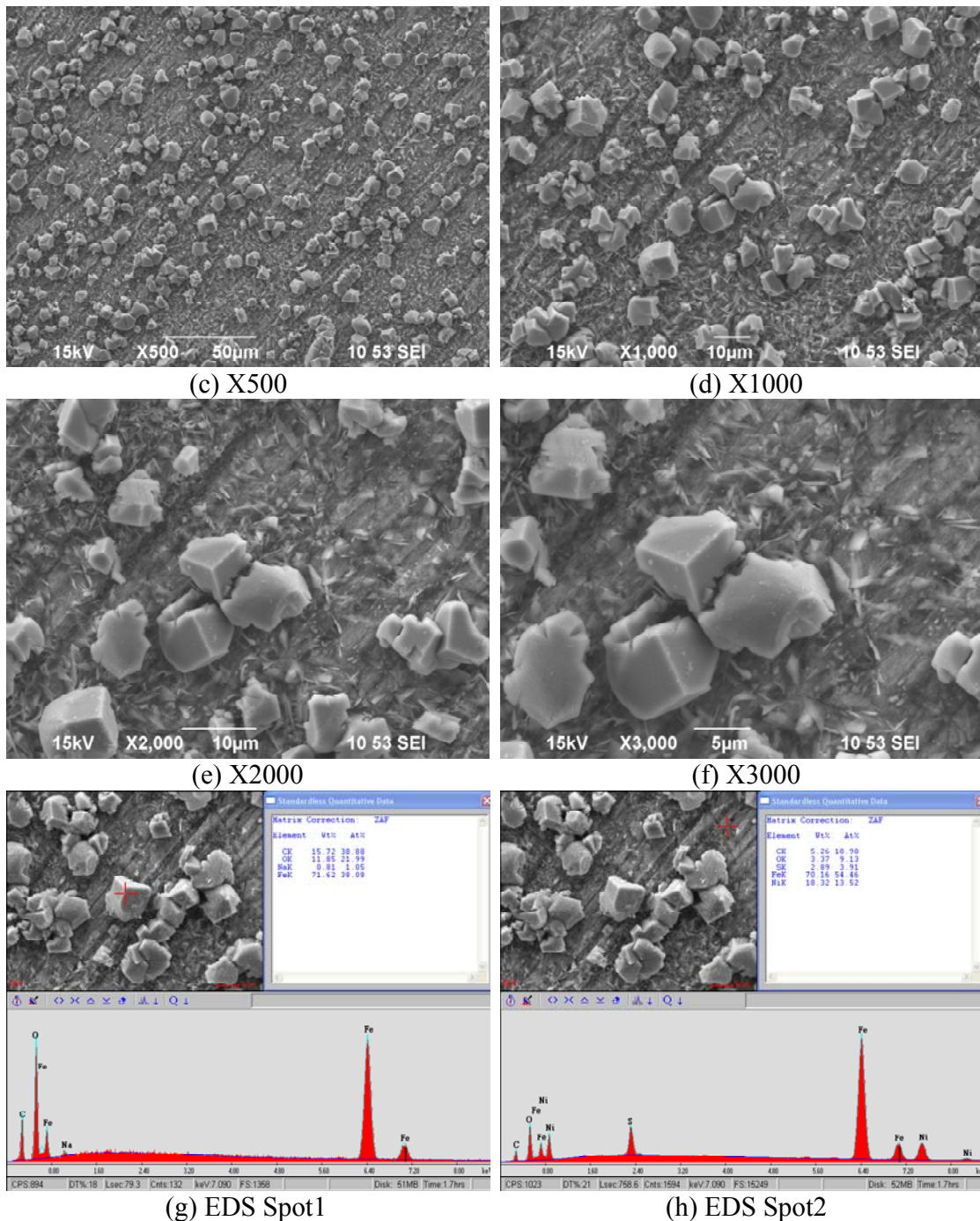


Figure 15. SEM and EDS images taken after layer removal under jet impingement on carbon steel specimen surface (wall jet region). pH 6.6, 1 wt% NaCl, initial SS=300, 80°C, jet flow velocity 10.6 m/s.

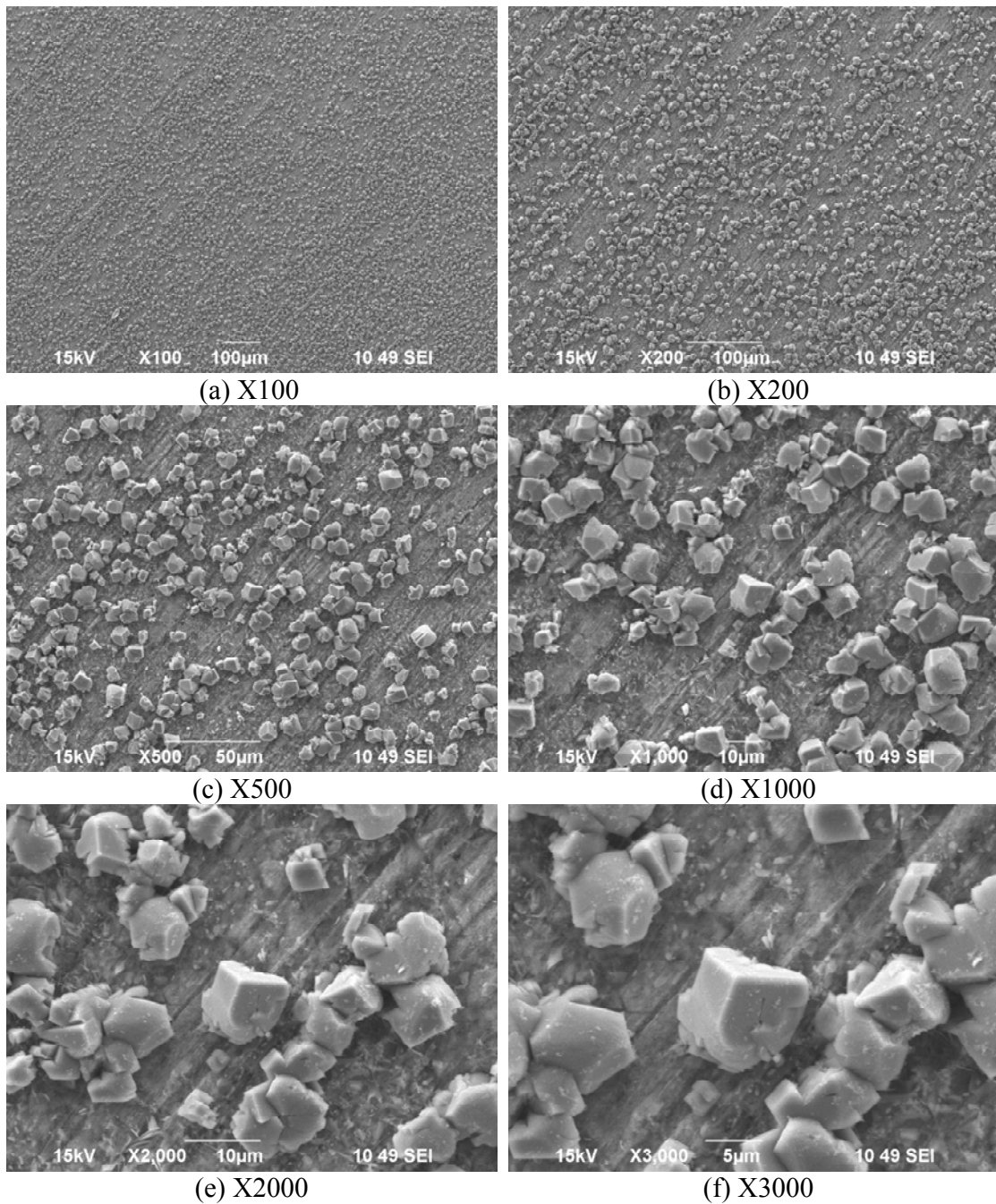


Figure 16. SEM images taken after layer removal under jet impingement on carbon steel specimen surface (transition region). pH 6.6, 1 wt% NaCl, initial SS=300, 80°C, jet flow velocity 10.6 m/s.

#### 4.3.2.3 Layer formation without additional $Fe^{2+}$ and layer removal at 10.6 m/s jet velocity

In all the above cases, additional  $Fe^{2+}$  was added to the solution during the layer formation process, which would accelerate the iron carbonate precipitation by increasing the supersaturation of iron carbonate. However, it is not the same situation as in the field. Therefore one more test was conducted without adding additional  $Fe^{2+}$ , in order to simulate the “real” layer formation condition. The change of corrosion rate and corrosion potential during this test was shown in Figure 17. Initially, the corrosion rate was around 1 mm/year and corrosion potential was low ( $\sim 700$  mV). As the steel kept corroding in the corrosive  $CO_2$  environment,  $Fe^{2+}$  was released and the solution became supersaturated, especially near the steel surface. Therefore, it was possible that iron carbonate could precipitate from the solution and form a protective layer on the steel surface. As can be seen in Figure 17, the corrosion rate did decrease which proved the formation of the protective layer and the corrosion potential also increased, which is corresponding to the formation of a pseudo passive layer formed on the steel surface at the same time. A jet flow was introduced to the surface after a protective layer formed stably on the surface. It is noticed that the corrosion rate and corrosion potential fluctuated a little bit in the beginning, but soon stabilized at similar values as if nothing happened, which indicated that the flow didn't have a significant effect on the protectiveness of the corrosion product layer.

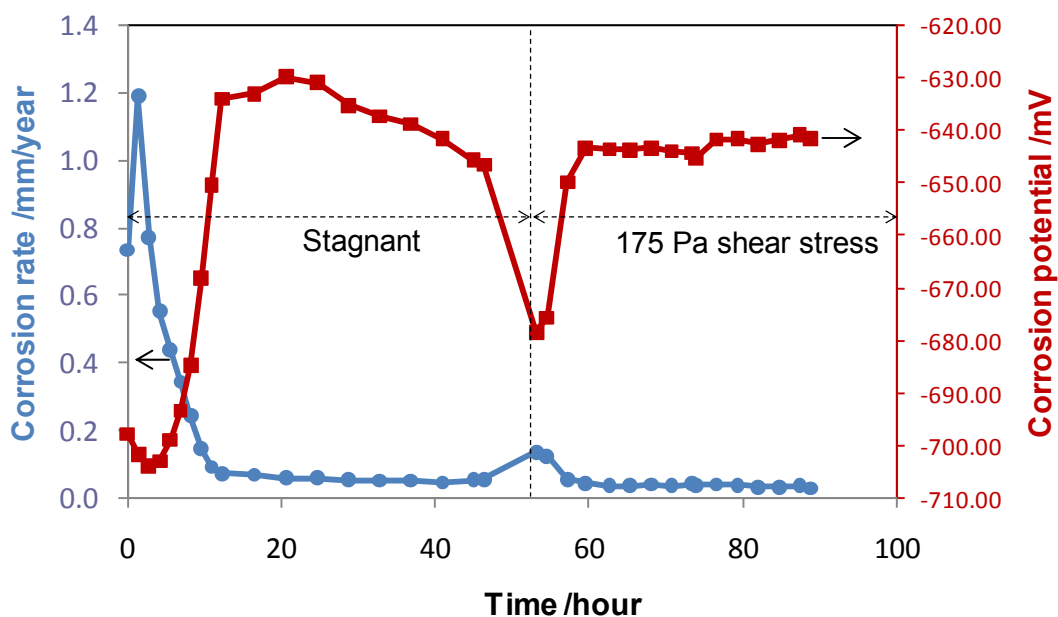


Figure 17. Corrosion rate and corrosion potential change of carbon steel sample under jet impingement, pH 7.0, 1 wt% NaCl, initial SS=0, jet flow rate 10.6 m/s, 80°C.

The SEM and EDS taken before and after the start of jet flow is shown in Figure 18 and Figure 19. It is noticed that the protective iron carbonate layer was formed before the jet flow started and protected the surface very well. In the SEM pictures taken after the jet flow (Figure 19), it is shown that many prism shaped iron carbonate were gone. When taking a look at the EDS picture, it shows that the locations, which look like bare steel surface, still have strong carbon and oxygen peaks. This indicated that underneath the prism shaped iron carbonate layer, there is still a very adhesive iron carbonate layer, protecting the surface. This layer is strong, adhesive and protective and limits the steel surface from further corrosion and was not affected by flow. The SEM pictures of sample cross sections before and after the jet flow are shown in Figure 20 and Figure 21. These clearly demonstrate the above assumption. There is still a thin, but adhesive, layer left on the surface after the jet flow was started and this layer was not damaged by the flow.

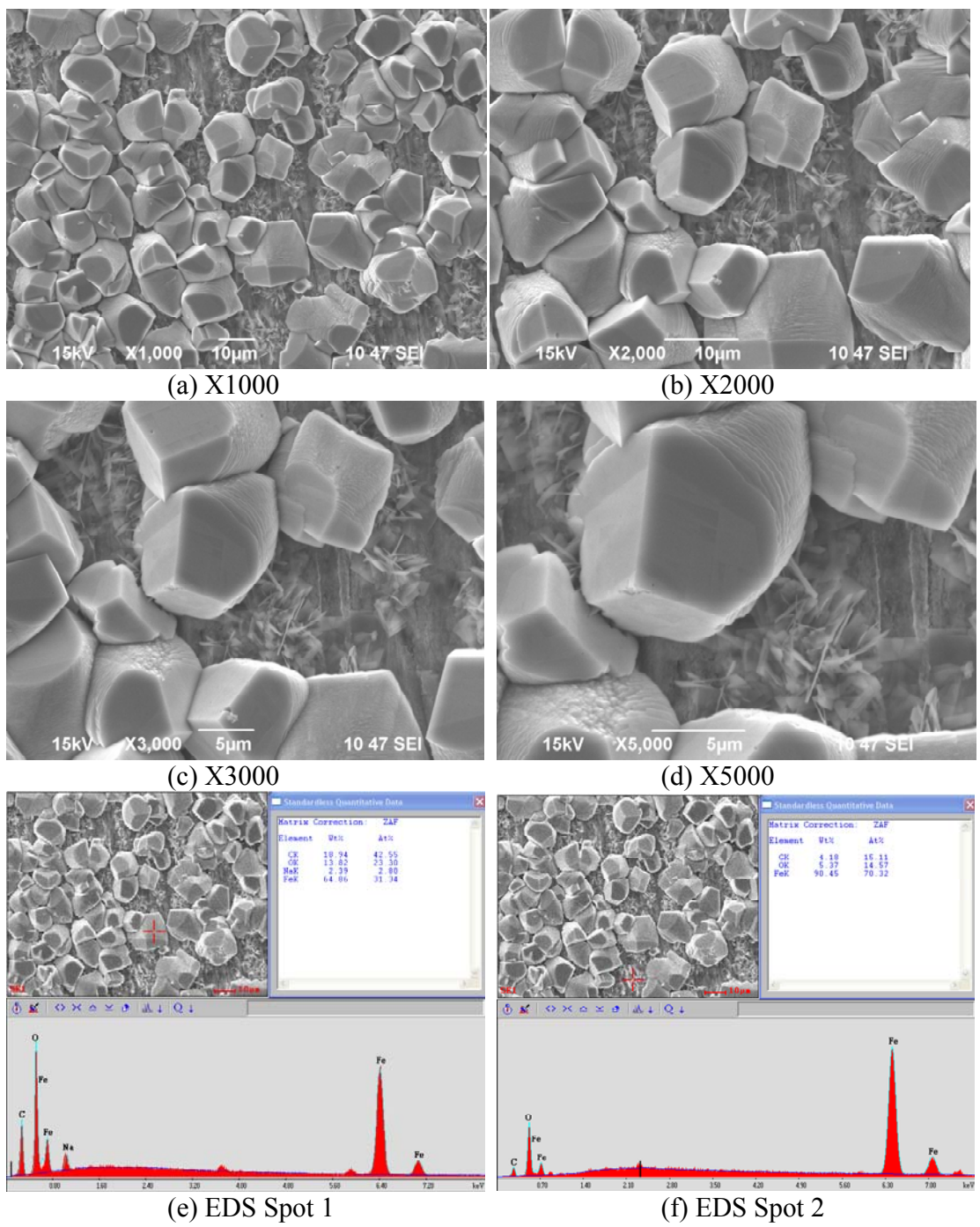


Figure 18. SEM and EDS pictures taken before layer removal under jet impingement on carbon steel sample surface. pH 7.0, 1 wt% NaCl, initial SS=0, jet flow rate 10.6 m/s, 80°C.

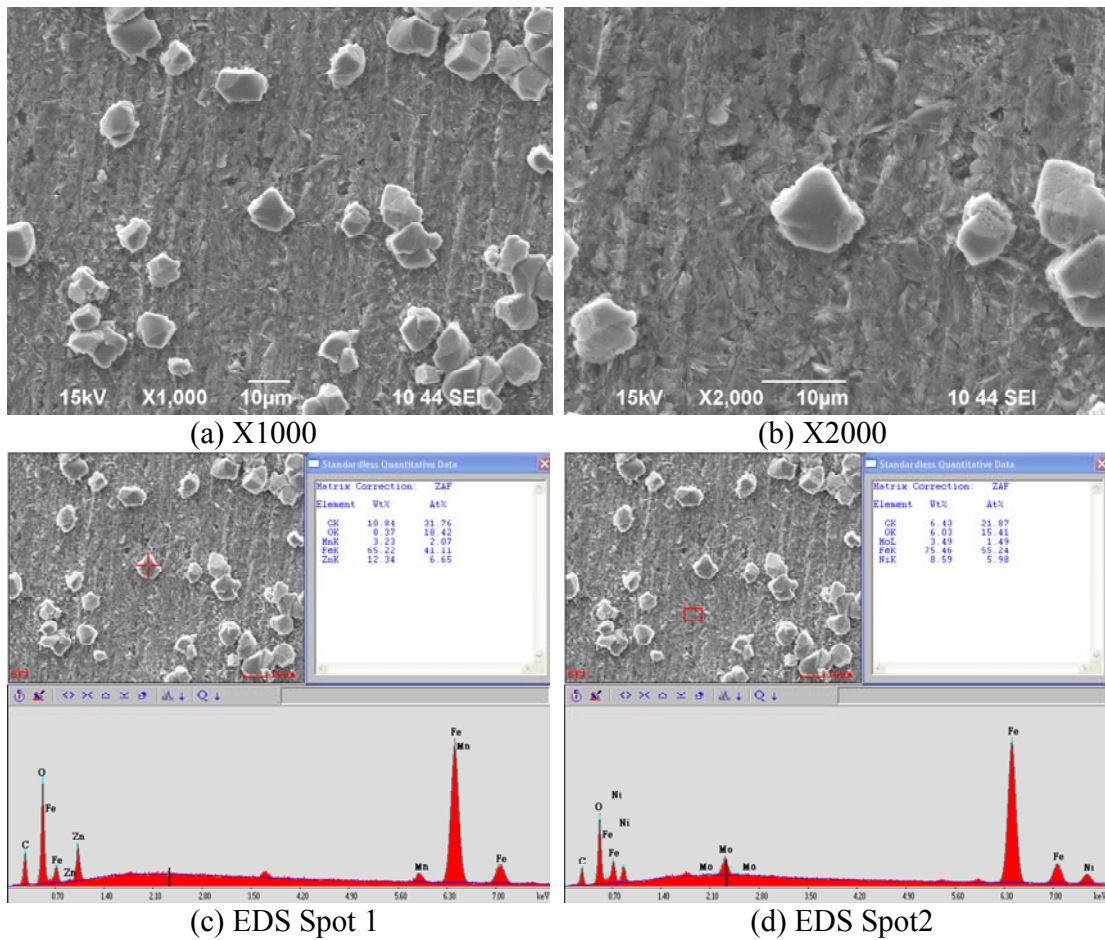


Figure 19. SEM and EDS images taken after layer removal under jet impingement on carbon steel sample surface. pH 7.0, 1 wt% NaCl, initial SS=0, jet flow rate 10.6 m/s, 80°C.

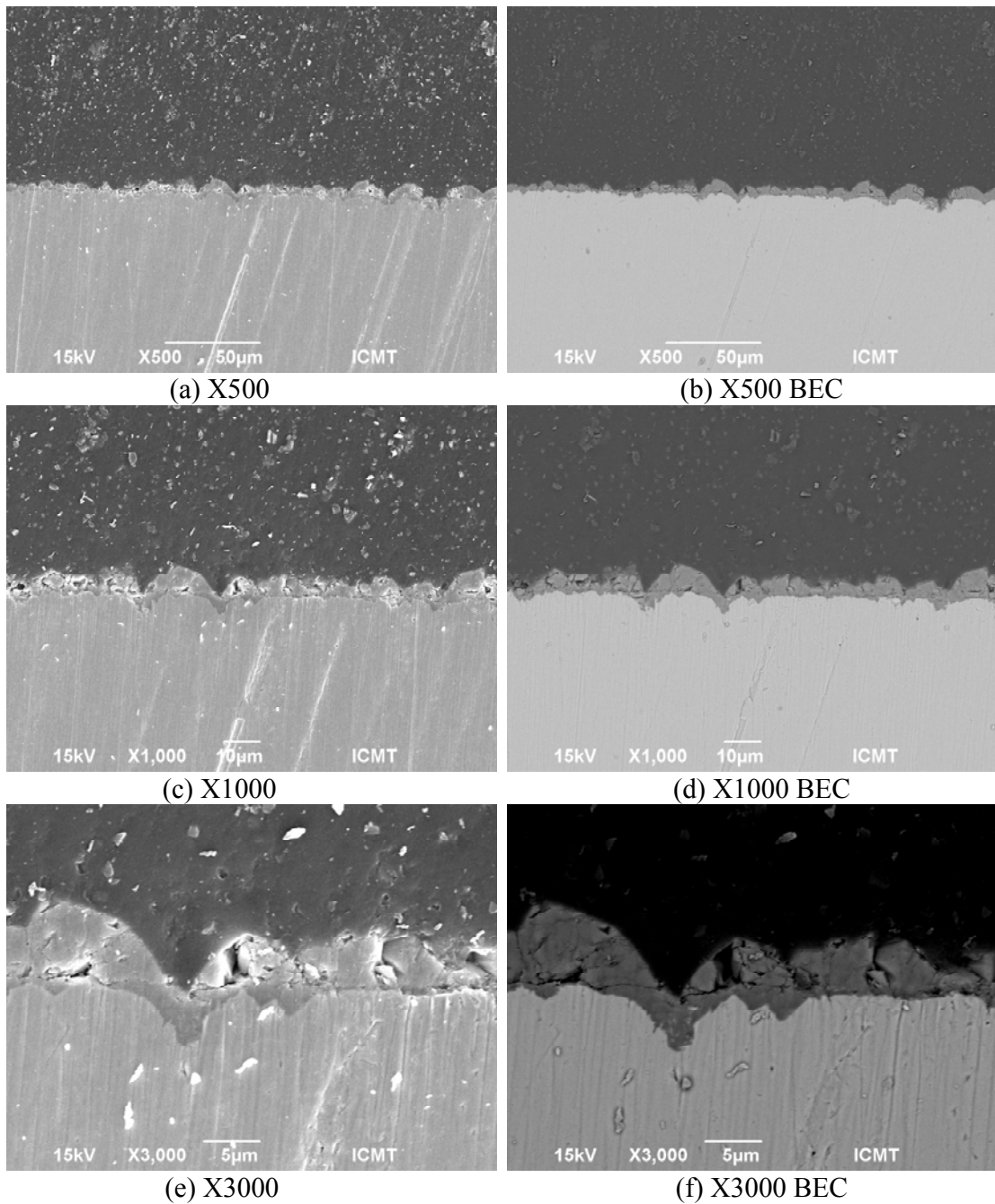
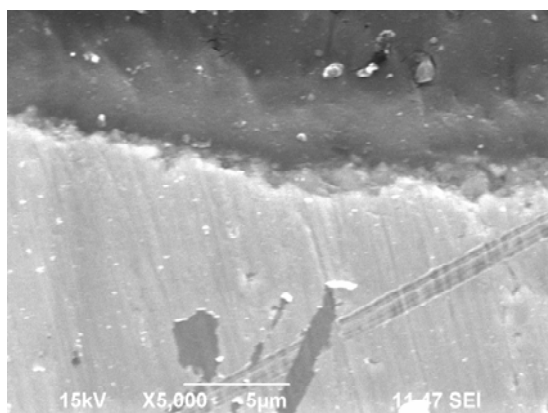
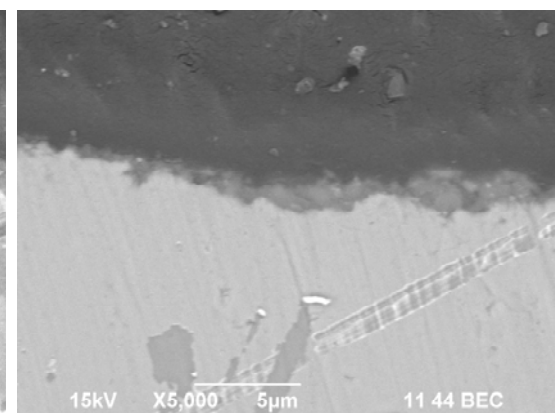


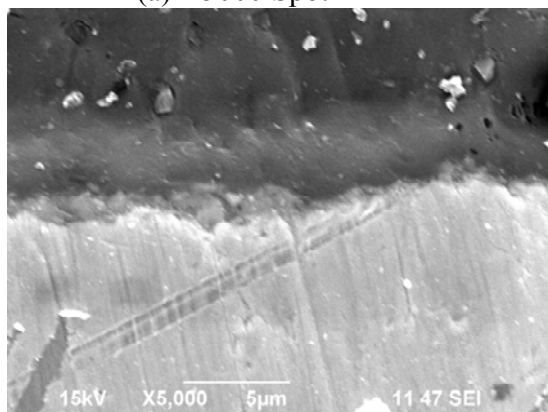
Figure 20. SEM of cross section taken before layer removal under jet impingement on carbon steel sample surface. pH 7.0, 1 wt% NaCl, initial SS=0, jet flow rate 10.6 m/s, 80°C. “BEC” stands for backscattered electron beam. A secondary electron beam was used in all other images when it was not pointed out specifically.



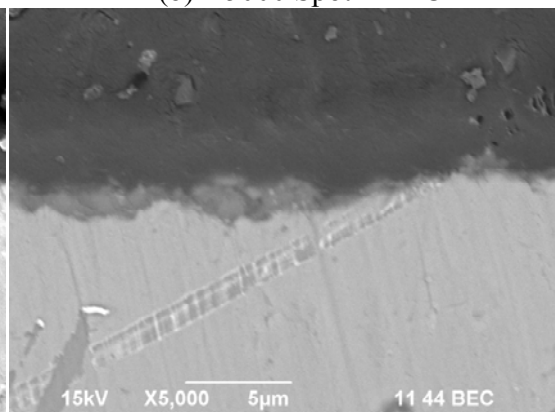
(a) X5000 Spot 1



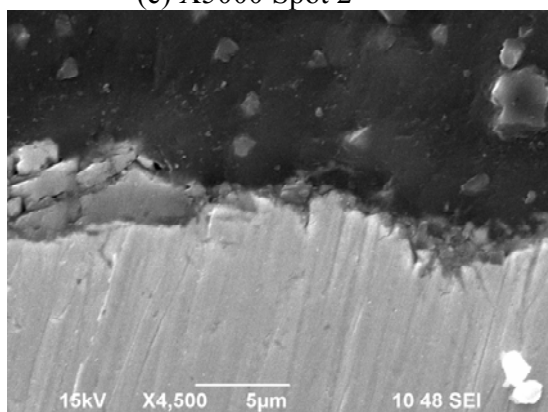
(b) X5000 Spot 1 BEC



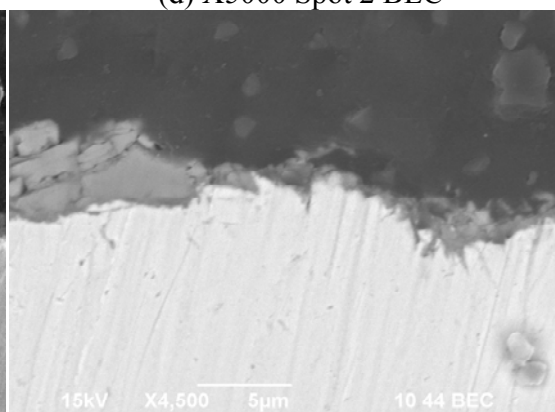
(c) X5000 Spot 2



(d) X5000 Spot 2 BEC



(e) X5000 Spot 3



(f) X5000 Spot 3 BEC

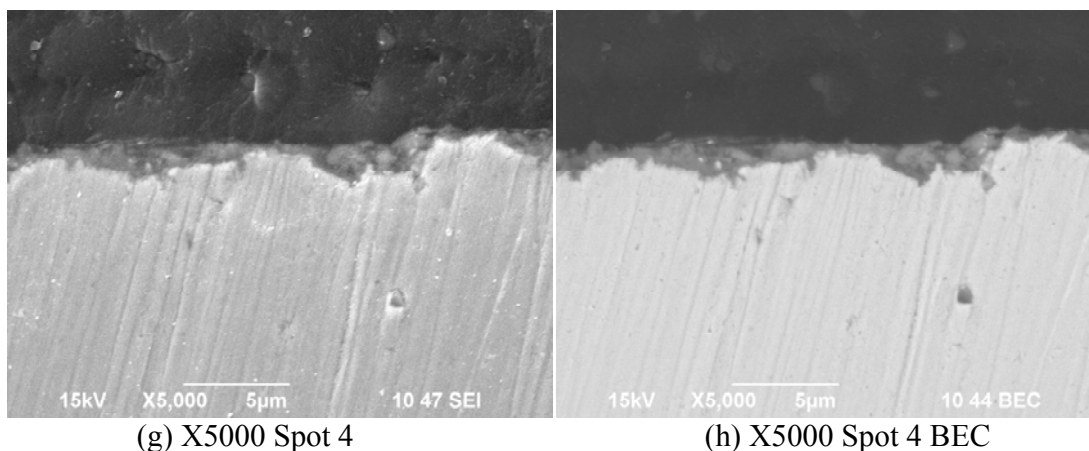


Figure 21. SEM images of cross section taken after layer removal under jet impingement on carbon steel specimen surface, pH 7.0, 1 wt% NaCl, initial SS=0, jet flow rate 10.6 m/s, 80°C.

#### 4.4 Tests done in the thin channel flow cell system

##### 4.4.1 Experimental method

##### 4.4.1.1 Test setup

A flow chart of thin channel flow cell (TCFC) system, which was originally designed and built for this study, is shown in Figure 22 and a schematic drawing of the test section is shown in Figure 23. The test section of the TCFC system includes a rectangular flow channel (3 mm high and 100 mm wide). There are four ports in the test section and each port can be mounted with a test probe, which can be a weight loss (WL) specimen, an LPR probe or an ER probe. The dimension of the flow channel and the alignment of the probes were carefully chosen to make sure that there was no edge effect and that turbulent flow has been fully developed at the location of the test probes. The test solution was prepared in the tank and circulated in the TCFC system by using a centrifugal pump. A flow meter was installed to monitor the flow rate inline. The temperature of the system was controlled by an electric heater and a cooling heat

exchanger. Several bypass flow line can be used to make pH measurement, adjustment or take solution sample. There were several ports that can be connected to CO<sub>2</sub> gas line to make sure the system was deoxygenated.

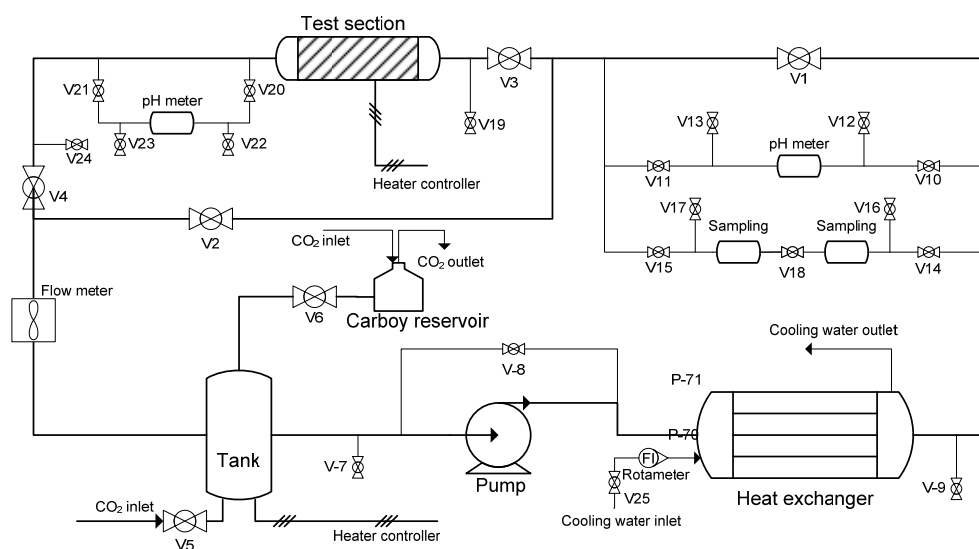
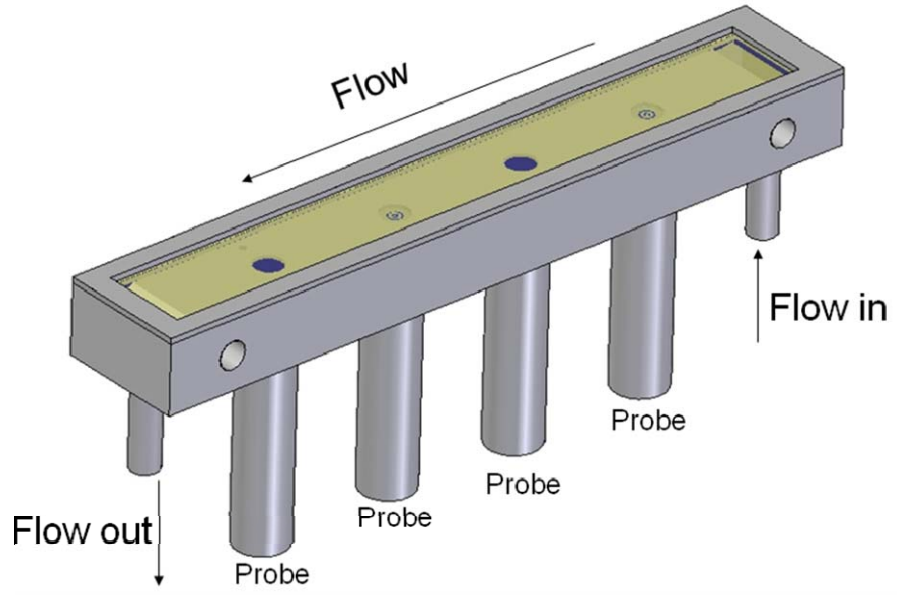
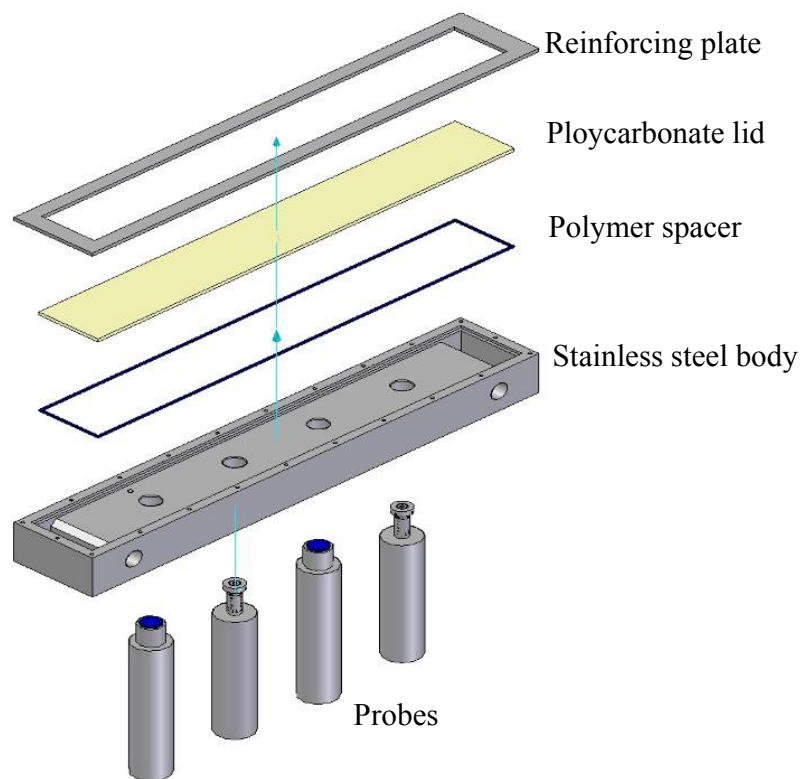


Figure 22. Flow chart of thin channel flow cell system.



(a) Assembled view



(b) Exploded view

Figure 23. Schematic of assembled and exploded view of thin channel flow cell system test section.

#### 4.4.1.2 Test matrix

Test matrix for the iron carbonate layer formation and removal test conducted in TCFC system is shown in Table 6 and chemical composition of X65 is shown in Table 7.

Table 6. Text matrix for iron carbonate layer formation and removal in TCFC system.

Parameter	Layer formation	Layer removal
Material	X65	
Solution	1 wt% NaCl	
Temperature	80°C	
CO <sub>2</sub> partial Pressure	0.52 bar	
pH	6.6	
Initial supersaturation	300	
Flow velocity	0.6 m/s	2.9 m/s
Wall shear stress	1 Pa	21 Pa

Table 7. Chemical composition of X65 steel (wt%)

C	Si	Mn	P	S	Cr	Ni	Cu	Al	Mo	Fe
0.05	0.31	1.32	0.013	0.002	0.042	0.039	0.019	0.032	0.031	Balance

#### 4.4.1.3 Test procedure

1 wt% NaCl test solution was prepared in the tank of the TCFC system. The system was deoxygenated by CO<sub>2</sub> gas sparged into the tank and the solution circulated through the system bypassing the test section. The flow channel test section was deoxygenated separately by purging CO<sub>2</sub> gas into the test section. At the same time, the electric heater was turned on to heat the test solution to 80°C. The pH of the solution was then measured and adjusted by adding deoxygenated NaHCO<sub>3</sub> solution through the flow

bypass. The surfaces of LPR probe and WL specimen were prepared by polishing with sand paper, rinsing with isopropyl alcohol in ultrasonic cleaner and drying with blower. The test probes were then mounted into the test section, flush with bottom of the flow channel. The test solution was introduced into the test section with the desired flow rate. The corrosion potential and corrosion rate of the LPR probe were monitored with a potentiostat. A specific amount of deoxygenated  $\text{Fe}^{2+}$  solution was added into the system through the bypass to reach the desired  $\text{Fe}^{2+}$  concentration in the TCFC system. After the corrosion rate of the LPR probe was reduced to less than 0.1 mm/year, one WL specimen was taken out for SEM surface analysis. The flow rate was then increased to a higher value and the corrosion rate and corrosion potential of LPR probe were monitored continuously until the end of the test. The pH change and  $\text{Fe}^{2+}$  concentration was measured periodically during the whole test. At the end, the LPR probe and WL specimen were taken out and prepared for surface analysis. The system was drained, cooled and rinsed with deionized water.

#### *4.4.2 Results and discussion*

All the above tests were conducted in the 20 liter TCFC system, which provided a more realistic pressure driven flow condition. Figure 24 shows the corrosion rate and corrosion potential change during the test in the TCFC system. At the beginning of the test, the corrosion rate measured from the LPR probe was around 1.5 mm/year, which decreased as additional ferrous ions were added. This indicated that a protective layer of layer was formed on the specimen surface due to the high supersaturation with respect to iron carbonate. Corrosion rate of the LPR probe decreased to around 0.1 mm/year at the

end of layer formation process. One WL specimen was taken out of the system and SEM and EDS surface analysis were conducted with pictures shown in Figure 25 (a) (c) and (e).

After a protective layer was formed, flow rate was increased and around 21 Pa wall shear stress was generated on the specimen surface according the calculation made by the following equations:

$$\tau_{TCFC} = \frac{f}{2} \rho u_{TCFC}^2 \quad (24)$$

$$\frac{1}{\sqrt{f}} = -4 \log \left[ \frac{0.27\epsilon}{D_H} + (7/Re_{TCFC})^{0.9} \right] \quad (25)$$

$$Re_{TCFC} = \frac{D_H u_{TCFC}}{\gamma} \quad (26)$$

$$D_H = \frac{2Dh}{D+h} \quad (27)$$

where  $\tau_{TCFC}$  is the wall shear stress in TCFC,  $f$  is friction factor,  $u_{TCFC}$  is the flow velocity in TCFC,  $\epsilon$  is the surface roughness of the specimen,  $D_H$  is the hydraulic diameter,  $Re_{TCFC}$  is the Reynolds number in TCFC,  $D$  is the width of the rectangular channel and  $h$  is the height of the channel.

The supersaturation with respect to iron carbonate decreased to a value in the range between 10 and 20 during the layer formation process. A low corrosion rate and consistent corrosion potential were maintained even after the flow rate was increased, with no indication of change related to the increase of shear stress. From the comparison shown in the SEM analysis, Figure 25, between the pictures of the specimen surface taken before and after the change in shear stress, there was not a significant visual change in the iron carbonate layer appearance. It was noticed that on the specimen surface there

was both prism shaped iron carbonate covered area and uncovered area. With the aid of EDS analysis, there was also Fe, C and O detected shown that the prism free area was also possibly covered by different shape of iron carbonate and therefore the corrosion rate of the specimen remained very low.

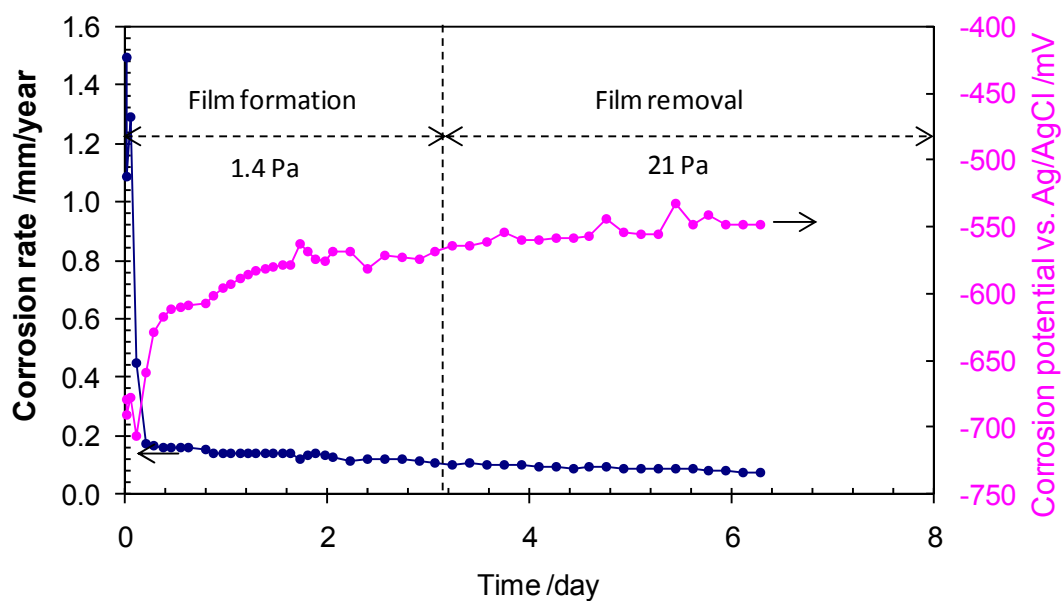


Figure 24. Change of corrosion rate and corrosion potential during the iron carbonate layer formation and mechanical removal test in TCFC, 80°C, pH 6.6, 1 wt% NaCl, initial SS=300, wall shear stress of flow 21 Pa.

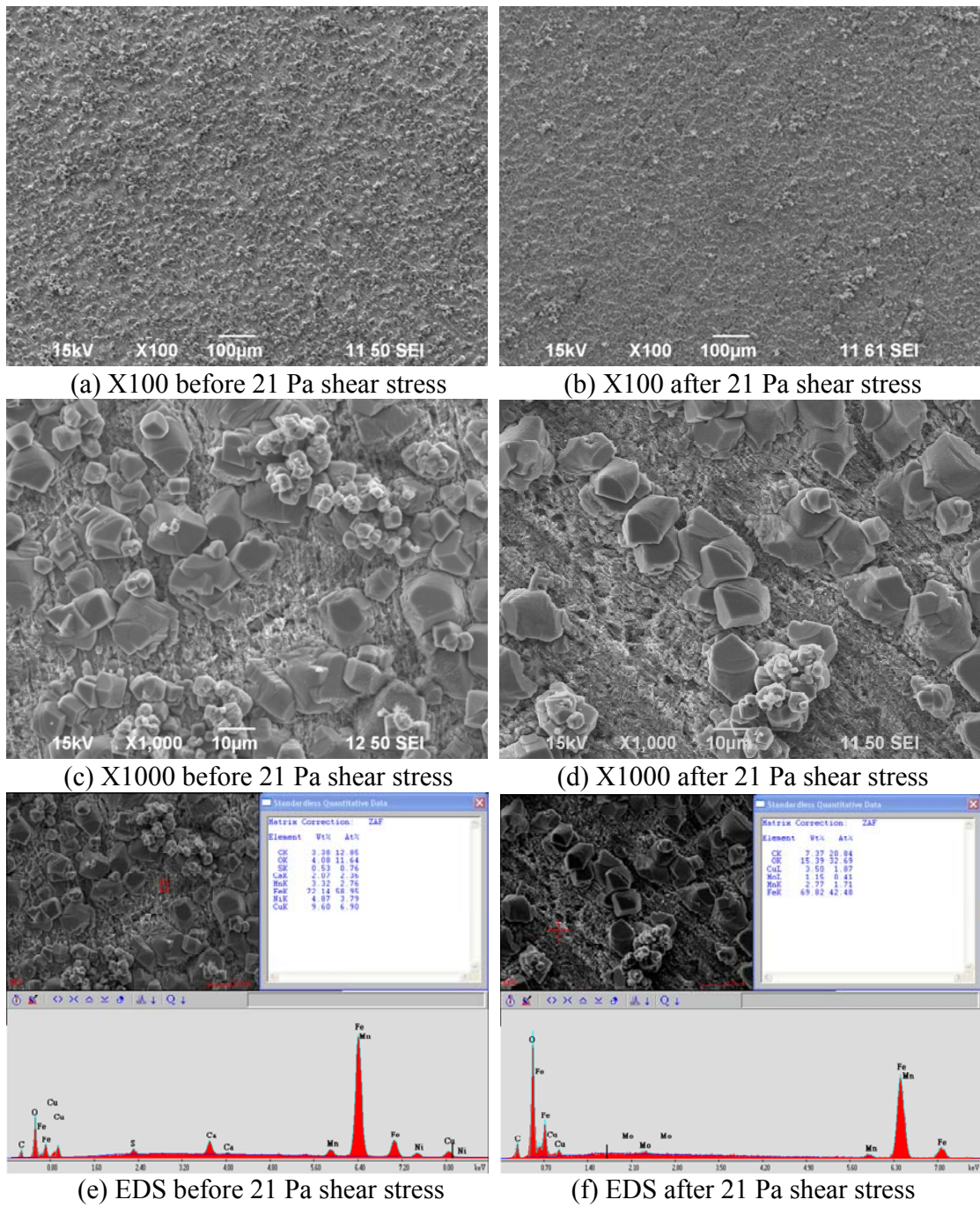


Figure 25. SEM images of specimen surface before and after layer removal at 21 Pa, pH 6.6, 1 wt% NaCl, 80°C.

## **4.5 Mechanical properties of the protective iron carbonate layer**

### *4.5.1 Experimental method*

#### 4.5.1.1 Test setup

For these tests, the iron carbonate layer formation was done within a glass cell setup shown in Figure 26, which is very similar to the glass cell setup shown previously, with the cylindrical working electrode replaced by a flat square specimen. Detailed information of cell setup can be referred to the earlier description of the glass cell setup made in this chapter.

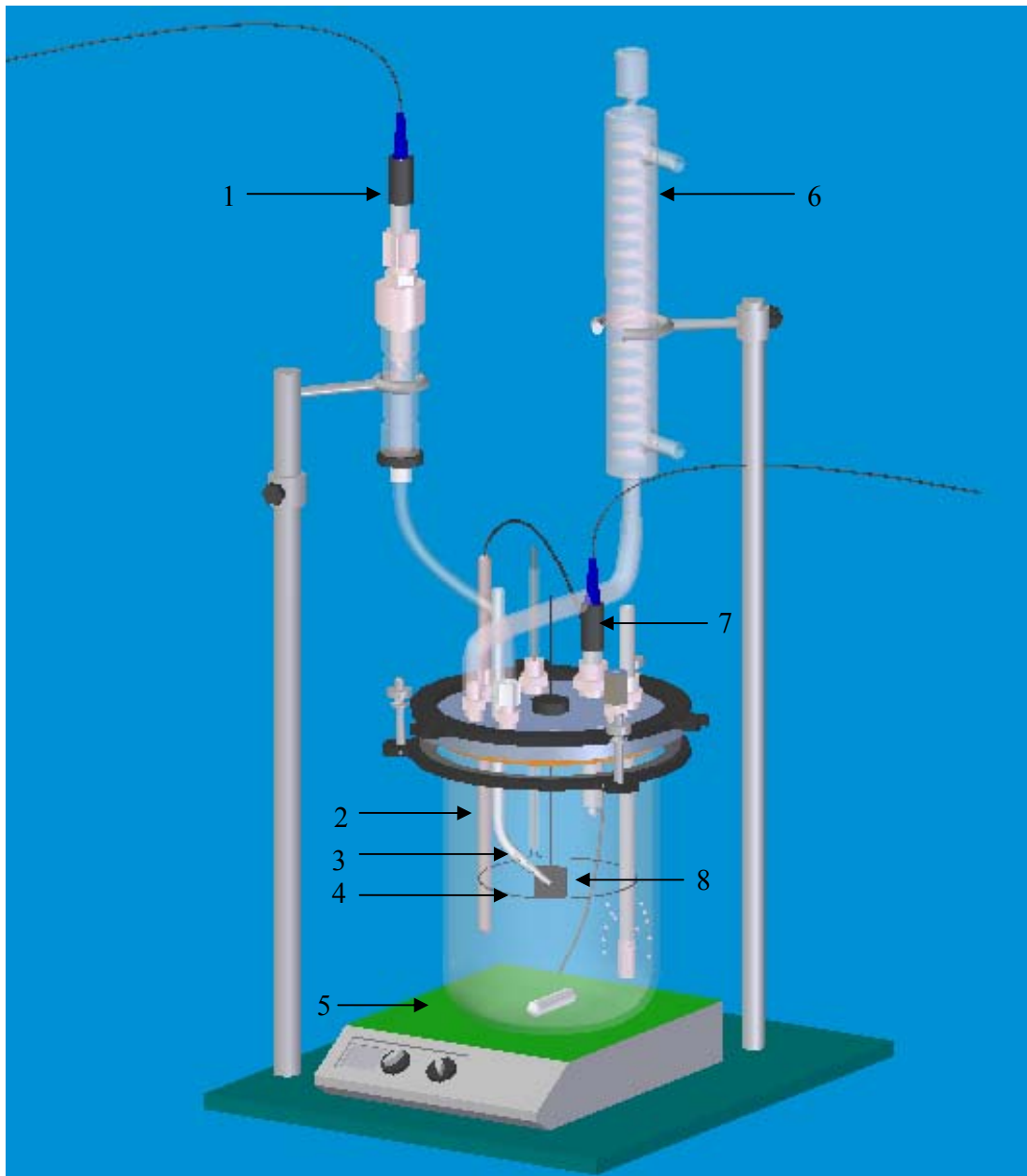


Figure 26. Schematic of glass cell set-up for layer formation for mechanical property test of iron carbonate.

1-reference electrode; 2- thermo probe; 3-Luggin capillary; 4-counter electrode; 5-heater; 6-condenser; 7-pH probe; 8-working electrode (square specimen).

A tensile machine (Instron 4500) used for the iron carbonate mechanical strength measurement is shown in Figure 27. The square steel specimen covered with protective

iron carbonate layer was mounted into the sample holder and fixed onto the moving stage tightly, with the “stud” (glued to the specimen in advance) attached to the top of the tensile machine. The stage was moved at a constant speed. The stud and the steel sample were separated and the force was measured during the process.

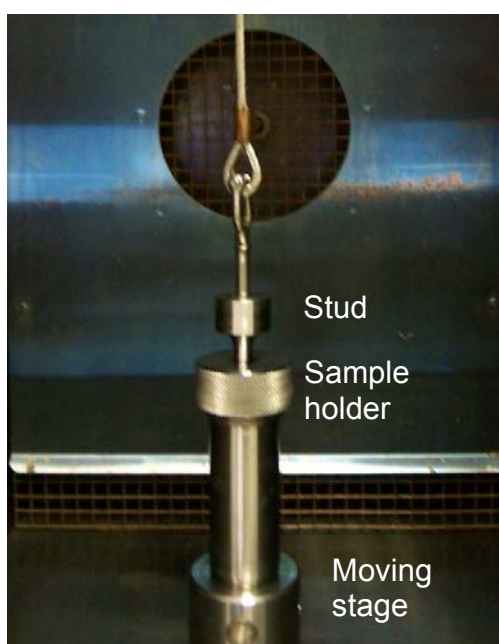


Figure 27. Mechanical strength test set-up with tensile machine.

#### 4.5.1.2 Test matrix

The test matrix for iron carbonate formation is shown in Table 8. Chemical composition of carbon steel X52 is shown in Table 9.

Table 8. Test matrix for layer formation test.

Material	X52
Test solution	1 wt% NaCl
Temperature	80°C
CO <sub>2</sub> partial pressure	0.52 bar
Solution pH	6.6
Initial [Fe <sup>2+</sup> ]	50 ppm
Initial supersaturation	300
Galvanostatic current	0.86 A/m <sup>2</sup>
Test duration	24 hours

Table 9. Chemical composition of X52 and X65 steel (wt%).

C	Si	Mn	P	S	Cr	Ni	Cu	Nb	Al	Fe
0.094	0.22	0.97	0.012	0.005	0.028	0.03	0.02	0.03	0.04	Balance

#### 4.5.1.3 Test procedure

For iron carbonate layer formation, 1 wt% NaCl solution was prepared, deoxygenated with CO<sub>2</sub> and heated to 80°C. The solution pH was adjusted to the desired value by adding 1 M NaHCO<sub>3</sub> into the test solution. Test specimen was polished with different grit of sand papers, rinsed and dried. After the specimen was immersed into the test solution, corrosion potential and corrosion rate was measured. A galvanostatic current, which was equal to 1 mm/year corrosion rate, was applied to the specimen during

layer formation process in order to build a protective iron carbonate layer repeatedly and quickly. Additional  $\text{Fe}^{2+}$  was added to the solution to achieve a high supersaturation condition. After 24 hours, galvanostatic current was stopped and the corrosion rate was measured again. The test specimen was taken out of the solution and prepared for SEM surface analysis and mechanical property test.

For the mechanical property test, glue was deposited onto a stainless steel specimen (to measure glue strength) or iron carbonate covered steel specimen (to measure iron carbonate layer adhesion strength) and the stud was laid on top of the specimen. The specimens with the stud was set under specific conditions for a specific amount of time (according to the different type of glue that was used) to allow the glue to be fully cured. Then the specimen together with the stud was mounted onto Instron 4500 tensile machine to measure the force that was needed to separate the stud and specimen. After the test, both stud and specimen were analyzed with SEM and EDS. A layer of aluminum foil was used to wrap the specimen before being sealed in epoxy in order to distinguish the glue used for tensile test and the epoxy used for sealing the specimen.

#### *4.5.2 Results and discussion*

##### *4.5.2.1 Iron carbonate layer formation*

Figure 28 shows a typical potential change curve during the iron carbonate layer formation process which involves applying an anodic galvanostatic current to the working electrode. In the beginning of the test, the free corrosion rate of the sample was measured by LPR to be approximately 1 mm/year. As the anodic galvanostatic current was applied to the working electrode, a steady amount of  $\text{Fe}^{2+}$  was released by the steel

sample into the aqueous solution close to the surface, which added to the  $\text{Fe}^{2+}$  that were injected at the beginning of the test into the bulk solution, making the solution highly supersaturated with respect to iron carbonate. As a consequence, a layer of iron carbonate was formed rapidly on the steel surface. This layer became denser and more protective with time. The corrosion potential increased about 300 mV, which indicates that a passive layer had developed together with the iron carbonate layer on the surface. At the end of the test, after 24 hours of iron carbonate layer “building”, the measured free corrosion rate of the sample had decreased to less than 0.1 mm/year. SEM images of the top view of the iron carbonate layer surface and a cross section of the sample after iron carbonate layer formation is given in Figure 29, which shows an evenly covered steel substrate with an iron carbonate layer around 10  $\mu\text{m}$  in thickness.

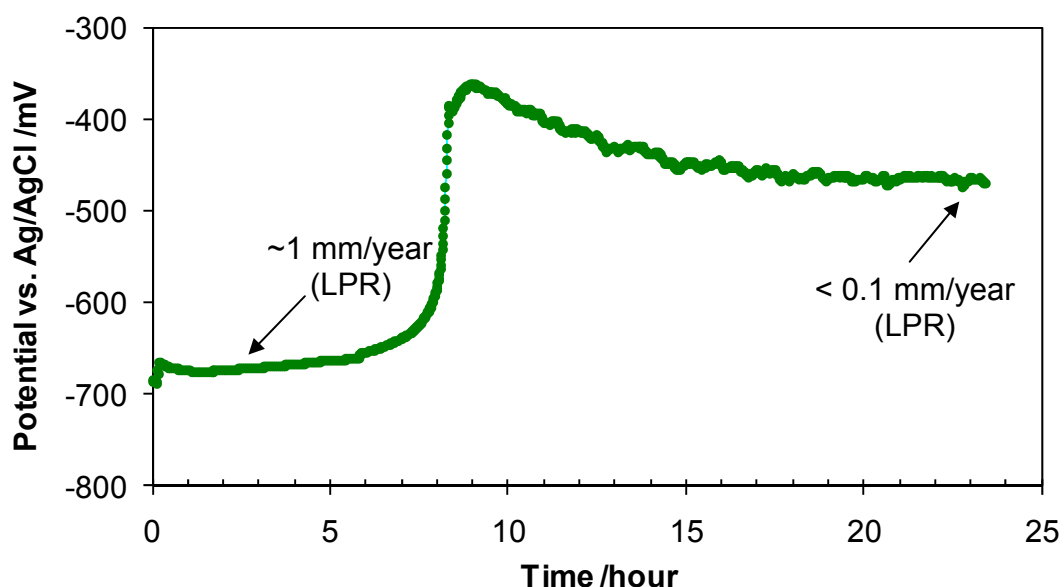


Figure 28. Change of corrosion potential during iron carbonate layer formation process, 1 wt% NaCl, 80°C, pH 6.6, initial SS of  $\text{FeCO}_3=300$ , applied anodic current= $0.86 \text{ A/m}^2$ .

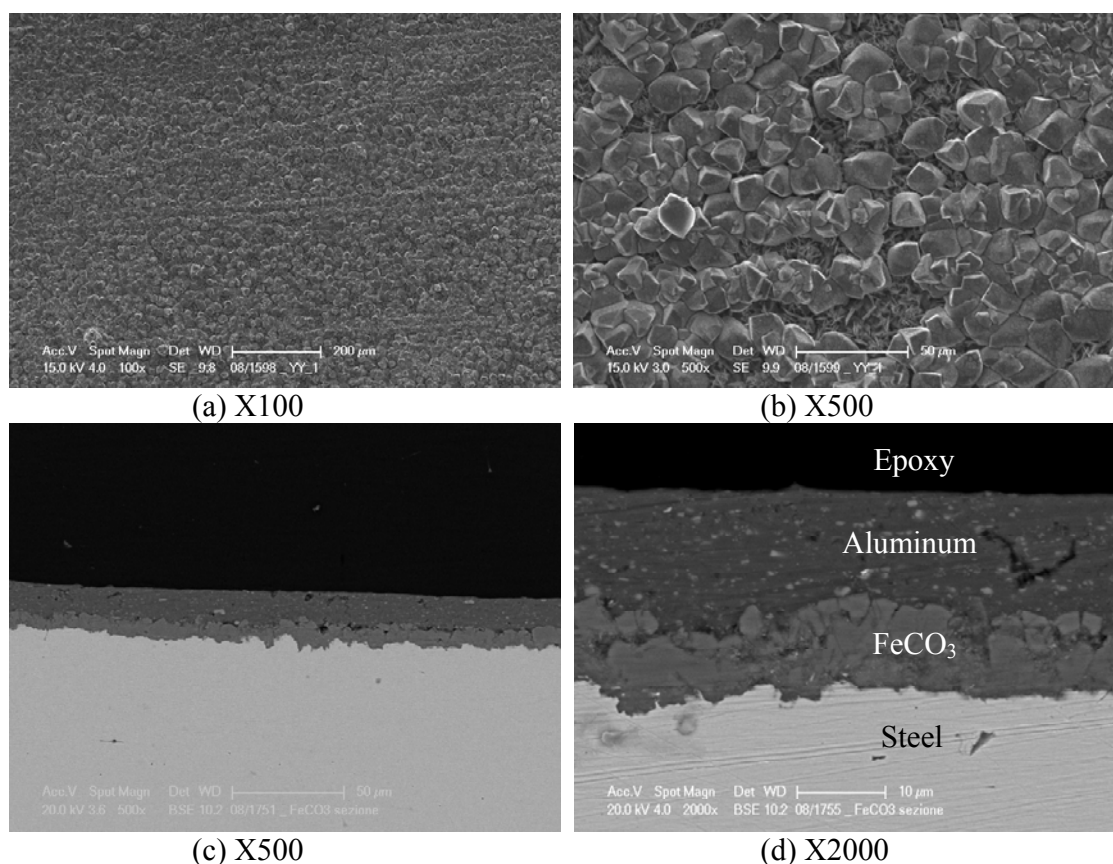


Figure 29. SEM images of surface (a, b) and cross sections (c, d) of the iron carbonate layer.

#### 4.5.2.2 Mechanical property test of iron carbonate layer

Before conducting the iron carbonate mechanical strength tests on carbon steel samples covered with an iron carbonate layer, the “adhesive-strength” tests were done by gluing two stainless steel studs together and pulling them apart, thereby measuring the strength of the adhesive. The results showed that the adhesive “F” had an especially high strength, about 53 MPa, while other adhesives had a lower strength, typically around 10 MPa. Figure 30 shows the images of the surfaces after the adhesive-strength test using adhesive “F”. It can be observed that the adhesive is present on both stud surfaces suggesting that the “breakage” occurred across the bulk of the adhesive rather than at the

contact with the steel substrate, which means that the adhesion strength between the adhesive and the steel substrate was even higher than the measured value.

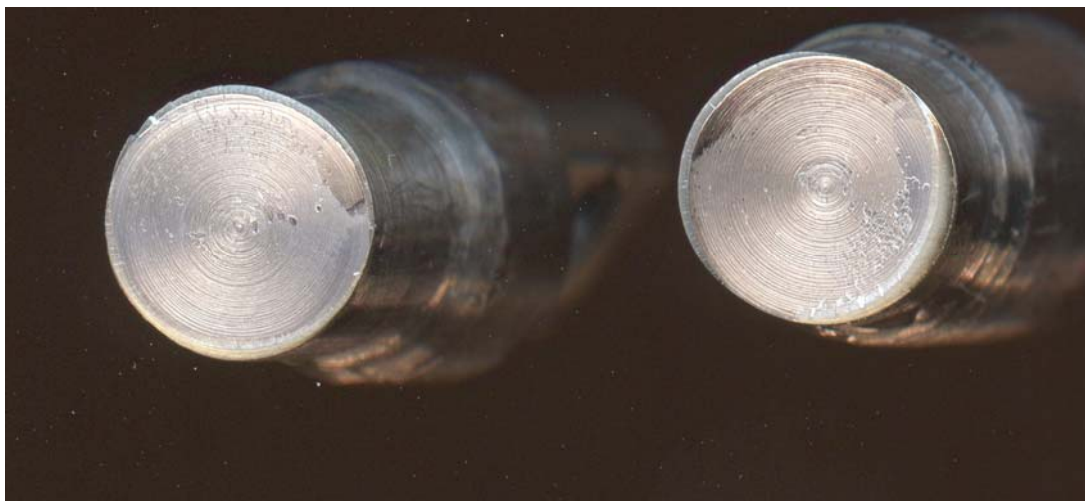


Figure 30. Surfaces of stainless steel stud after adhesive strength test of adhesive F.

In order to demonstrate the “grip” of the adhesive on the iron carbonate layer, Figure 31 shows a cross section image of a steel sample with an iron carbonate layer and a cured adhesive on top of it, before the iron carbonate mechanical strength test was conducted. It can be seen that the dense iron carbonate layer surface was fully covered by the adhesive and in some places the adhesive penetrated deeper into the layer.

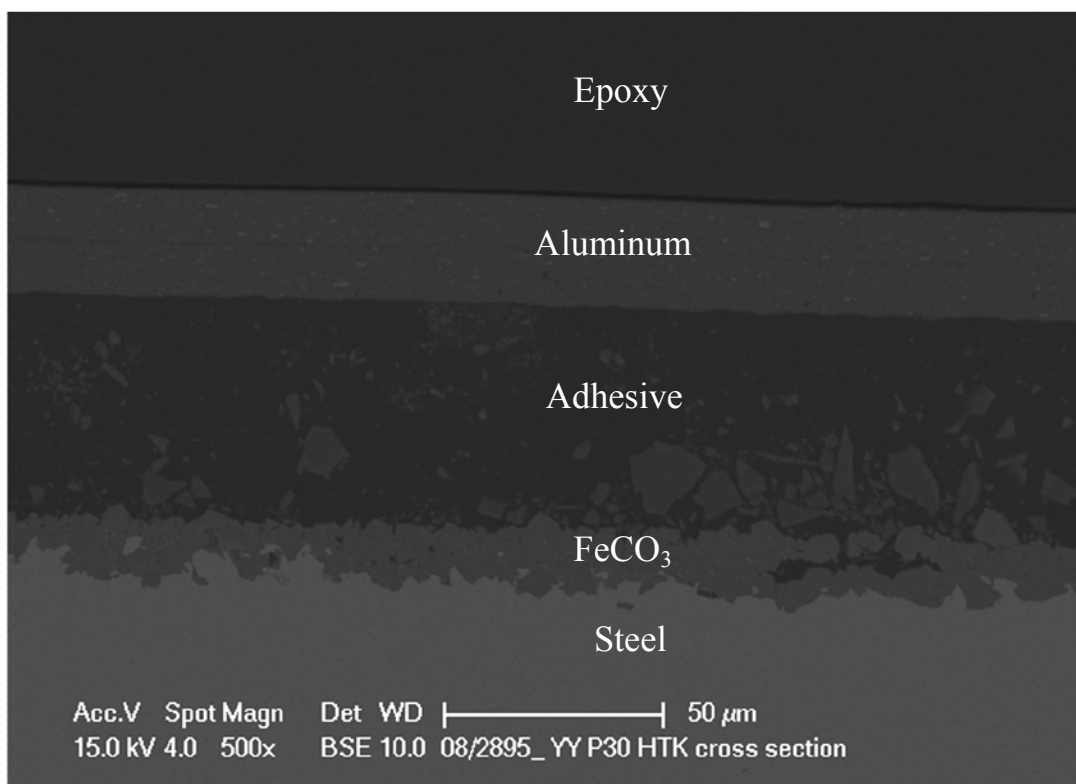


Figure 31. Cross section of iron carbonate layer with adhesive before mechanical strength test.

Figure 32 shows the results of mechanical strength tests in which less than 10% of the iron carbonate failed. On most of the surface, the adhesive detached from the iron carbonate layer, suggesting that the actual iron carbonate strength must be larger than the measured values. With different adhesives, the values of iron carbonate mechanical strength fluctuated, but they are all of the same order of magnitude. When compared with the measured strength of the adhesive itself, some of the results for iron carbonate mechanical strength fall rather close, which appears to bring the validity of the results into question, however any doubt is removed when considering the tests done with adhesive “F” which gave a much lower value for the iron carbonate mechanical strength

compared to the strength of the adhesive itself. Therefore only the results obtained with this adhesive will be shown in the graphs below.

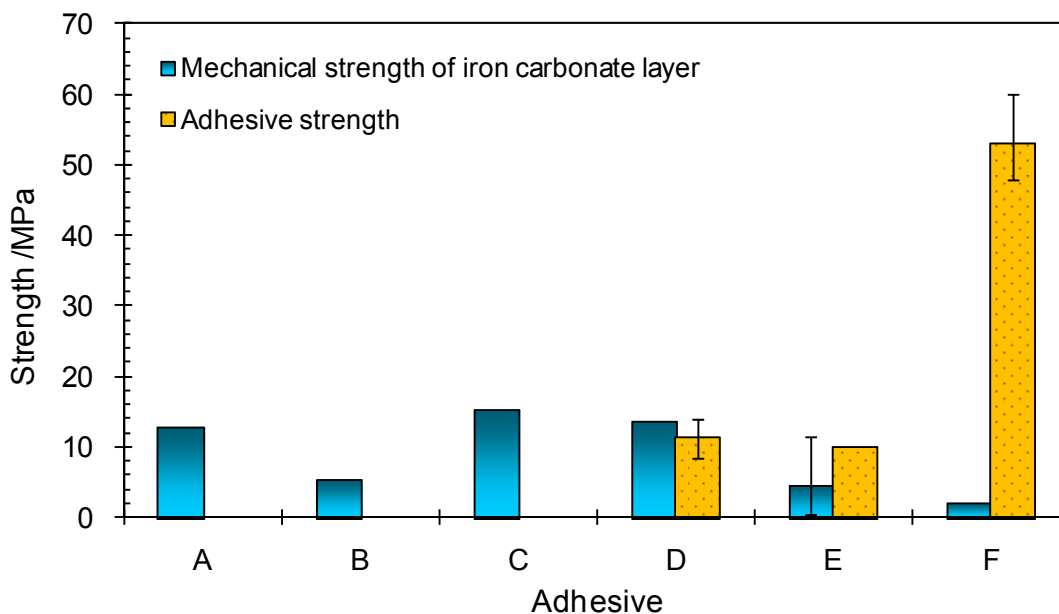


Figure 32. Mechanical strength of iron carbonate layer on a carbon steel substrate for the case in which less than 10% of the iron carbonate failed.

Figure 33 shows the SEM images of the steel specimen surface after the iron carbonate mechanical strength test and Figure 34 shows the corresponding stud surface. Over most of the surface area, the iron carbonate layer was not damaged whereas the adhesive has detached from the iron carbonate layer surface. It can be noticed in Figure 33 that there were some small areas where the steel underneath the iron carbonate layer was exposed, which corresponds to the grey sections in Figure 34 indicating a completely detached iron carbonate layer.

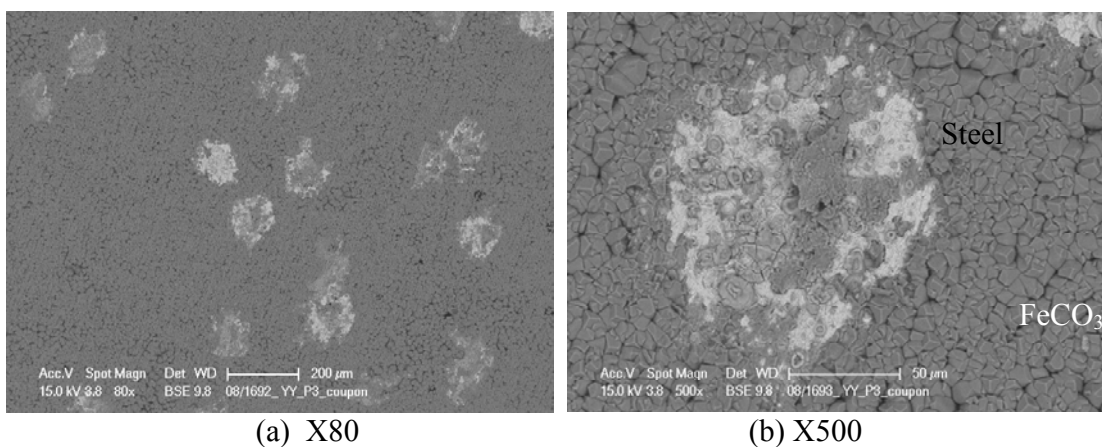


Figure 33. SEM images of the sample surface after the test in which less than 10% of the iron carbonate failed (light grey areas).

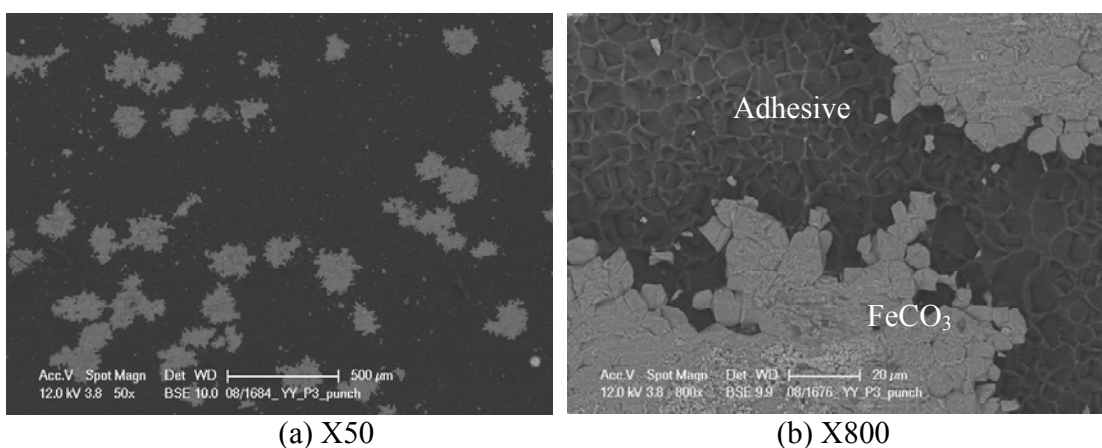


Figure 34. SEM images of the stud surface after the test in which less than 10% of the iron carbonate failed (light grey areas).

Figure 35 shows the results where almost 40% of the total area was showing iron carbonate layer failure. Compared to the results discussed immediately above, the measured iron carbonate mechanical strength was somewhat higher but still much lower than the strength of adhesive “F”. It can be seen in Figure 36 and Figure 37 that in some areas the iron carbonate layer was detached from the steel surface, while in other areas the adhesive detached from the layer.

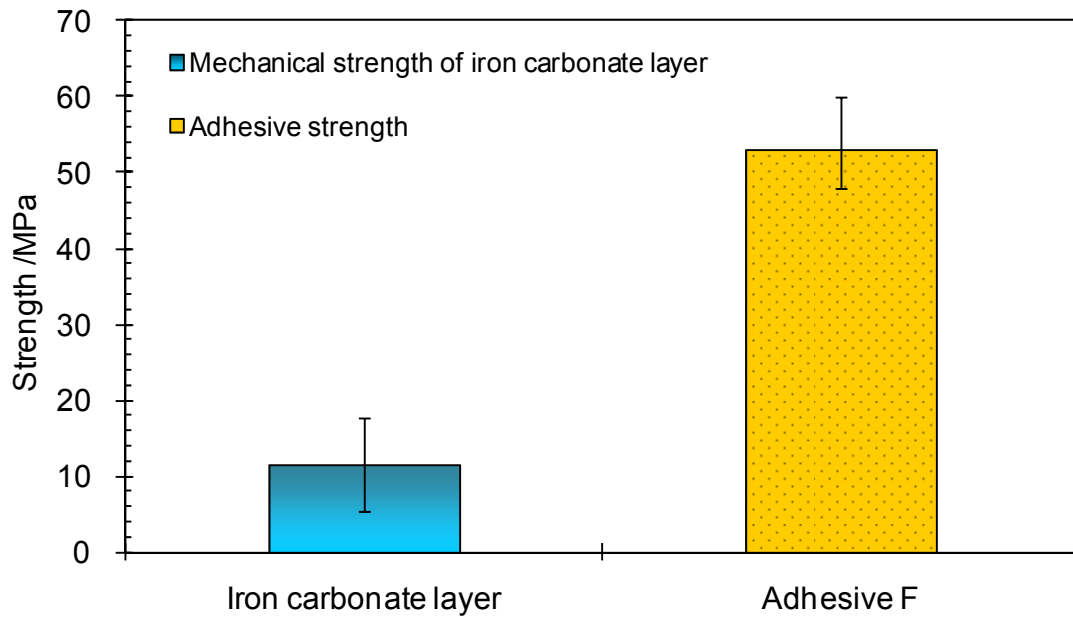


Figure 35. Mechanical strength of iron carbonate layer on a carbon steel substrate for the case in which 10% - 50% of the iron carbonate surface failed.

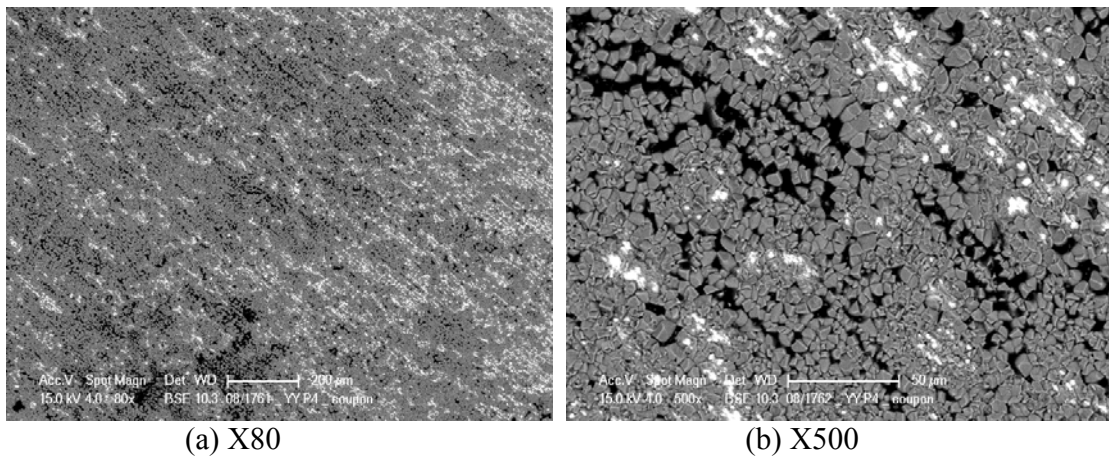


Figure 36. SEM images of the sample surface after the test in which 10% - 50% of the iron carbonate failed (light grey areas).

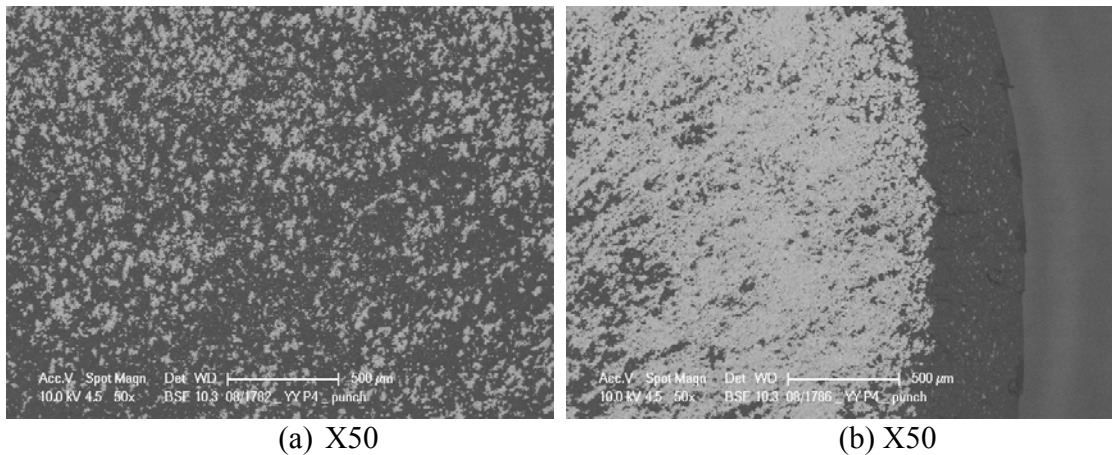


Figure 37. SEM images of the stud surface after the test in which 10% - 50% of the iron carbonate failed (light grey areas). Images (a) and (b) are from different locations on the stud surface.

The results where more than 50% of the total area was showing iron carbonate layer failure are shown in Figure 38, which agreed very well with the previous observations. As can be seen in Figure 39 and Figure 40, most of the surface of the sample and the stud were covered with iron carbonate layer. This means that the failure happened predominantly within the iron carbonate layer rather than between the layer and steel substrate or the layer and the adhesive. In addition, the cross section shown in Figure 41 indicates that the adhesive did not contact the steel substrate and has not interfered with the iron carbonate mechanical strength measurement.

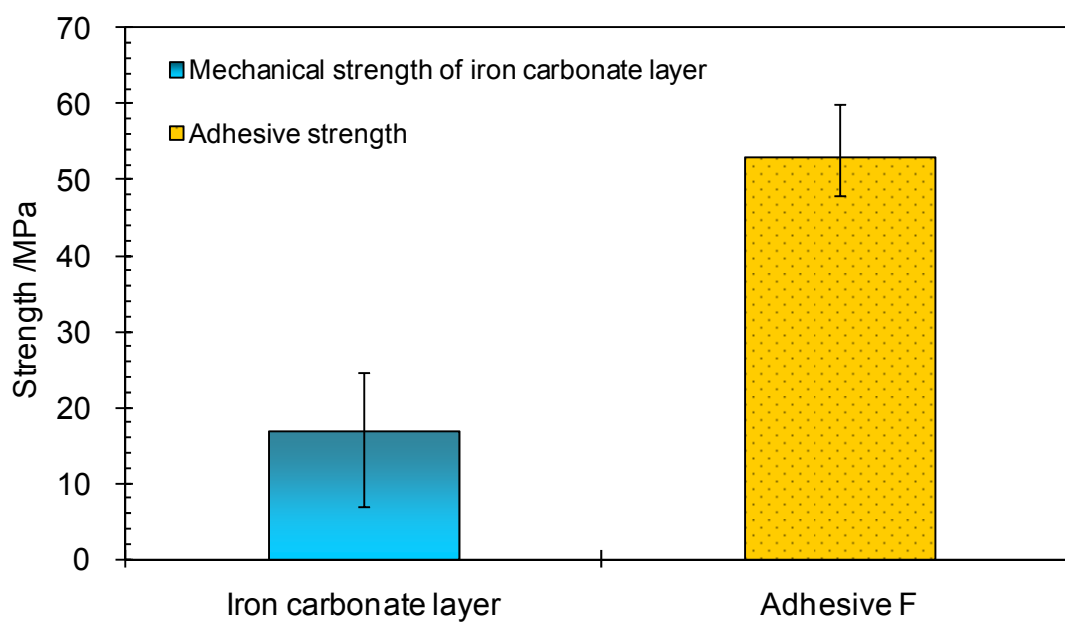


Figure 38. Mechanical strength of iron carbonate layer on a carbon steel substrate for the case in which more than 50% of the iron carbonate surface failed.

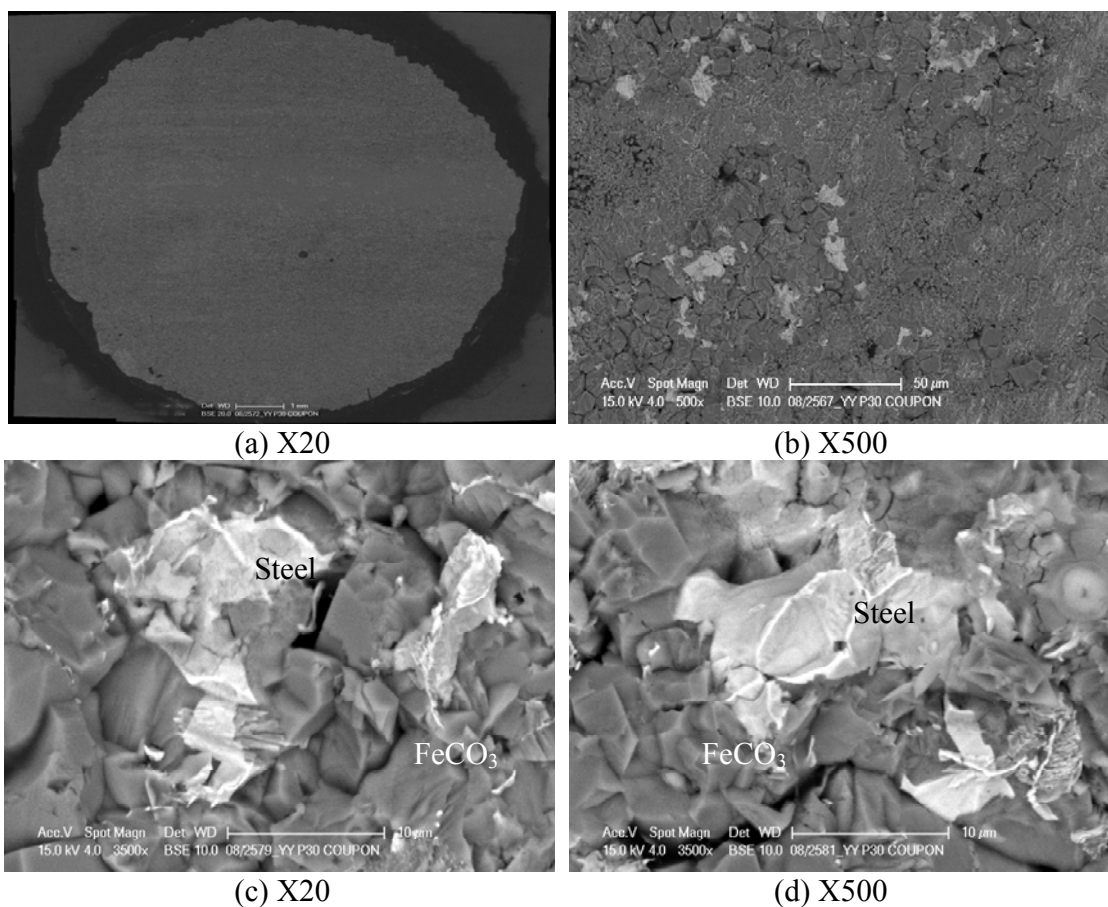


Figure 39. SEM images of the sample surface after the test in which more than 50% of the iron carbonate failed (darker gray areas), showing small portions where the iron carbonate detached from the steel (lighter gray areas).

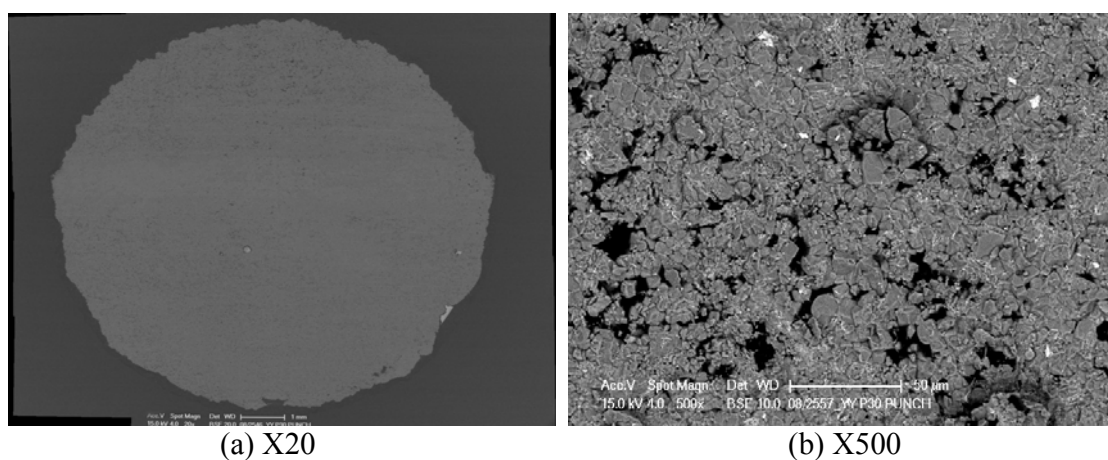


Figure 40. SEM images of the stud surface after the test in which more than 50% of the iron carbonate failed, showing iron carbonate detached from the sample.

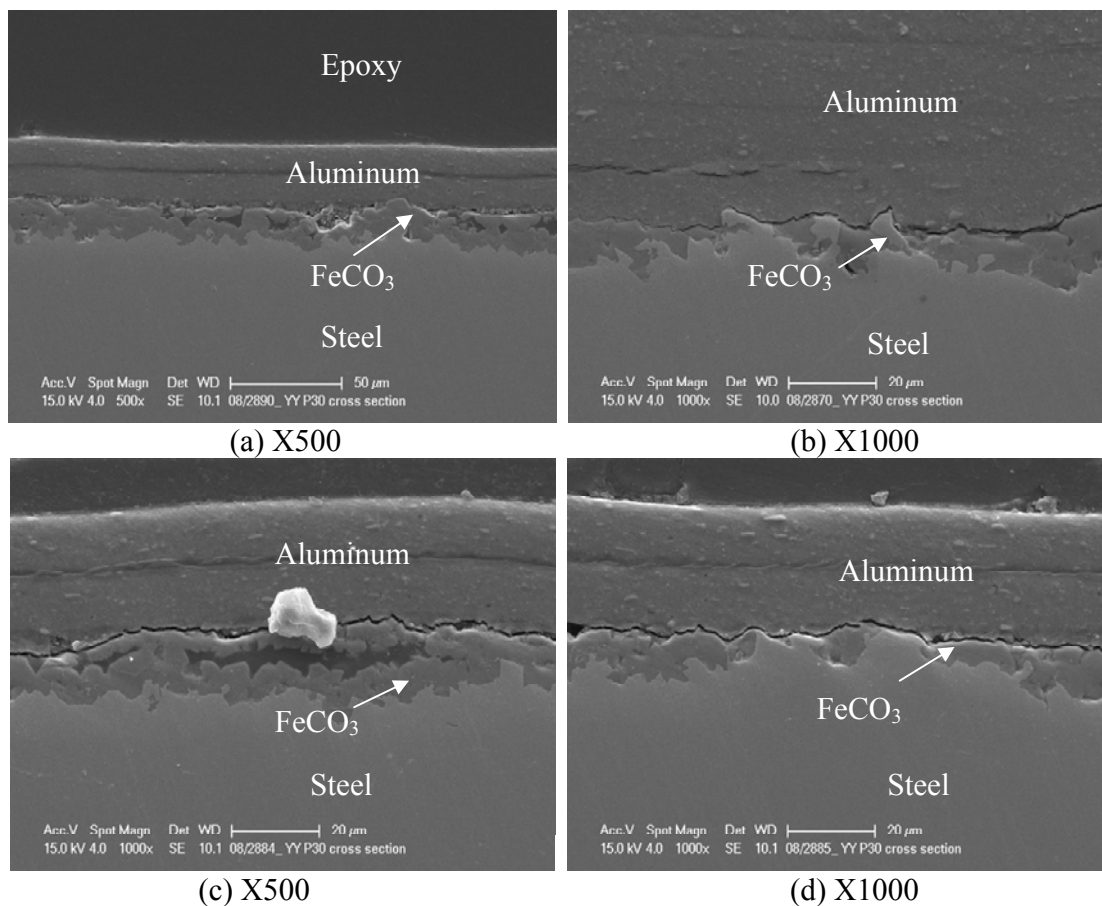


Figure 41. Cross section SEM images of the sample after the test in which more than 50% of the iron carbonate failed, taken at a location where iron carbonate “broke”.

It can be concluded that the mechanical strength reported above represents a “mixed” value, which predominantly reflecting the mechanical strength of the iron carbonate layer however there are contributions from the adhesion strength between iron carbonate layer and carbon steel substrate, and between the adhesive and the iron carbonate layer. It was hard to distinguish how much this contribution really was, but from the analysis presented above it can be concluded that the mechanical strength of the

iron carbonate layer must have been in the excess of 10 MPa. The adhesion strength between the iron carbonate layer and the steel substrate appears to be even higher.

When comparing the adhesion strength of protective iron carbonate layer obtained in the current study with literature, although limited (K. Gao, et al., 2008; Schmitt, et al., 1999), the values of the adhesion strength all are of same order of magnitude, which further validated the current results.

#### **4.6 Discussion**

Besides the experimental results shown above, there were some additional tests conducted in a glass cell with a rotating cylinder setup and electrochemical quartz crystal microbalance with jet impingement setup (details about these test setups can be found in Chapter 5). Because it was discovered later that there were some problems in the experimental methods used in these tests, the results do not truly reflect the situation which was investigated. To avoid confusion, and still show what was done and why the results are not valid, these tests are shown in Appendix A and Appendix B respectively, where the results were analyzed in detail.

Another point that needs to be addressed is that during iron carbonate layer formation, one phenomenon was noticed, which was not considered before. Accompanying the corrosion rate decrease due to protective iron carbonate layer formation on the steel surface, an increase of corrosion potential was observed simultaneously (Han, et al., 2011) (see Figure 5, Figure 8, Figure 13, Figure 17 and Figure 24). It was indicated that spontaneous passivation of carbon steel could take place in CO<sub>2</sub> corrosion environment, which significantly slowed down the corrosion rate and

caused the increase of corrosion potential. It was pointed out that the passivation behavior was mainly caused by the formation of iron carbonate with trace amount of magnetite (Han, et al., 2011). However, in a follow-up study (Li, 2011), no magnetite was detected under the same conditions and the passivation behavior was still observed, just like in the present study. It was concluded that the passivation behavior is seen when very adherent and protective layers (sometimes very thin) form and almost fully cover the steel surface, thereby retarding the anodic reaction significantly. Future work needs to be done to get a better understanding of the spontaneous passivation behavior of carbon steel in CO<sub>2</sub> corrosion environment, as it plays an important role in the protectiveness of corrosion product layer.

#### **4.7 Summary**

In this chapter, the mechanical flow effect on the protective iron carbonate layer formed on carbon steel surface was investigated in different experimental configurations. In all the experiments, a layer of iron carbonate was formed and the corrosion rate was decreased to around 0.1 mm/year, which indicates that the iron carbonate layer was very protective. Various flow conditions were generated to observe the response of the protective iron carbonate layer to highly turbulent flow. In all the tests, no significant change was observed in the corrosion rate. In some tests, the large grains of iron carbonate (including prism shaped and plate shaped) were removed by turbulent flow, while the steel surface still remained at a very low corrosion rate as there was still a very thin yet adherent layer attached to the steel surface and protected the underlining metal from corrosion.

In addition, the mechanical strength of the protective iron carbonate layer was directly evaluated by tensile tests. It was shown that the adhesion strength between the protective iron carbonate layer and the steel substrate is of the order of  $10^6$  Pa, which is several orders of magnitudes higher than the shear stress that realistic flow can provide. Therefore, in typical oil and gas pipelines, the protective iron carbonate layer could not be mechanically damaged by flow only.

## CHAPTER 5: CHEMICAL DISSOLUTION OF PROTECTIVE IRON CARBONATE LAYER<sup>3</sup>

### 5.1 Introduction

In the previous chapter, the mechanical effect of flow on the protective iron carbonate layer was investigated. As introduced in Chapter 2, there also exists another possible scenario where the protective iron carbonate layer could be damaged. When the saturation level of the solution is below 1, which means the solution is undersaturated with respect to iron carbonate, dissolution could happen and the protective layer consequently will be damaged. In this chapter, the effect of chemical dissolution on the protective iron carbonate layer will be investigated both qualitatively and quantitatively. In addition, a dissolution mechanism for the iron carbonate layer will be proposed.

### 5.2 Qualitative study of iron carbonate dissolution using SEM

#### *5.2.1 Experimental method*

##### 5.2.1.1 Test setup

Circular specimens with a 3.2 cm diameter were used to form an iron carbonate layer in a glass cell setup, which is very similar to the one shown in Figure 26. A 100 ml beaker filled with test solution (pH 2.0 or pH 3.8) was used to dissolve the iron carbonate layer formed on the carbon steel specimen. SEM was used to observe the change of the appearance of the iron carbonate layer periodically and EDS was used when needed.

---

<sup>3</sup> Portions of the work presented in this Chapter was published in the co-authored paper (Yang, et al., 2008).

### 5.2.1.2 Test matrix

The test matrix for the qualitative study of iron carbonate dissolution using SEM is shown in Table 10.

Table 10. Text matrix for qualitative study of iron carbonate layer dissolution using SEM.

Parameters	Layer formation	Layer dissolution
Material	X65 carbon steel	
Solution	1 wt% NaCl	
Temperature	80°C	25°C
CO <sub>2</sub> partial Pressure	0.52 bar	0.96 bar
Solution pH	6.6	2.0, 3.8
Initial [Fe <sup>2+</sup> ]	50 ppm	0
Initial saturation level	300	0

### 5.2.1.3 Test procedure

The iron carbonate layer formation was conducted in a 2 liter glass cell with 1 wt% NaCl. The detailed procedure for layer formation can be found in section 4.2.1.3. Subsequently, a 1 wt% NaCl test solution was used for the iron carbonate layer dissolution which was prepared and deoxygenated with CO<sub>2</sub> in advance. The pH of the solution was adjusted by using hydrochloric acid (HCl) to the desired pH value when necessary. Once the iron carbonate layer formation was finished, the specimen was taken from the glass cell and rinsed with isopropyl alcohol and dried. Images of the specimen

surface were taken using SEM before proceeding to dissolution. When using the test solution with pH 2.0 to dissolve iron carbonate layer, droplets of the prepared test solution were added onto the specimen surface sequentially. When using the test solution with pH 3.8 to dissolve the iron carbonate layer, the specimen was immersed into the prepared test solution. During the dissolution process, the specimen was taken to SEM periodically for observation of the change of the iron carbonate layer.

### *5.2.2 Results and discussion*

#### *5.2.2.1 Iron carbonate layer formation*

A protective iron carbonate layer was formed on X65 steel specimens using the same procedure described in section 4.2.1.3, for the purpose of dissolution observation using SEM and EDS. In order to compare the change of the surface due to dissolution, images of the specimen surface were taken after the iron carbonate layer was formed on the steel surface as shown in Figure 42. There was an evenly covered iron carbonate layer protecting the steel surface from corrosion, including both prism-shaped and plate-shaped iron carbonate.

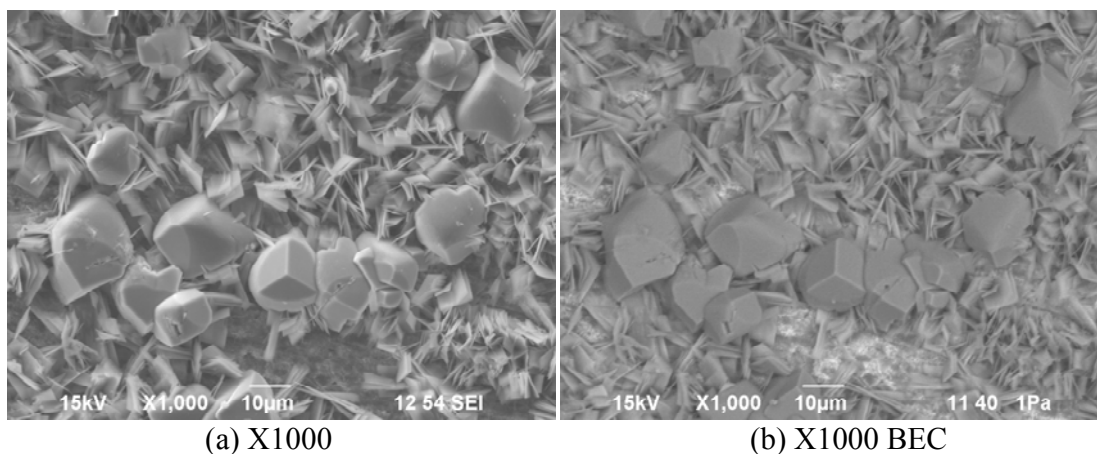


Figure 42. SEM images of the specimen surface after layer formation at pH 6.6, 1 wt% NaCl, at 80°C, initial SS=300.

#### 5.2.2.2 Iron carbonate dissolution with pH 2.0 test solution

Figure 43 shows the images of the iron carbonate covered steel surface after adding one droplet of pH 2.0 test solution to dissolve the layer. A lot of plate shaped iron carbonate vanished, which can be seen when comparing Figure 43 with Figure 42.

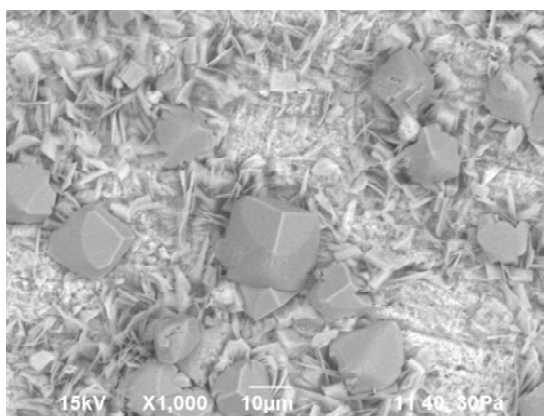


Figure 43. SEM image (X1000 BEC) of the specimen surface after iron carbonate dissolution by the first droplet of pH 2.0 test solution.

Continuing the test by adding another droplet of pH 2.0 test solution onto the specimen surface, SEM images were taken again and are shown in Figure 44. As can be

seen there, almost all of the plate shaped iron carbonate disappeared due to dissolution, but quite a few prism shaped iron carbonate crystals were still remaining on the specimen surface.

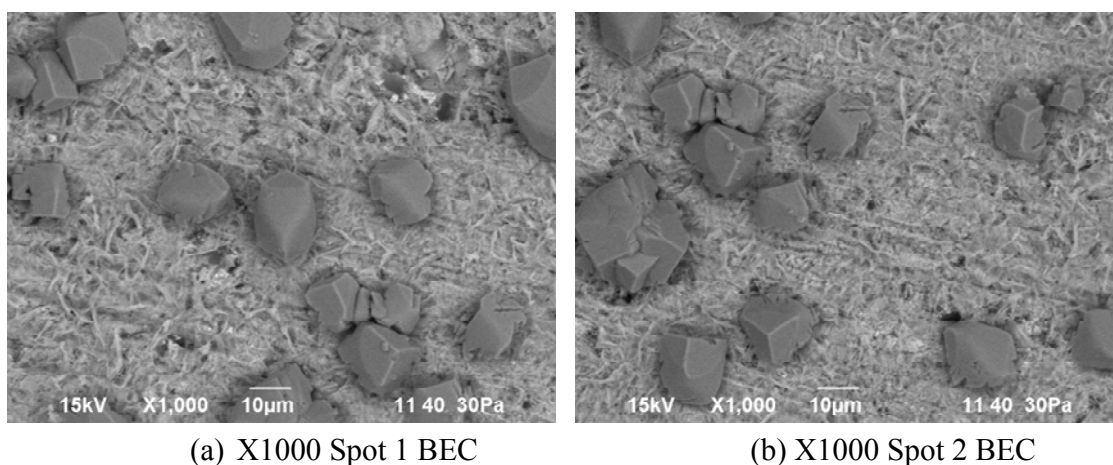


Figure 44. SEM images of the specimen surface after iron carbonate dissolution by the second droplet of test solution with pH 2.0.

After another droplet of pH 2.0 test solution was added onto the specimen surface, it can be seen in Figure 45 that just a few prism shaped iron carbonate crystals were left. Interestingly, the sharp edges of the crystals still remained after dissolution of all of the surrounding iron carbonate. It appears that the prism shaped iron carbonate was more resistant to dissolution. The pH of the test solution was 2.0 so the solution was extremely undersaturated with regard to  $\text{FeCO}_3$ . The solution appeared to be quite aggressive and the dissolution process occurred very fast by adding just droplets of the test solution onto the specimen surface.

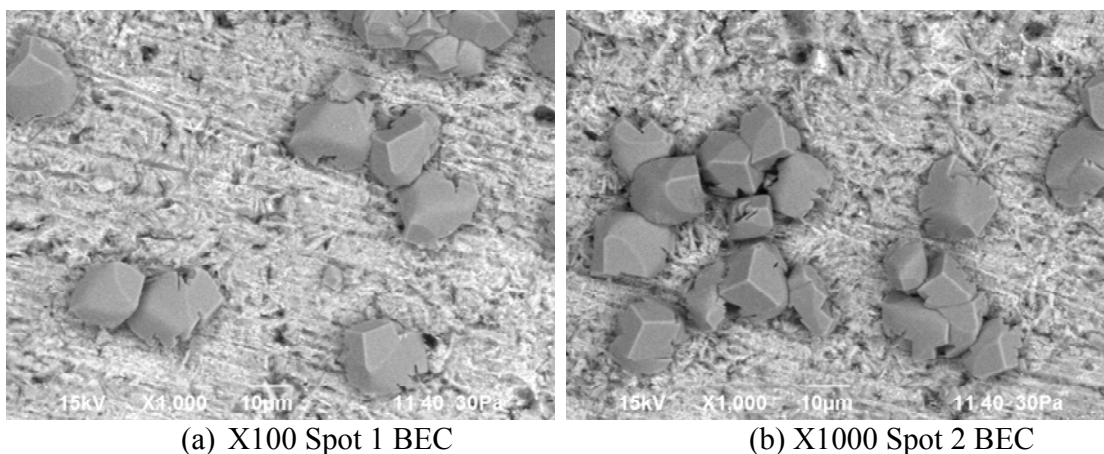


Figure 45. SEM images of the specimen surface after iron carbonate dissolution by the third droplet of test solution with pH 2.0.

#### 5.2.2.3 Iron carbonate dissolution with a pH 3.8 test solution

Another set of dissolution observations made by SEM were done by using a less aggressive test solution with pH 3.8. This was the pH at equilibrium when the test solution was purged with CO<sub>2</sub> at room temperature, so no HCl was needed to adjust the solution pH. Since the pH of the test solution was higher and it was expected that the dissolution process would be slower, in this test the specimen was completely immersed into the beaker with 100ml test solution purged with CO<sub>2</sub> continuously at ambient condition.

The specimen surface after iron carbonate layer formation was observed by SEM and EDS as shown in Figure 46. As before, a similar iron carbonate layer was obtained under the same condition (pH 6.6, 80°C, and SS (FeCO<sub>3</sub>) $\gg$ 1).

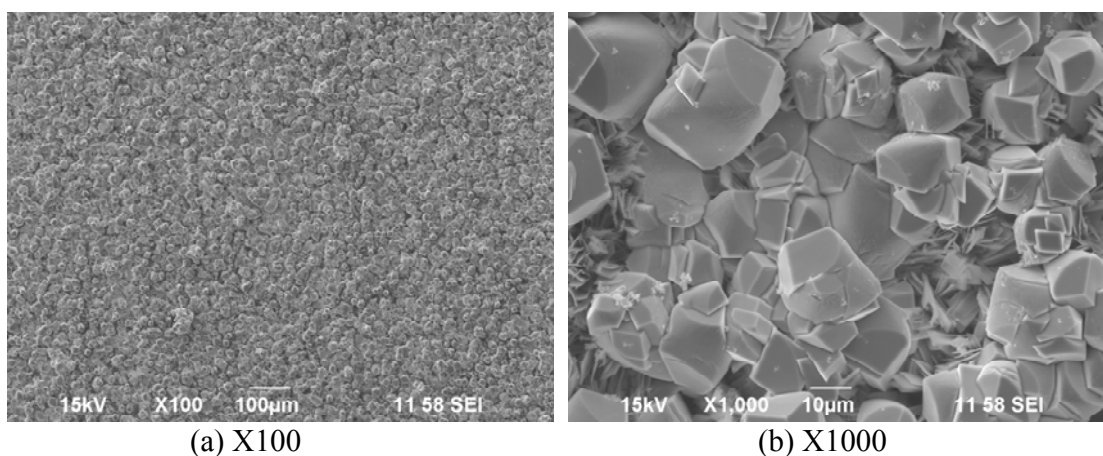


Figure 46. SEM and EDS images of the specimen surface after iron carbonate layer formation at pH 6.6, 1 wt% NaCl and 80°C.

SEM images (Figure 47) were taken after immersing the specimen into the pH 3.8 test solution for 5 minutes for dissolution. Since the pH of the test solution was higher and the solution was less aggressive, there was no significant change observed on the specimen surface after five minutes compared with Figure 46.

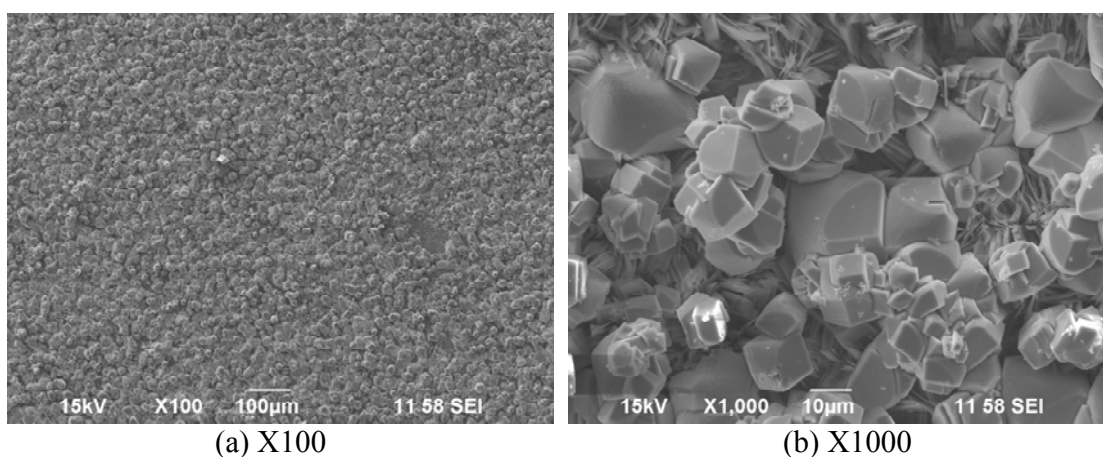
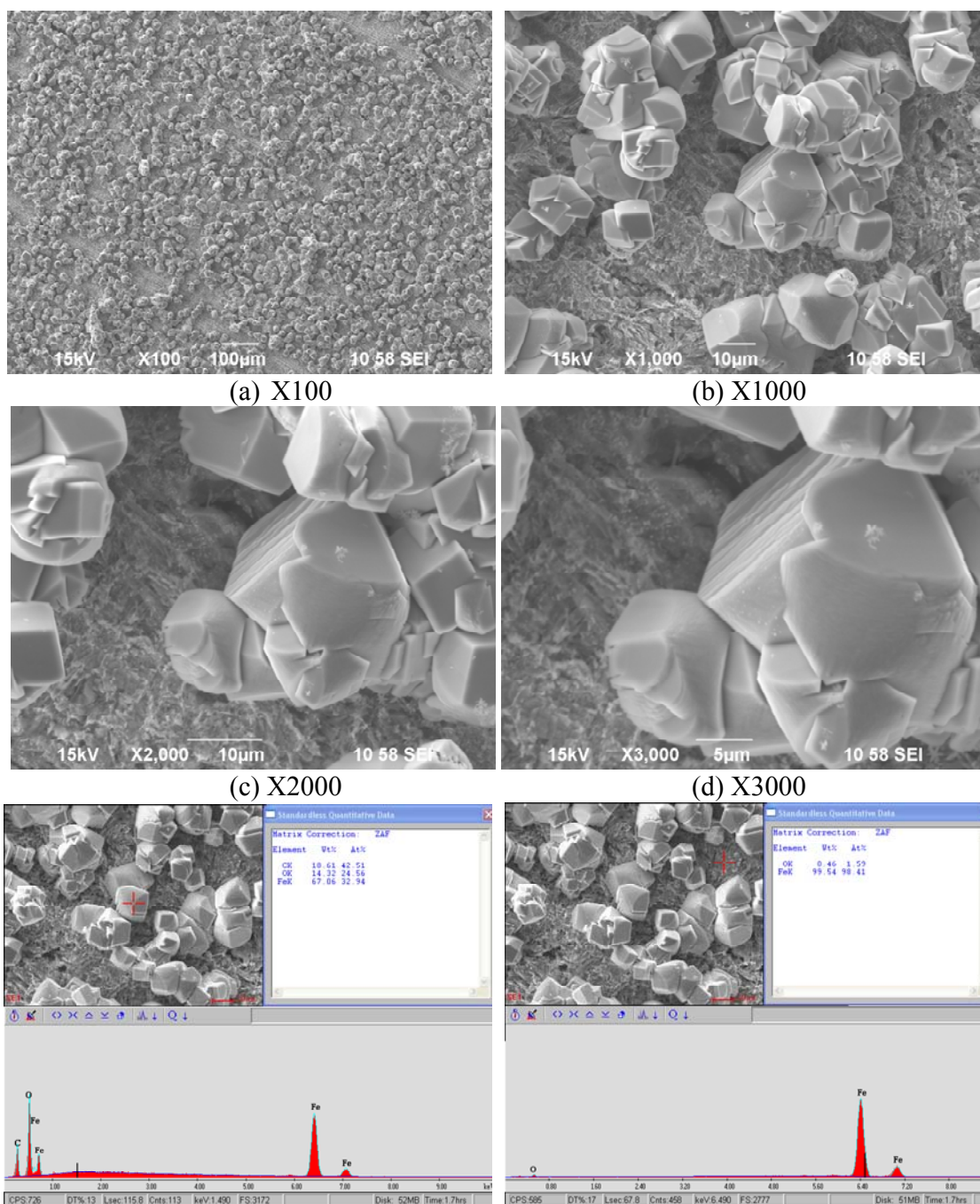


Figure 47. SEM images of the specimen surface after dissolution by pH 3.8 test solution for 5 minutes.

Then the specimen was placed in the pH 3.8 test solution again for 15 hours. The SEM images of this specimen are shown in Figure 48. It can be clearly seen that only prism shaped iron carbonate crystals were left on the surface and all plate shaped iron carbonate was dissolved. According to the EDS analysis, the voids between the crystals only showed iron, which means the bare steel surface was exposed after dissolution and the protection from iron carbonate layer was gone.



(f) EDS of a  $\text{FeCO}_3$  crystal  
 (g) EDS of the void among crystals  
 Figure 48. SEM and EDS images of the specimen surface after dissolution by pH 3.8 test solution for 15 hours.

Although the dissolution of iron carbonate layer observed by SEM showed some interesting features, the tests were only qualitative and no detailed information was acquired. Quantitative characterization of iron carbonate dissolution needs to be done in order to understand how dissolution happens and what effect it has on the steel substrate. Therefore, a quantitative study of iron carbonate dissolution was conducted as shown in the following sections.

### **5.3 Iron carbonate formation and dissolution in a glass cell with a rotating cylinder electrode setup**

#### *5.3.1 Experimental method*

##### 5.3.1.1 Test setup

A glass cell with a rotating cylinder electrode setup was used for the iron carbonate dissolution study. The schematic of the setup was shown in Figure 4 in section 4.2.1.1, where detailed information can be found.

##### 5.3.1.2 Test matrix

The test matrix of iron carbonate dissolution conducted in a glass cell with rotating cylinder electrode setup is shown in Table 11.

Table 11. Text matrix for iron carbonate layer dissolution in a glass cell with a rotating cylinder electrode setup.

Parameters	Layer formation	Layer dissolution
Material	C1018	
Solution	1 wt% NaCl	
Temperature	80°C	
CO <sub>2</sub> partial Pressure	0.52 bar	
pH	6.6	5.6
Initial saturation level	300	0.3
Rotating speed	0	100 rpm

### 5.3.1.3 Test procedure

An iron carbonate layer was formed on carbon steel specimen with the same procedure explained in section 4.2.1.3. After the protective layer was formed, one specimen was taken out of the glass cell for surface analysis. The solution pH was adjusted by adding deoxygenated HCl to the desired value. The rotating cylinder electrode was rotated at 100 rpm to develop a well defined flow condition. Corrosion rate and corrosion potential were measured continuously during iron carbonate dissolution. Solution pH and ferrous ion concentration were also monitored periodically. At the end of the test, the specimen was taken out for surface analysis.

### 5.3.2 Results and discussion

Figure 49 shows the change of corrosion rate and corrosion potential in one of the dissolution tests. A protective iron carbonate layer was formed under a high initial

supersaturation (pH 6.6, 80°C, and SS ( $\text{FeCO}_3$ )  $\gg$  1). Corrosion rate decreased and corrosion potential increased due to the formation of a protective layer. When the pH of the solution was adjusted to achieve an under-saturation level of 0.3, the corrosion potential decreased and corrosion rate increased immediately, which indicated the loss of protection by the iron carbonate layer due to dissolution.

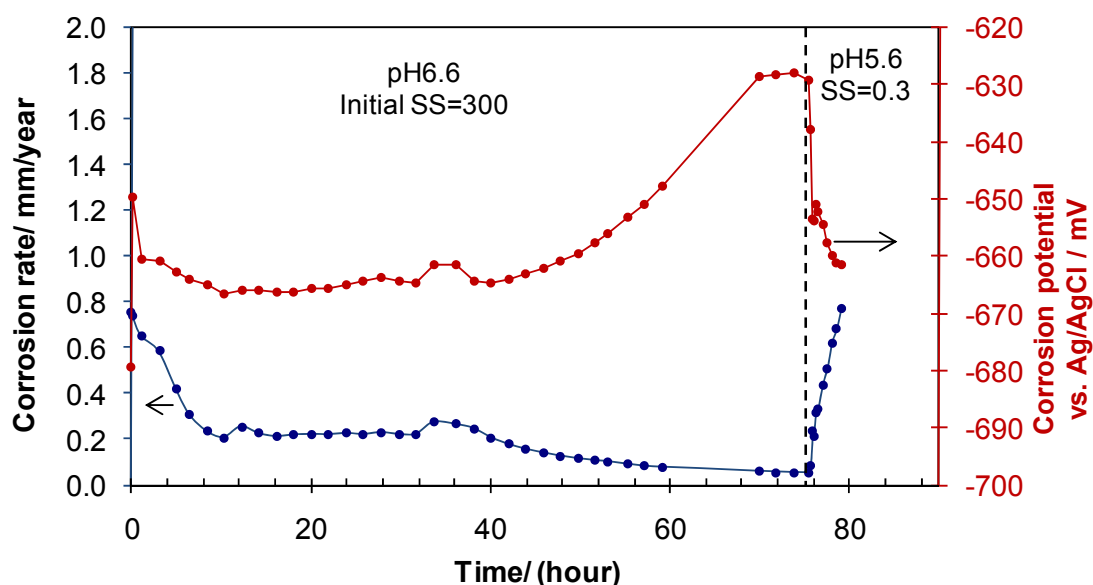


Figure 49. Change of corrosion rate and corrosion potential during iron carbonate layer formation (pH 6.6, initial S=300, stagnant) and dissolution (pH 5.6, initial S=0.3, 100 rpm) in 1 wt% NaCl at 80°C. Test was conducted with RCE glass cell setup.

SEM images taken before (when layer formation was finished) and after the dissolution process are shown in Figure 50. It can be seen that there was a protective layer formed on the surface of the steel specimen before the dissolution took place. After dissolution, many iron carbonate crystals were gone and the underlying steel substrate was exposed, which was the cause of the corrosion rate increase observed during the test.

Tests using the same procedure were also conducted at different pH for iron carbonate dissolution process and a similar phenomenon was observed.

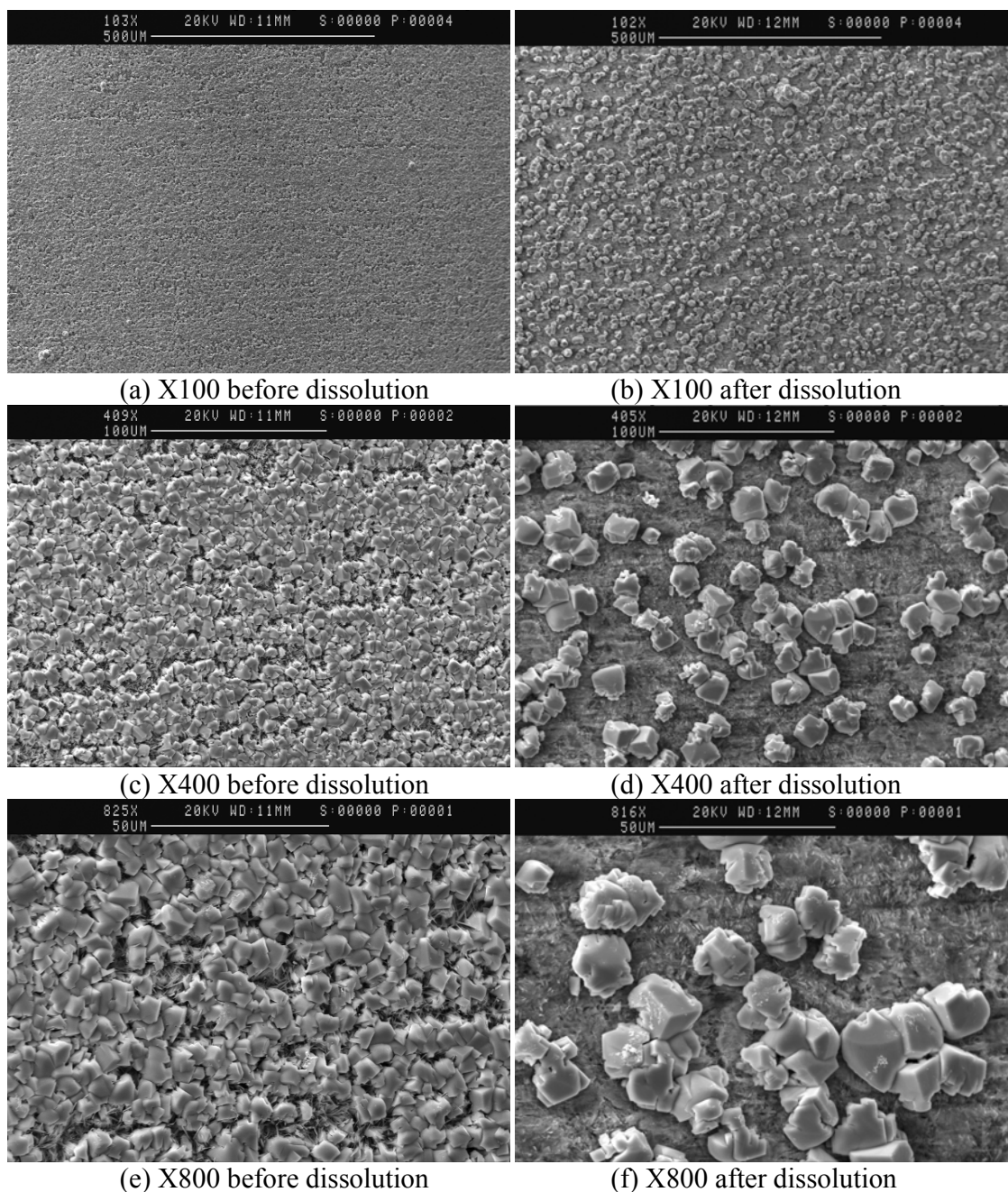


Figure 50. SEM images of the iron carbonate layer before (pH 6.6, initial  $S=300$ , stagnant) and after dissolution (pH 5.6, initial  $S=0.3$ , 100 rpm) in 1 wt% NaCl at 80°C. Test was conducted with RCE glass cell setup.

Although the conclusions obtained from the RCE tests seem to be valid, they do not constitute a direct measurement of iron carbonate layer dissolution. The change of

corrosion rate and corrosion potential were the results of dissolution, but not ideal parameters to quantify the dissolution process. By using an electrochemical quartz crystal microbalance (EQCM), the mass change due to the dissolution of the protective iron carbonate layer can be directly monitored, so it is a more suitable technique for the current study.

#### **5.4 Iron carbonate layer formation and dissolution in a glass cell with an electrochemical quartz crystal microbalance and a jet impingement setup**

##### *5.4.1 Calibration of electrochemical quartz crystal microbalance*

###### 5.4.1.1 Experimental method

###### 5.4.1.1.1 Test setup

The EQCM device is shown in Figure 51 and the quartz crystal (5 MHz resonance frequency) coated with gold is shown in Figure 52. Quartz crystals coated with different material (iron, platinum and etc.) were also used in the tests.

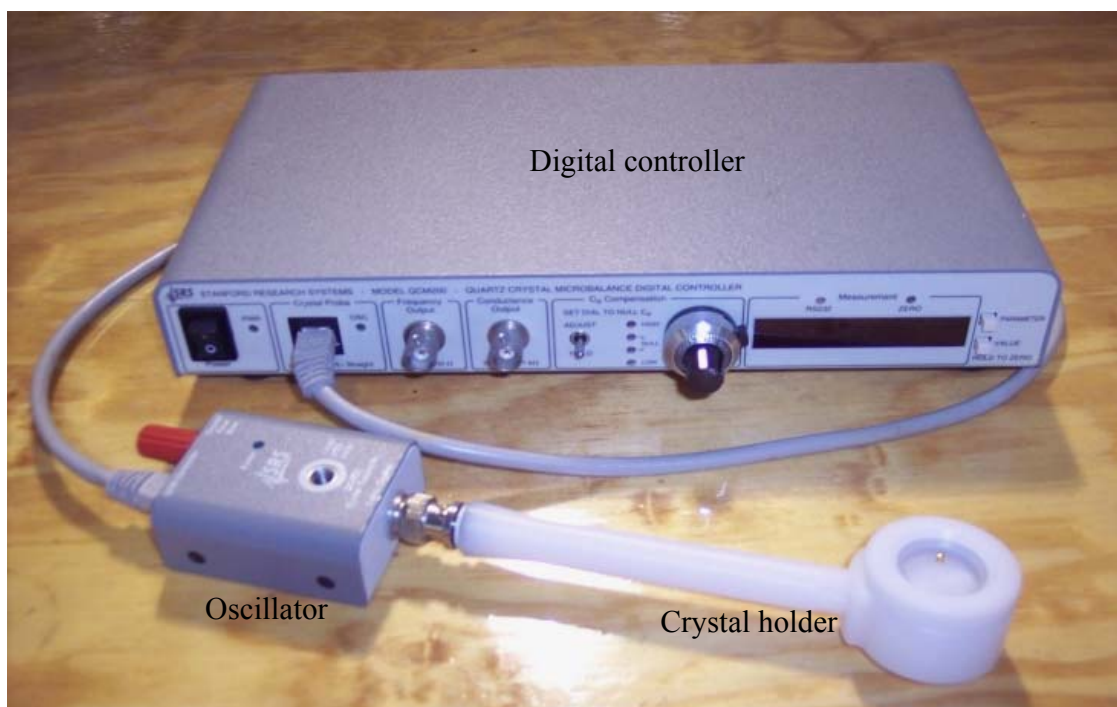


Figure 51. EQCM device (QCM200 from Stanford Research Systems).



Figure 52. Quartz crystal coated with gold.

The schematic of glass cell with EQCM setup is shown in Figure 53. This is a three electrode system, similar to the glass cell setup with rotating cylinder electrode, except that the working electrode was replaced by a quartz crystal.

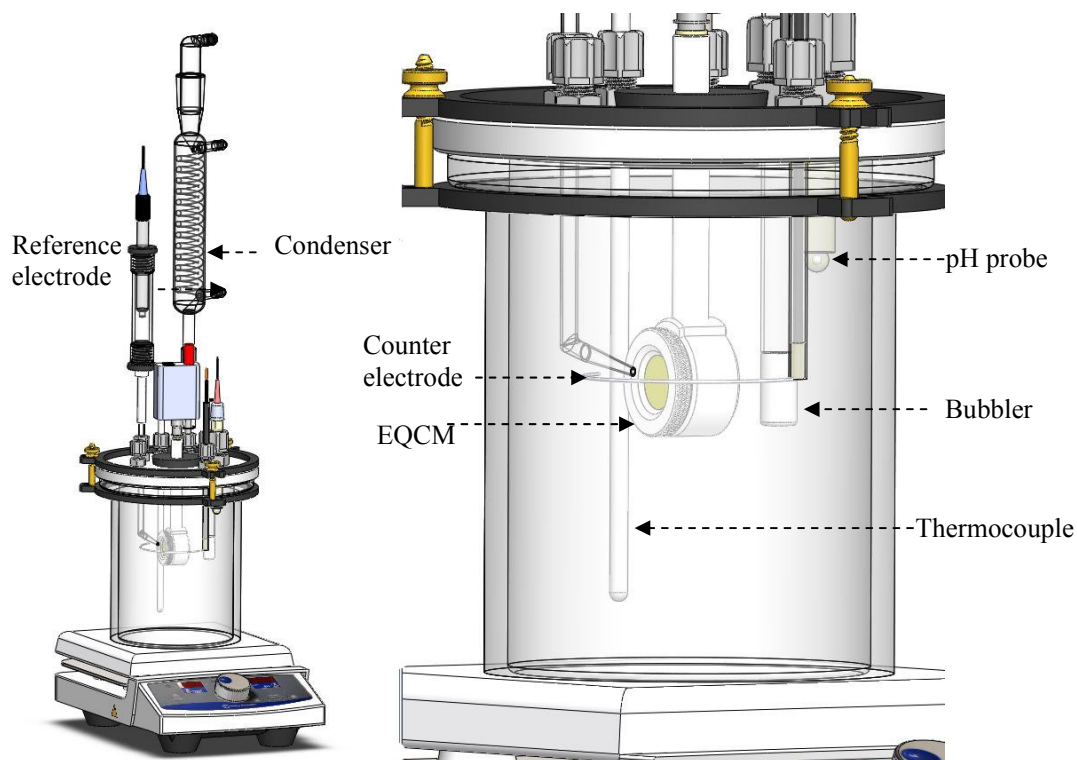


Figure 53. Glass cell setup with EQCM (courtesy of Cody Shafer).

#### 5.4.1.1.2 Test matrix

The test matrix for EQCM calibration tests is shown in Table 12.

Table 12. Test matrix for EQCM calibration.

Parameter	Calibration
Material	Polished gold and iron coated quartz crystal
Solution	1 wt% NaCl
CO <sub>2</sub> partial pressure	0.96 bar, 0.52 bar
Temperature	25°C, 80°C
pH	4.0

#### 5.4.1.1.3 Test procedure

The experiments were all conducted in distilled water with 1 wt% NaCl, which was deaerated by CO<sub>2</sub> in advance and stabilized at the designated temperature. The pH of the solution was then adjusted by adding NaHCO<sub>3</sub> to the desired test condition. During the test, CO<sub>2</sub> was bubbled continuously. Gold coated and iron coated quartz crystals were cleaned with N<sub>2</sub> gas stream before tests to remove any dust from the surface. Then the crystal was immersed into the prepared solution for testing. SEM and EDS were used for surface analysis as needed.

#### 5.4.1.2 Results and discussion

There is a linear relationship between the mass change on the quartz crystal surface and the resonance frequency as described by Sauerbrey (1959) equation as shown in Equation (28).

$$\Delta f = -C_f \Delta m \quad (28)$$

where  $\Delta f$  is the frequency change (Hz),  $C_f$  is the sensitivity factor for the quartz crystal (56.6 Hz/( $\mu\text{g}\cdot\text{cm}^2$ )),  $\Delta m$  is the mass change on the crystal surface ( $\mu\text{g}/\text{cm}^2$ ).

Before using EQCM in the layer formation and dissolution study, it was necessary to prove that EQCM was able to provide reasonable and accurate measurement. So the first step was to calibrate EQCM under the desired test conditions. As shown in Table 12, the EQCM was calibrated at 25°C and 80°C with gold and iron coated quartz crystals.

The change in resonance frequency when a quartz crystal was exposed to a viscous media could be calculated (Kanazawa & Gordon, 1985). When a gold coated

quartz crystal (5 MHz) was exposed to 1 wt% NaCl solution at 25°C, a change of about 750 Hz in resonance frequency was expected, which is equal to 13.2  $\mu\text{g}/\text{cm}^2$  change in mass according to Sauerbrey equation. Figure 54 shows the measured 13.6  $\mu\text{g}/\text{cm}^2$  change in mass when gold coated quartz crystal was exposed to 1 wt% NaCl solution at 25°C, which showed a reasonable agreement with the calculation.

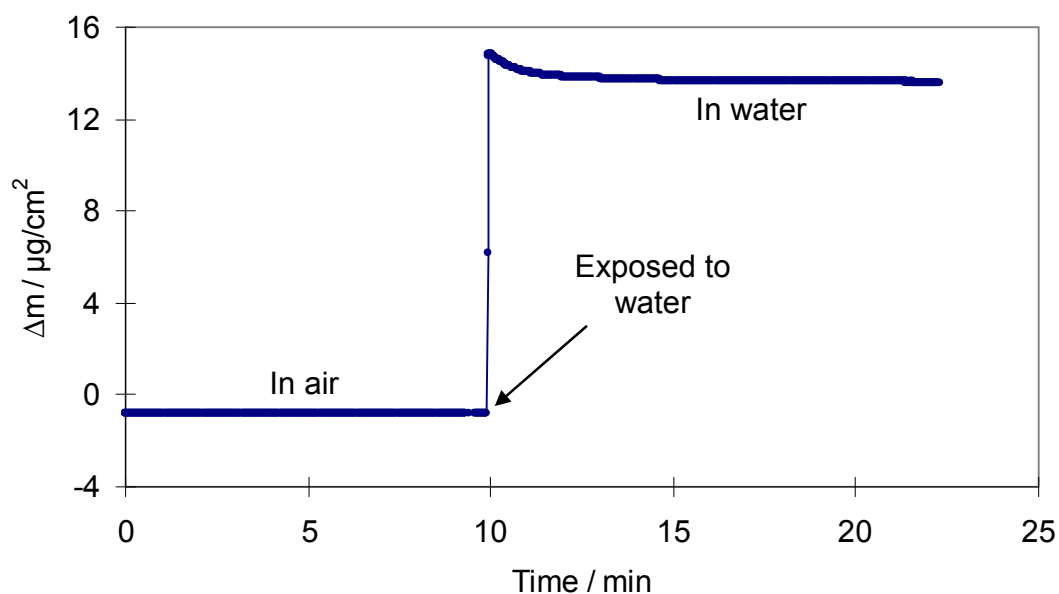


Figure 54. Signal change of EQCM when exposed to 1 wt% NaCl (5 MHz, gold coated quartz crystal, 25°C).

The resonance frequency of the quartz crystal was also a function of temperature. As shown in Figure 55, when the gold coated quartz crystal was exposed to the 1 wt% NaCl solution at 80°C, the resonance frequency first increased (resulting in a decrease of mass) and then decreased (corresponding to an increase in mass) until it became stable.

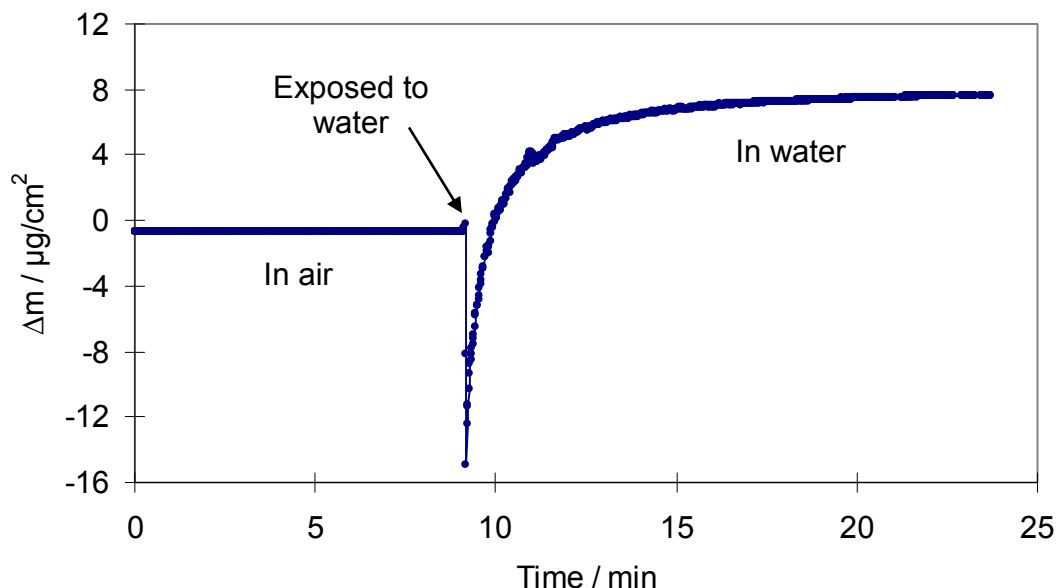


Figure 55. Signal change of EQCM when exposed to 1 wt% NaCl (5 MHz, gold coated quartz crystal, 80°C).

It was expected that when the iron coated quartz crystal was exposed to the CO<sub>2</sub> corrosion environment, the coated iron would dissolve away due to corrosion. The mass change detected by EQCM and the corrosion rate of iron measured by electrochemical means can be correlated by using Faraday's Law to confirm the validity of EQCM measurement.

$$\Delta m' = \frac{ItW}{nA_s F} \quad (29)$$

where  $\Delta m'$  is the weight change of metal in g/m<sup>2</sup>, I is current in A, t is time in s, W is the atomic weight of the metal (g/mol), n is the valence charge of the dissolved metal in solution (mol electrons per mol reaction), A<sub>s</sub> is the specimen surface area in m<sup>2</sup>, F is Faraday's constant (96485 C/mol). Figure 56 shows the signal change of an iron coated

quartz crystal when exposed to CO<sub>2</sub> purged 1 wt% NaCl solution at pH 4.0 at room temperature.

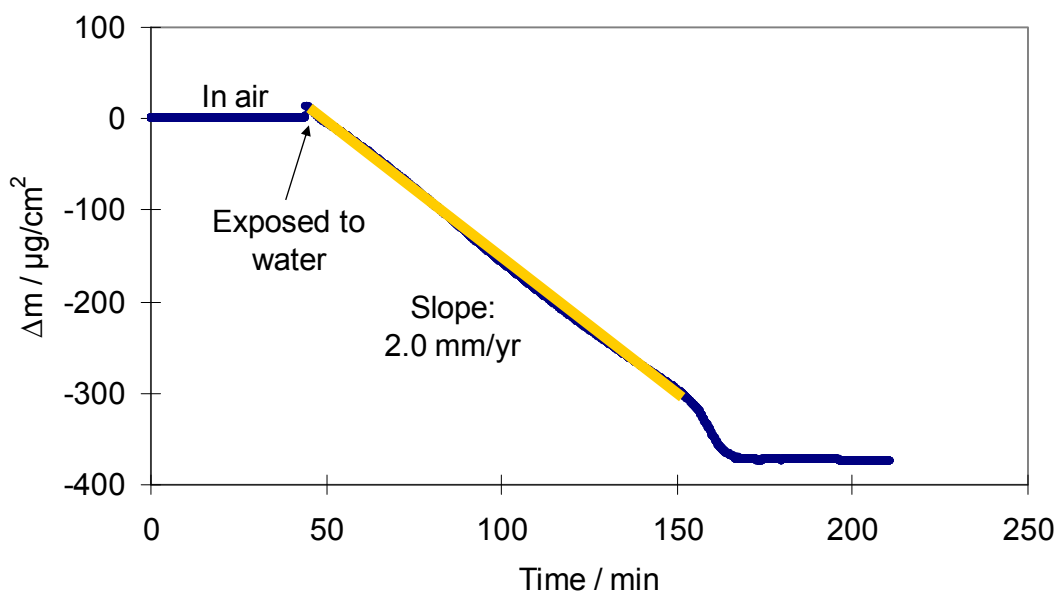


Figure 56. Signal change of EQCM when exposed to 1 wt% NaCl without electrochemical measurement (5 MHz, 0.5 μm iron coated quartz crystal, 25°C).

It was shown that there was a signal change due to the contact with liquid phase followed by a linear mass loss due to corrosion. At the end of this test, there was no mass change detected since the iron coating was corroded away completely. This was proven by EDS analysis made on the crystal surface after this test, which showed pure Si and O element with no iron left (Figure 57). The total weight loss measured by EQCM was 386 μg/cm<sup>2</sup>, which matched well with the amount of iron coated on the crystal (394 μg/cm<sup>2</sup>). The weight change of the crystal measured by an analytical balance was 170 μg/cm<sup>2</sup>. The error of the balance is within 0.1 mg, which is of the same order of magnitude as the mass

change during the test. Therefore the analytical balance could not be used for validation purposes in this case.

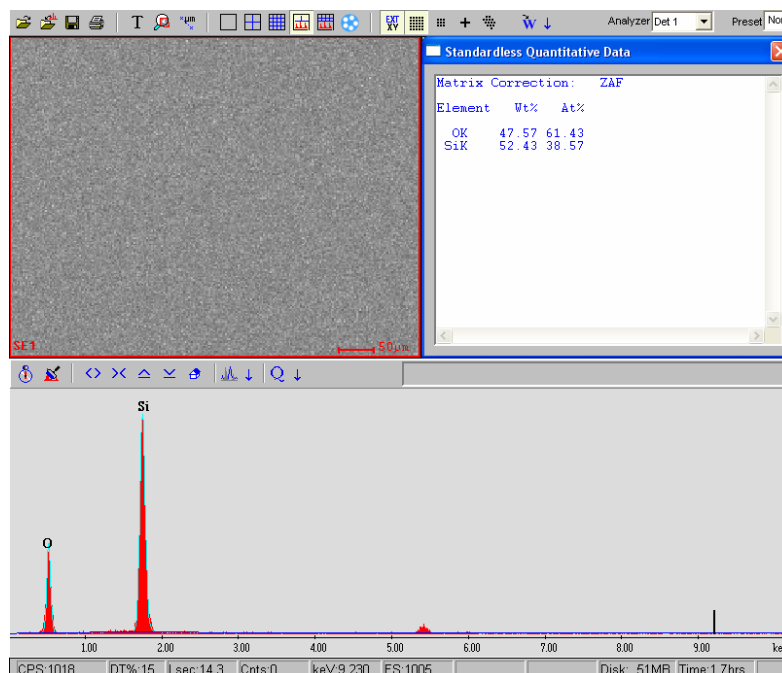


Figure 57. EDS analysis of the iron (0.5  $\mu\text{m}$ ) coated quartz crystal after corrosion test.

Calibration tests were also made by applying a galvanostatic current to the iron coated quartz crystal. As shown in Figure 58, initially the iron coating corroded spontaneously when exposed to the test solution. Then a galvanostatic current which is equivalent to 10 mm/year corrosion rate was applied to the crystal (see highlighted part). The slope change of the mass change curve obtained by EQCM indicated a 9.7 mm/yr corrosion rate.

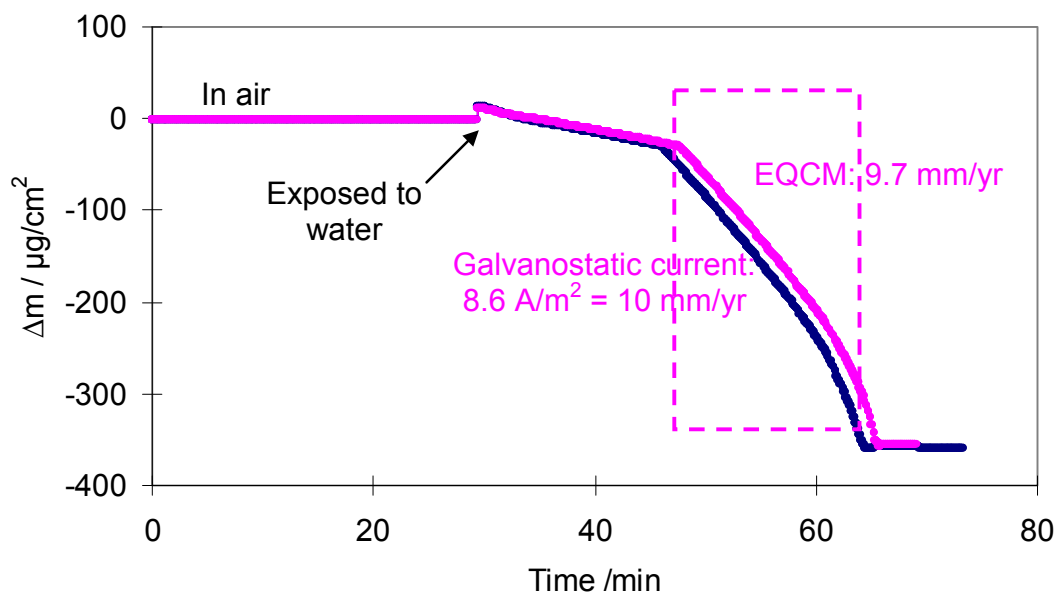


Figure 58. Mass change of the iron coated quartz crystal when controlled by galvanostatic current (1 wt% NaCl, 25°C).

Another two tests were made at 80°C to confirm the validation of EQCM measurement at high temperature. As shown in Figure 59, the iron coated quartz crystal was exposed to 1 wt% NaCl solution at 80°C and corroded until all the coated iron was lost. The corrosion rate appeared to be higher due to the elevated temperature. A controlled galvanostatic corrosion test was also conducted and it showed reasonable results as seen in Figure 60.

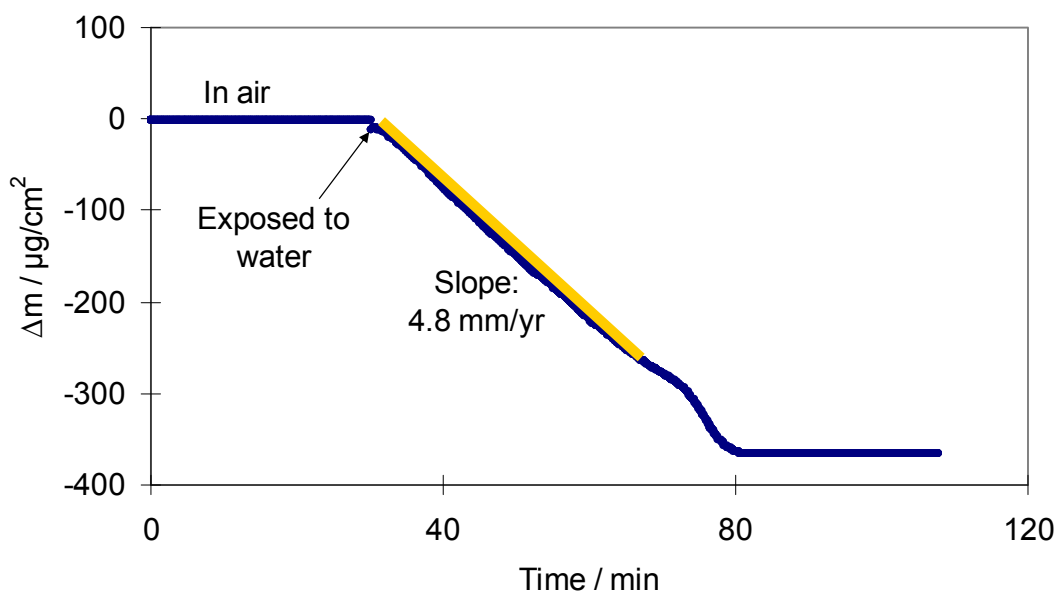


Figure 59. Mass change of the iron coated quartz crystal when exposed to 1 wt% NaCl solution at 80°C.

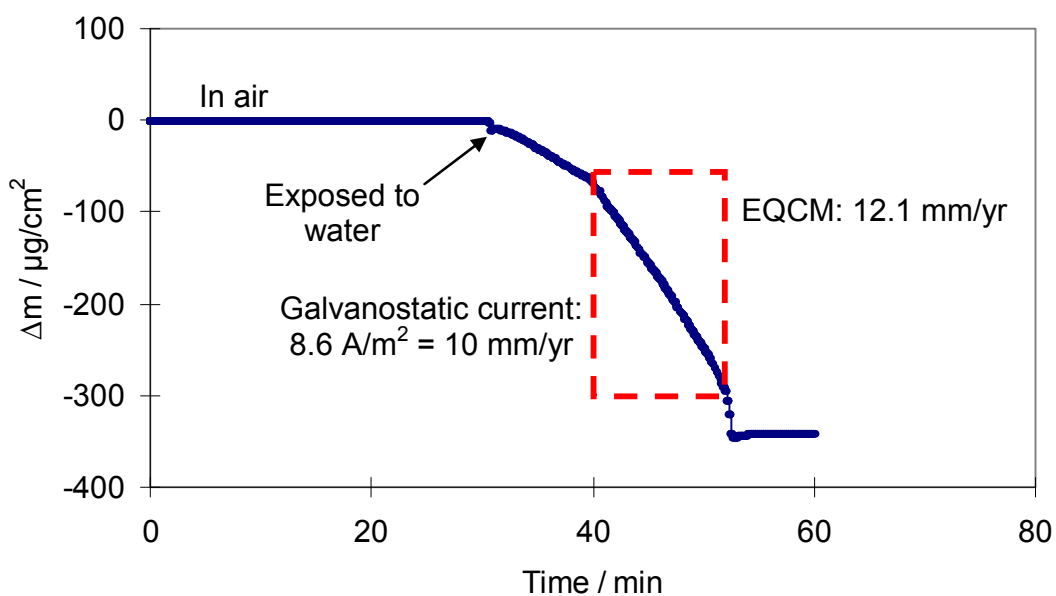


Figure 60. Mass change of the iron coated quartz crystal when controlled by galvanostatic corrosion at 80°C.

Tests were also done by exposing the iron coated quartz crystal to the test solution at higher pH. Figure 61 shows the mass change of an iron coated quartz crystal after being exposed to the test solution at 80°C and pH 6.6 in two repeated tests.

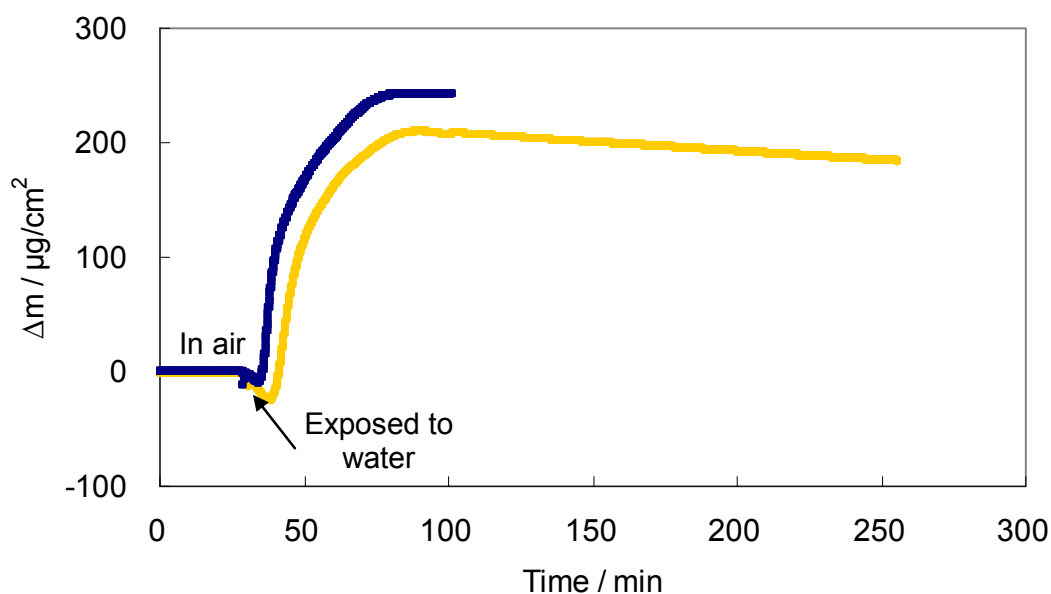


Figure 61. Iron carbonate precipitation on the iron coated quartz crystal surface at pH 6.6, initial SS=0, 80°C, 1 wt% NaCl solution.

It was noticed that at first the mass decreased due to corrosion and then increased. This was because the ferrous ion concentration at the surface increased due to corrosion of iron and therefore the solution was supersaturated at the surface and caused iron carbonate precipitation. After a while, the mass increase slowed down, stabilized and then started to decrease gradually. This was because the bulk solution was undersaturated and iron carbonate formation and dissolution reached steady state. SEM pictures of the surface after the test are shown in Figure 62. Some iron carbonate crystals are shown on

the surface, but the appearance was not similar to the one formed on carbon steel surface, since what was seen here represents only the initial stage of the layer formation. However, these tests showed the possibility of studying the dissolution process with EQCM.

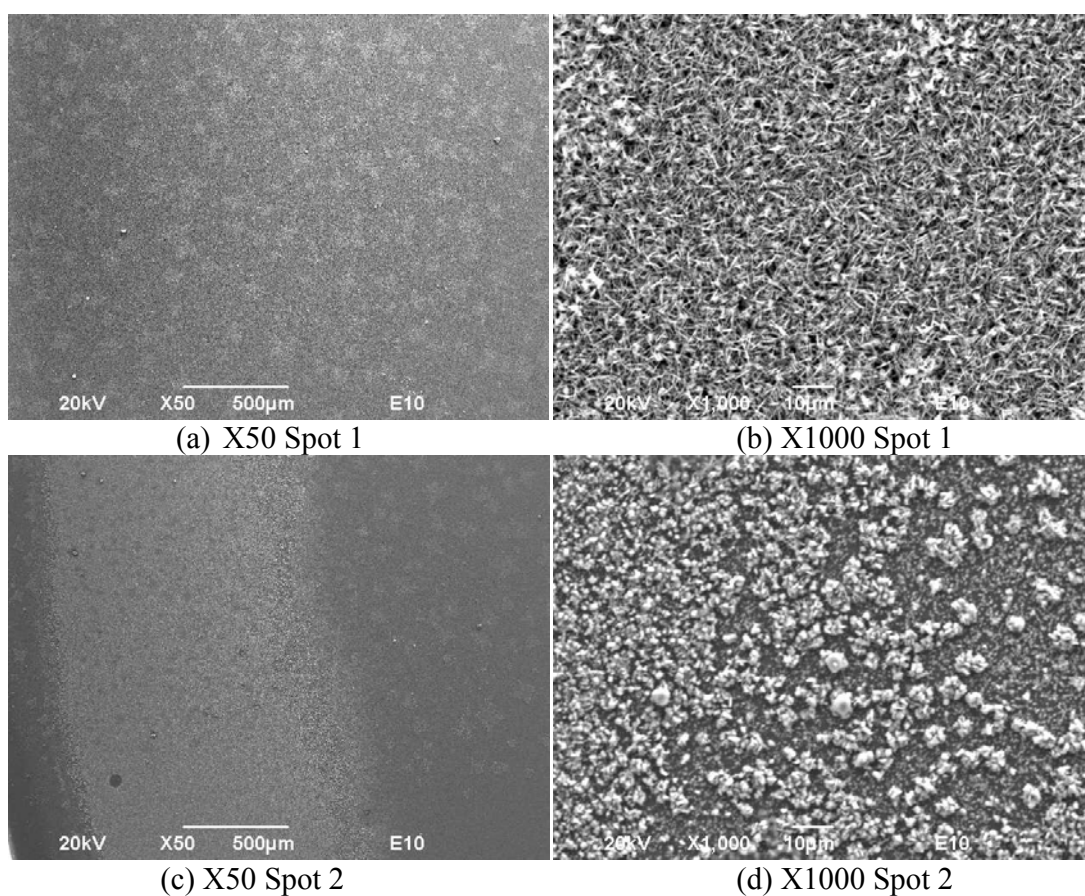


Figure 62. SEM analysis of the iron carbonate layer formed on iron coated quartz crystal at pH 6.6, initial  $S=0$ ,  $80^{\circ}\text{C}$ , 1 wt% NaCl solution.

#### 5.4.2 Iron carbonate layer formation and dissolution on an iron coated quartz crystal

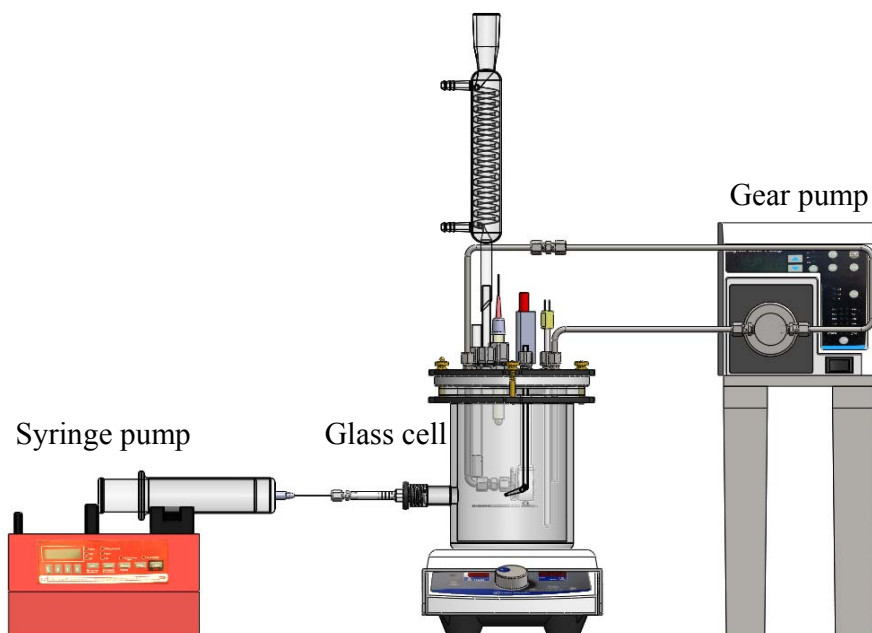
Since EQCM provided reasonable measurements in the abovementioned calibration tests, the next step was to try to form a realistic iron carbonate layer on the

quartz crystal surface and observe the mass change due to dissolution. The test was conducted with iron coated quartz crystal since it was expected that the coated iron would behave similarly to carbon steel.

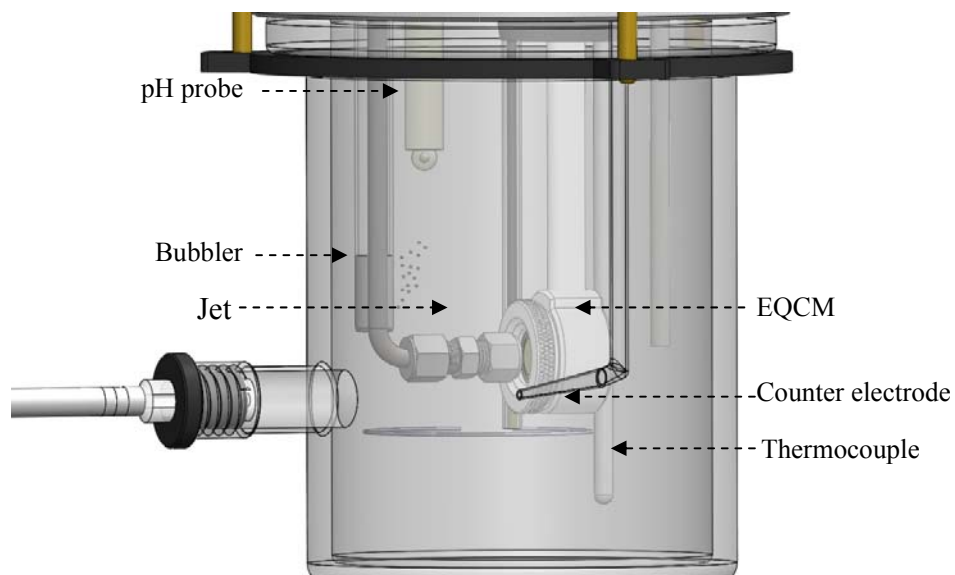
#### 5.4.2.1 Experimental method

##### 5.4.2.1.1 Test setup

A schematic of the glass cell setup with EQCM and jet impingement is shown in Figure 63. A gear pump was used to circulate the test solution from the glass cell and create an impinging jet flow on the quartz crystal surface. The nozzle of the jet was 1 mm and the distance between the jet nozzle and the EQCM surface was 5 mm. In order to adjust the solution pH slowly during the dissolution test, a syringe pump was connected to the glass cell through a side port.



(a) The complete setup



(b) Zoom in of EQCM and jet impingement

Figure 63. Schematic of the glass cell setup with QCM and jet impingement (courtesy of Cody Shafer).

#### 5.4.2.1.2 Test matrix

The test matrix for iron carbonate layer formation and dissolution on iron coated quartz crystal is shown in Table 13.

Table 13. Test matrix for the iron carbonate layer formation and dissolution on polished iron coated quartz crystal.

Parameter	Layer formation	Layer dissolution
Material	Polished iron coated quartz crystal	
Solution	1 wt% NaCl	
CO <sub>2</sub> partial pressure	0.52 bar	
Temperature	80°C	
pH	6.6	5.8
Initial S of FeCO <sub>3</sub>	600	0.3

#### 5.4.2.1.3 Test procedure

Experiments were conducted in a 2 liter glass cell with 1 wt% NaCl solution, which was deaerated by CO<sub>2</sub> in advance of the tests for at least 2 hours. CO<sub>2</sub> sparging was maintained throughout the entire test. Once the solution was heated and stabilized at the desired temperature, the pH of the solution was adjusted by adding reagent grade NaHCO<sub>3</sub> to achieve the desired value. Prior to immersion, the iron coated quartz crystal was cleaned with a N<sub>2</sub> gas stream to remove any dust from the surface. A deaerated ferrous chloride (FeCl<sub>2</sub>·4H<sub>2</sub>O) solution was added to the solution to provide additional Fe<sup>2+</sup> and increase the saturation level of iron carbonate. A potentiostat was used during

the tests for electrochemical measurements as described below. The mass change on the quartz crystal surface was monitored by EQCM throughout all the tests. A spectrophotometer was used to measure the  $\text{Fe}^{2+}$  concentration as necessary. The solution pH was followed throughout the test.

#### 5.4.2.2 Results and discussion

##### 5.4.2.2.1 Iron carbonate layer formation

Since the surface of an iron coated quartz crystal is more similar to a carbon steel surface, it was expected that a realistic iron carbonate layer would form on it. Because the surface of an iron coated quartz crystal will corrode and release ferrous ions, it was expected that an iron carbonate layer could form on it, when the saturation level of the solution became higher than 1. However, to speed the process up, at the beginning of the test, additional  $\text{Fe}^{2+}$  ions were added to the test solution (in the form of a deoxygenated  $\text{FeCl}_2 \cdot 4\text{H}_2\text{O}$  solution) to achieve a high initial supersaturation of iron carbonate, in order to accelerate protective layer formation. Figure 64 shows that the mass change monitored by the EQCM increased every time when the saturation level was increased, which indicated that the iron carbonates precipitated on the surface due to the high supersaturation. In each case, after some time, the mass increase slowed down, indicating that the precipitation rate decreased as the solution supersaturation dropped spontaneously. At the end of the test, the specimen was taken to the SEM for surface analysis.

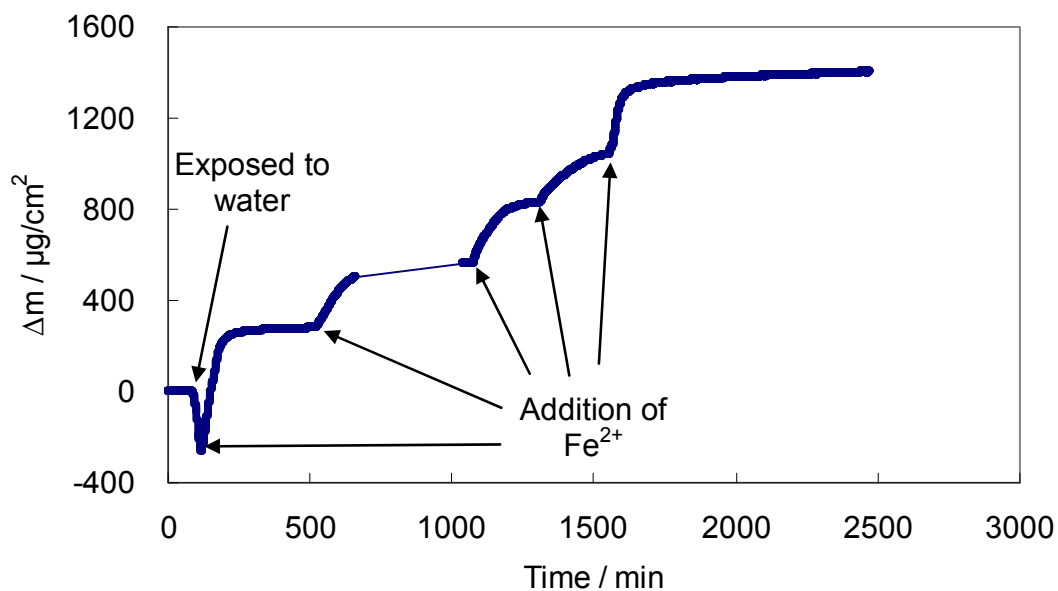


Figure 64. Iron carbonate precipitation on an iron coated quartz crystal surface at pH 6.6, initial SS=600, 80°C, 1 wt% NaCl solution.

The SEM pictures (Figure 65) show the surface was uniformly covered with an iron carbonate layer. Even though this experiment was conducted by using a pure iron coated quartz crystal specimen, the iron carbonate layer was considered to be realistic, as it was alike to the one formed on a mild steel specimen (shown in Figure 66), exposed to similar conditions in a separate experiment. This appeared to be promising and further layer dissolution experiments were planned based on the current results.

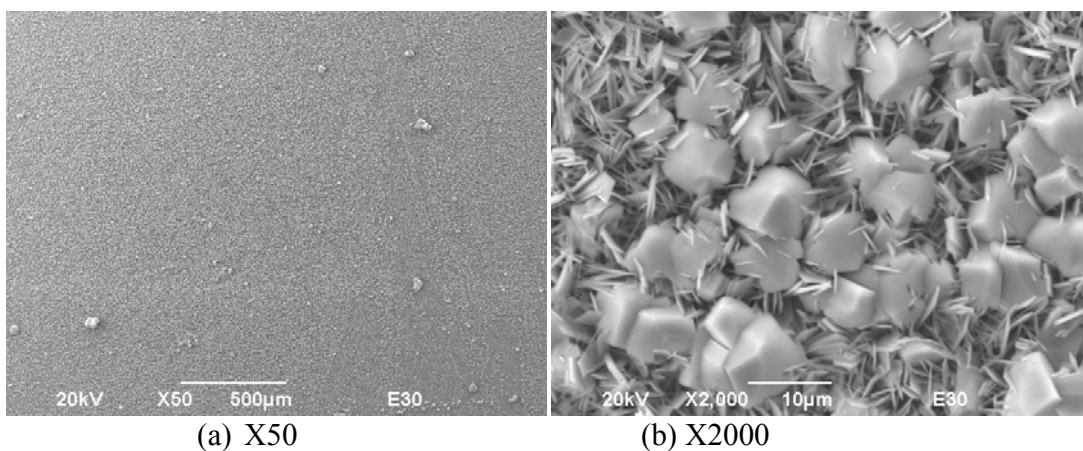


Figure 65. SEM analysis of the iron carbonate film formed on an iron coated quartz crystal at pH 6.6, initial SS=120, 80°C, 1 wt% NaCl solution.

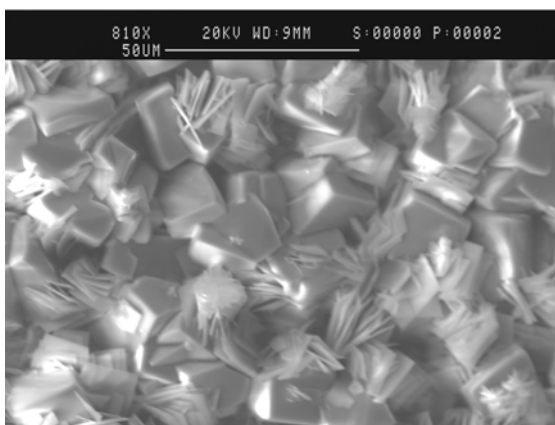


Figure 66. SEM analysis of the iron carbonate layer formed on carbon steel at pH 6.6, initial SS=300, 80°C, 1 wt% NaCl solution.

#### 5.4.2.2.2 Iron carbonate layer dissolution

Dissolution tests were done using EQCM under a well developed jet impingement flow. Figure 67 shows the mass change of an iron coated quartz crystal monitored by EQCM in an iron carbonate formation and dissolution test at 1.3 m/s jet impingement flow. Figure 68 shows the corrosion rate and corrosion potential monitored during this process. Comparing Figure 67 with Figure 68, it can be seen that the mass increased as

the corrosion rate decreased and the corrosion potential increased about 100 mV. This suggests the increase of the mass was due to the protective layer formed on the iron coated quartz crystal surface.

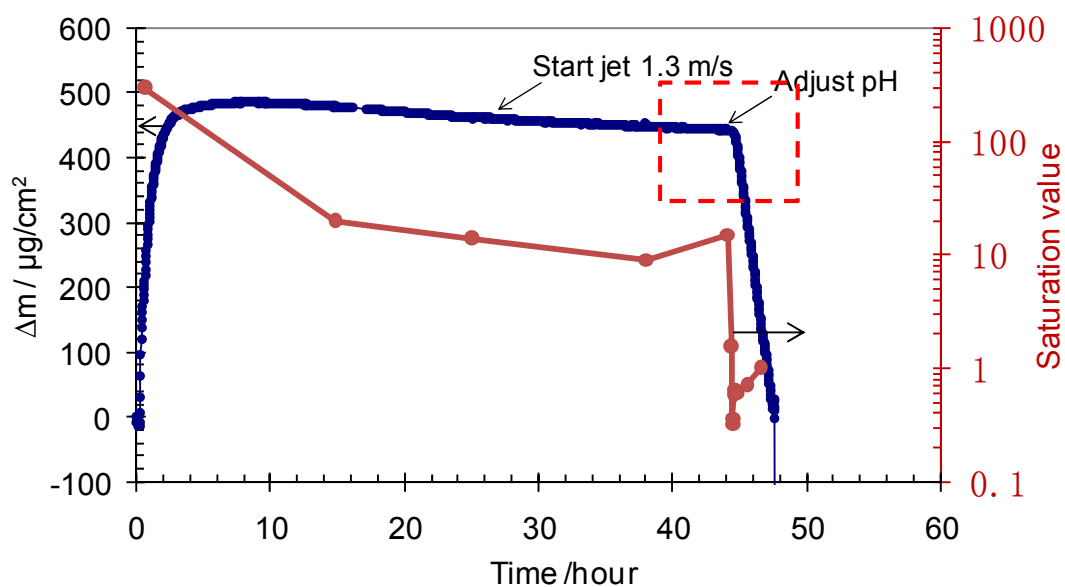


Figure 67. Mass change of the iron crystal monitored by EQCM in layer formation and dissolution test under jet impingement, pH 6.6, initial SS=300, dissolution pH 5.8, 80°C, 1 wt% NaCl, jet velocity 1.3 m/s.

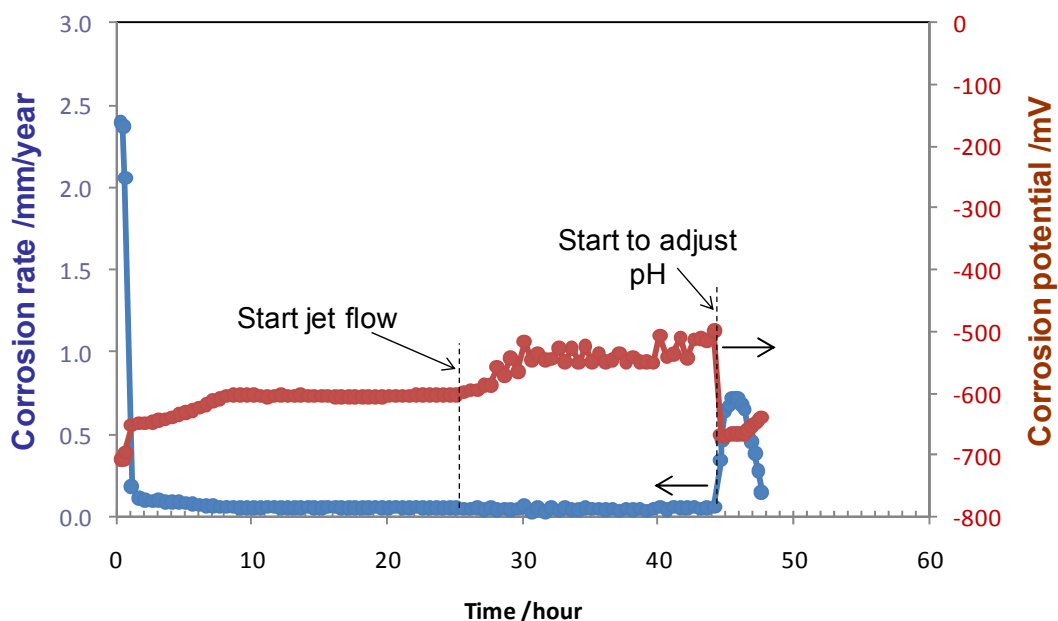


Figure 68. Change of corrosion rate and corrosion potential of the iron coated quartz crystal in iron carbonate layer formation and dissolution test under jet impingement, pH 6.6, initial SS=300, dissolution pH 5.8, 80°C, 1 wt% NaCl.

After the protective layer was formed, a jet flow with 1.3 m/s was started and there was no significant change in mass, which suggested that the jet flow did not mechanically affect the protective iron carbonate layer. Then the pH of the solution was adjusted to 5.8, which corresponded to an under-saturation value of 0.3 with respect to iron carbonate. The mass recorded by EQCM decreased sharply while corrosion rate increased. A mass decrease rate was calculated and was equivalent to 1.7 mm/year corrosion rate. However, due to the corrosion of iron on the coated quartz crystal, it was difficult to distinguish the contribution by iron carbonate dissolution from iron corrosion in the overall mass loss. The two mechanisms needed to be separated.

### 5.4.3 Iron carbonate layer formation and dissolution on a gold coated quartz crystal

A gold coated quartz crystal is very stable and commonly used in EQCM studies. Besides, as a noble metal, gold does not corrode as iron in a CO<sub>2</sub> corrosion environment. Therefore it was possible to study iron carbonate formation and dissolution on a gold coated quartz crystal, given that a layer of iron carbonate can be built on gold.

#### 5.4.3.1 Experimental method

##### 5.4.3.1.1 Test setup

The same glass cell setup with EQCM and jet impingement was used as shown in Figure 63.

##### 5.4.3.1.2 Test matrix

The test matrix for iron carbonate layer formation and dissolution on polished gold coated quartz crystal is shown in Table 14.

Table 14. Test matrix for iron carbonate layer formation and dissolution on a gold coated quartz crystal.

Parameter	Layer formation	Layer dissolution
Material	Polished gold coated quartz crystal	
Solution	1 wt% NaCl	
CO <sub>2</sub> partial pressure	0.52 bar	
Temperature	80°C	
pH	6.6	5.5, 5.0

#### 5.4.3.1.3 Test procedure

The test procedure was similar to the one shown in section 5.4.2.1.3. In addition, a polarization of the gold crystal at a cathodic potential was used when necessary.

#### 5.4.3.2 Results and discussion

##### 5.4.3.2.1 Iron carbonate layer formation

Since a gold coated quartz crystal does not corrode to release ferrous ion, a high supersaturation with respect to iron carbonate was used to achieve the layer formation on a gold coated quartz crystal by adding ferrous ions into the solution at the beginning of the test. Figure 69 shows the mass increase with initial supersaturation of 900. It was noticed that the precipitation rate changed as the  $\text{Fe}^{2+}$  was consumed with time.

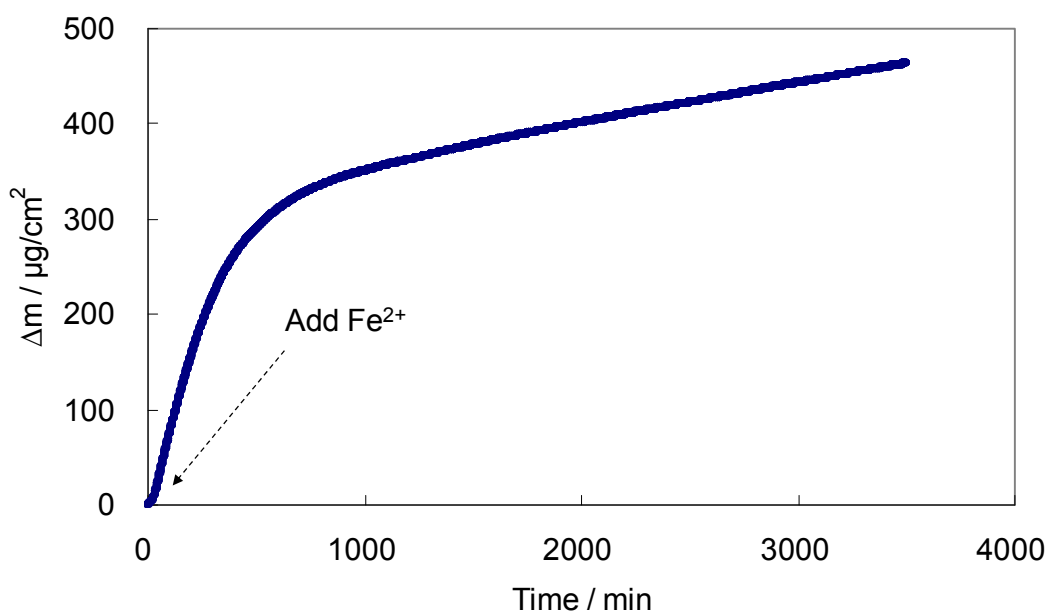


Figure 69. Iron carbonate precipitation on a gold coated quartz crystal at pH 6.6, initial SS=900, 80°C, 1 wt% NaCl solution.

Figure 70 shows the SEM images of the surface of the crystal after the test. It can be seen that the surface of the quartz crystal was non-uniformly covered by iron carbonate crystals, which was further confirmed by EDS analysis in Figure 71.

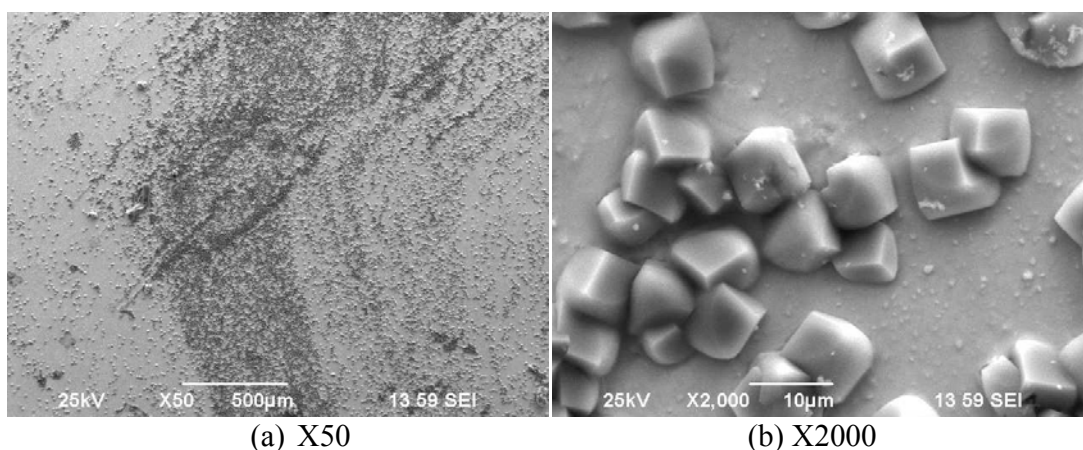


Figure 70. SEM analysis of the iron carbonate layer formed on a gold coated quartz crystal at pH 6.6, initial SS=900, 80°C, 1 wt% NaCl solution.

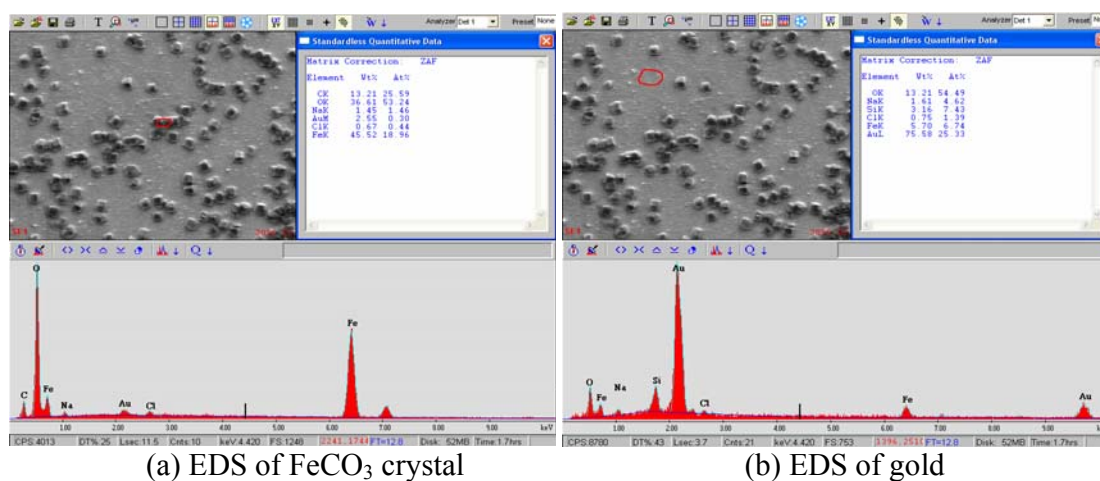


Figure 71. EDS analysis of the iron carbonate layer formed on a gold coated quartz crystal at pH 6.6, initial SS=900, 80°C, 1 wt% NaCl solution.

In order to build a more uniformly covered layer on a gold coated quartz crystal, the crystal was polarized cathodically to create a high pH level at the surface to facilitate

iron carbonate formation. A layer formation test was done by polarizing the gold crystal to -1000 mV with respect to saturated Ag/AgCl reference electrode. The results are shown in Figure 72 and SEM pictures are shown in Figure 73. From the EDS analysis shown in Figure 74, it can be seen that instead of forming iron carbonate,  $\text{Fe}^{2+}$  was reduced to Fe on the crystal surface due to the highly negative potential, which fell into the ferrous ion reduction region.

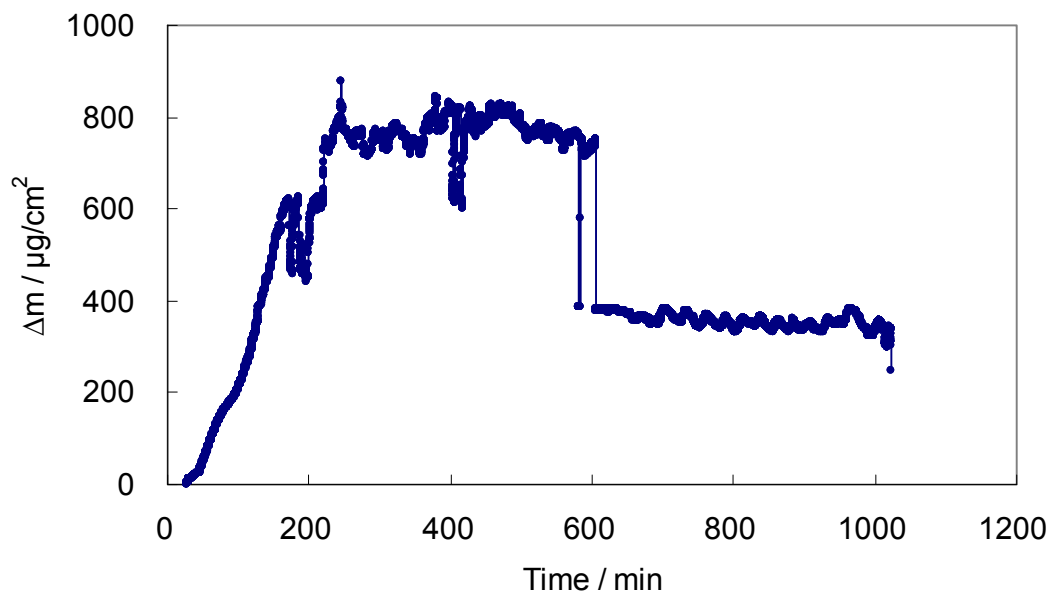


Figure 72. Iron carbonate precipitation on polarized (-1000 mV) gold coated quartz crystal surface at pH 6.6, initial SS=900, 80°C, 1 wt% NaCl solution.

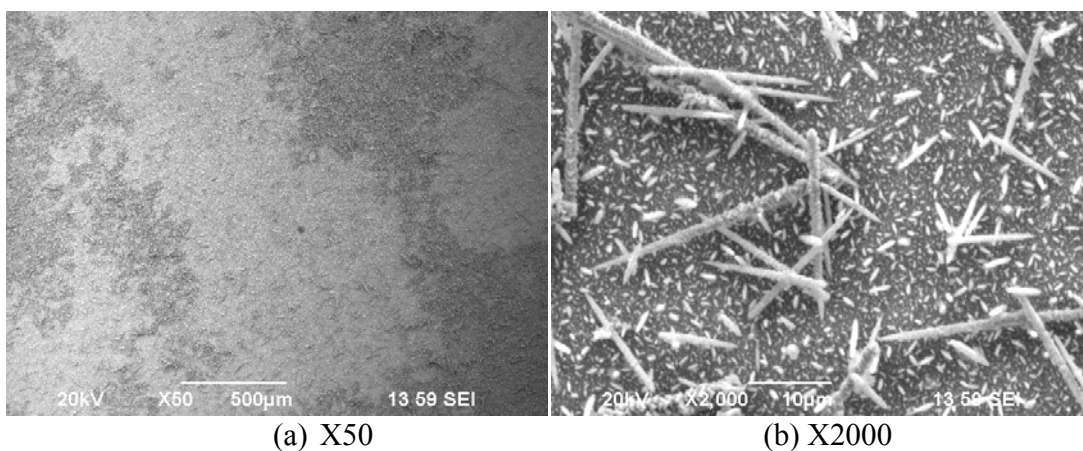


Figure 73. SEM analysis of specimen surface after layer formation on polarized (-1000 mV) gold coated quartz crystal at pH 6.6, initial SS=900, 80°C, 1 wt% NaCl solution.

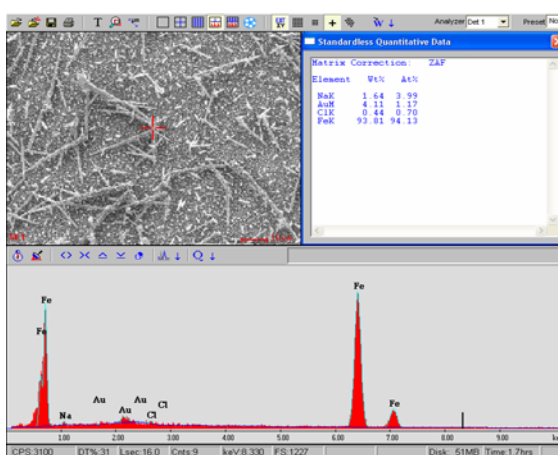


Figure 74. EDS analysis of the layer formed on a polarized (-1000 mV) gold coated quartz crystal surface at pH 6.6, initial SS=900, 80°C, 1 wt% NaCl solution.

Another test was done by polarizing the crystal at -700 mV vs. Ag/AgCl to simulate the corrosion potential normally observed on carbon steel in a CO<sub>2</sub> corrosion environment. It was shown in Figure 75 that the mass monitored by EQCM increased after the additional ferrous ion source was added to the solution at the beginning of the test. This was due to the iron carbonate precipitation on the gold coated crystal surface.

As the ferrous ion was consumed when precipitation proceeded, the supersaturation regarding iron carbonate decreased so the mass increase slowed down gradually.

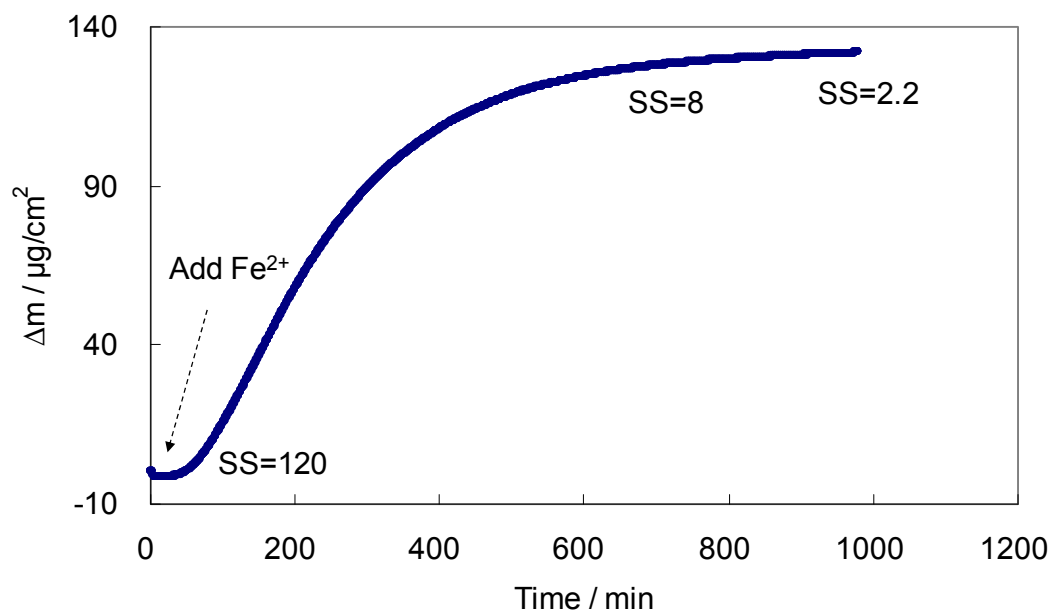


Figure 75. Iron carbonate precipitation on polarized (-700 mV) gold coated quartz crystal surface at pH 6.6, initial SS=120, 80°C, 1 wt% NaCl solution.

The SEM and EDS analysis of the surface after the test were shown in Figure 76 and Figure 77. The  $\text{FeCO}_3$  film was more uniformly distributed on the surface, but still not as dense as on the carbon steel surface.

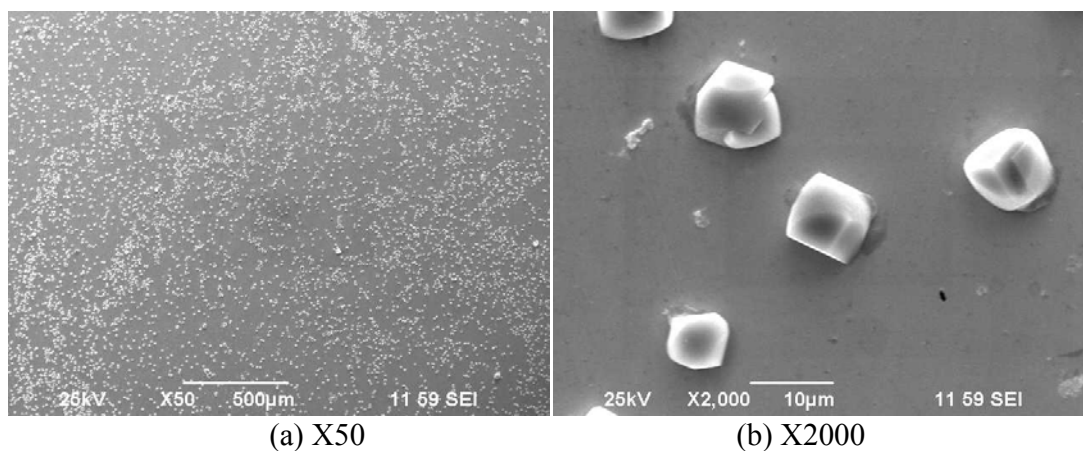


Figure 76. SEM analysis of the iron carbonate layer formed on a polarized gold coated quartz crystal at pH 6.6, initial SS=120, 80°C, 1 wt% NaCl solution.

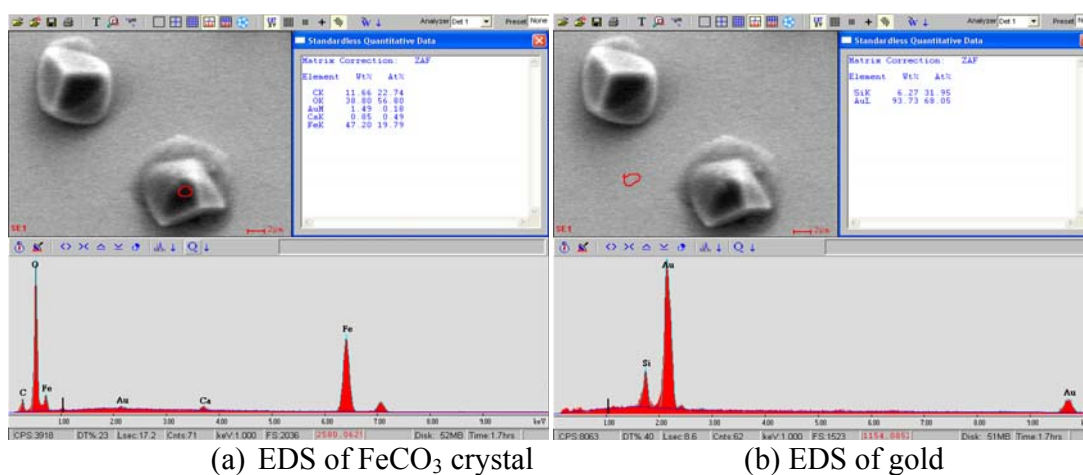


Figure 77. EDS analysis of iron carbonate layer formed on polarized gold coated quartz crystal surface at pH 6.6, initial SS=120, 80°C, 1 wt% NaCl solution.

In order to get a better coverage by the iron carbonate layer, a much higher initial supersaturation was used in the subsequent test. Figure 78 shows the mass change curve and Figure 79 shows the SEM pictures of the quartz crystal surface. A denser layer was obtained, but it was believed that this could still be improved.

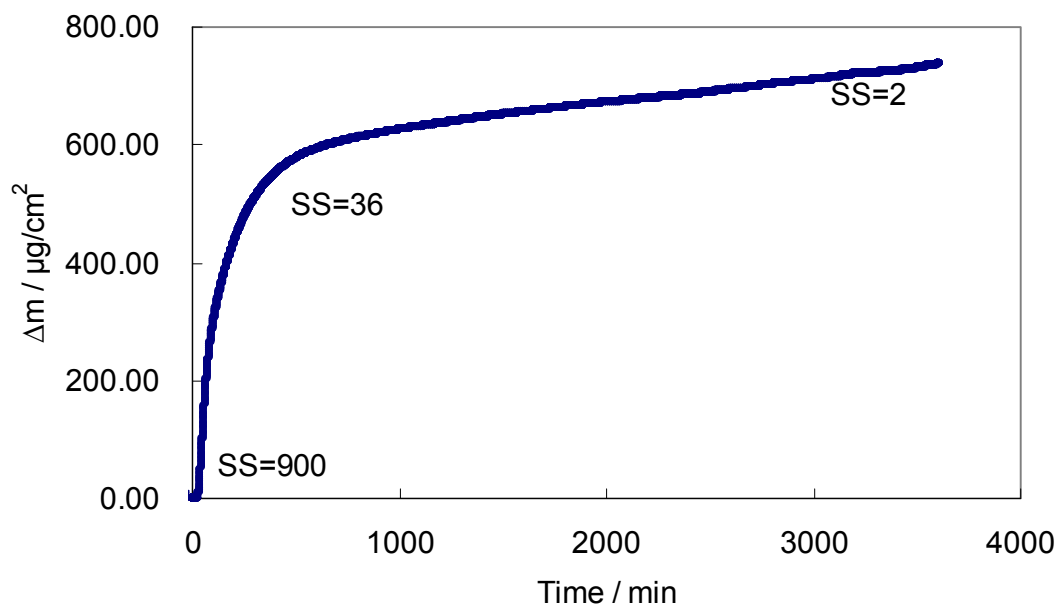


Figure 78. Iron carbonate precipitation on a polarized (-700 mV) gold coated quartz crystal surface at pH 6.6, initial SS=900, 80°C, 1 wt% NaCl solution.

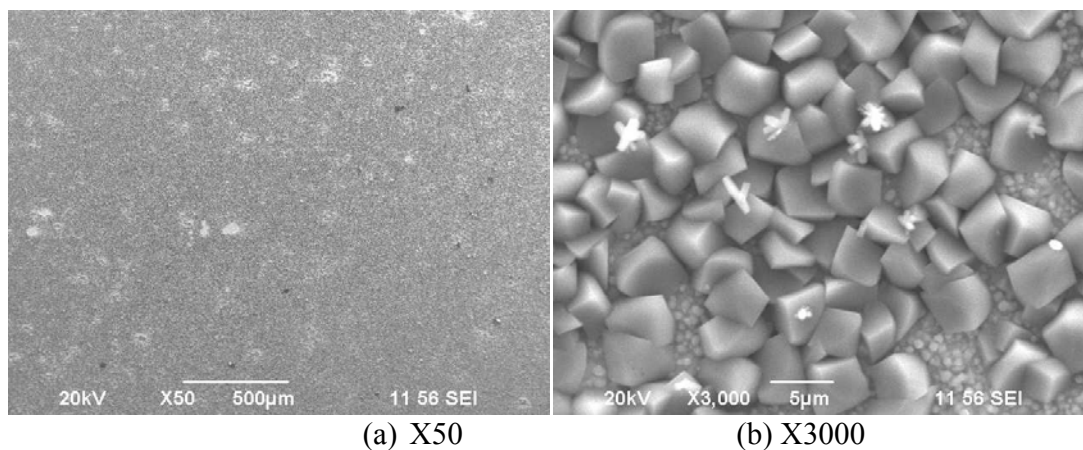


Figure 79. SEM analysis of an iron carbonate film formed on a polarized gold coated quartz crystal at pH 6.6, initial SS=900, 80°C, 1 wt% NaCl solution.

#### 5.4.3.2.2 Iron carbonate layer dissolution on a gold coated quartz crystal

Figure 80 shows an iron carbonate layer formation and dissolution test done with gold coated quartz crystal. There was a mass increase when the layer was formed on the

crystal surface due to the high initial supersaturation. After the mass increase stopped at a certain level, a jet flow with 1.3 m/s was started. It was noticed that there was no significant change in mass after the flow was started, which indicated that there was no effect on the layer from the jet flow. Then the solution pH was adjusted to 5.5, which created an undersaturated condition with respect to iron carbonate. The mass began decreasing immediately due to the dissolution of the iron carbonate. The slope of mass loss decreased as time passed, because the  $\text{Fe}^{2+}$  concentration increased as the iron carbonate layer dissolved, which thereby increased the saturation level of iron carbonate. Then the pH of the solution was adjusted again to a lower value, pH 5. Due to the decrease of the pH, there was less carbonate available in the solution and the solution became undersaturated again. In a similar fashion, the mass monitored by EQCM decreased and gradually became stable.

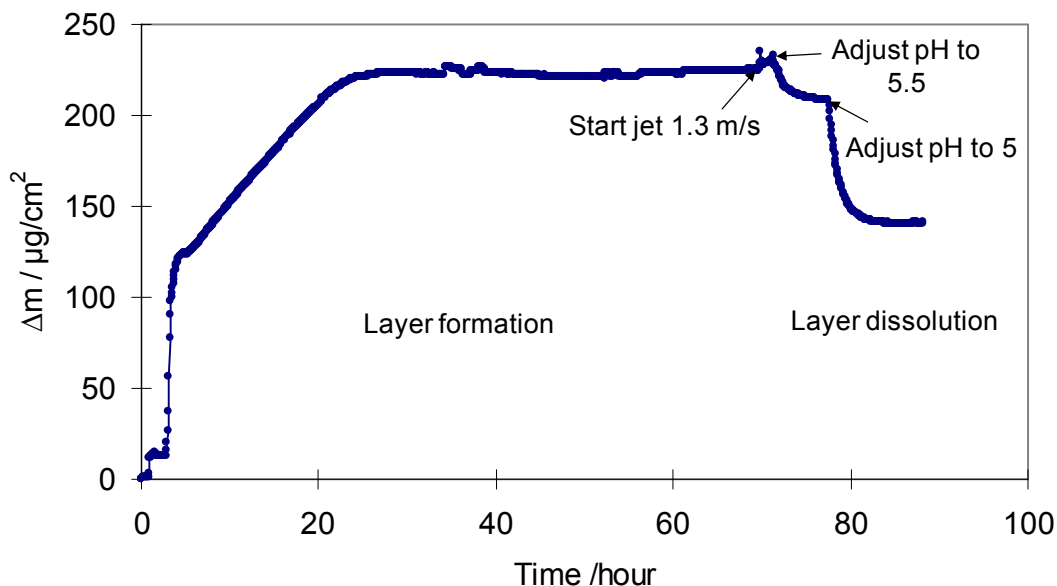


Figure 80. Mass change of the gold crystal monitored by EQCM in film formation and dissolution test under jet impingement, jet velocity 1.3 m/s, pH 6.6, initial SS=300, dissolution pH 5.5 and pH 5.0, 80°C, 1 wt% NaCl.

In this preliminary test, it was noted that the merit of this experiment done with the gold coated quartz crystal was that the mass change measured during the test was only due to the deposition of iron carbonate with no interference from other sources. This preliminary test showed that using EQCM with a gold coated quartz crystal could be a very useful method to study the iron carbonate layer formation and dissolution, while the layer formation could still be improved.

#### 5.4.4 Iron carbonate layer formation and dissolution on a platinum coated quartz crystal

It was thought that platinum coated quartz crystal can provide even better results. It was used to study iron carbonate layer formation and dissolution, since platinum is a noble metal and it also is well-known as a good catalyst, which could be helpful in iron carbonate formation.

#### 5.4.4.1 Experimental method

##### 5.4.4.1.1 Test setup

The same glass cell setup with EQCM and jet impingement was used as shown in Figure 63. Unpolished platinum crystal was used in the tests.

##### 5.4.4.1.2 Test matrix

The test matrix of iron carbonate layer formation and dissolution on platinum coated quartz crystal is shown in Table 15.

Table 15. Test matrix for the iron carbonate layer formation and dissolution on a platinum coated quartz crystal.

Parameter	Layer formation	Layer dissolution
Material	Unpolished platinum coated quartz crystal	
Solution	1 wt% NaCl	
CO <sub>2</sub> partial pressure	0.52 bar	
Temperature	80°C	
pH	6.6	5.0 to 6.0
Initial S of FeCO <sub>3</sub>	300	<0.1

##### 5.4.4.1.3 Test procedure

Before conducting any tests with the EQCM, platinum quartz crystals were initially cleaned by acetone in an ultrasonic bath. Deionized water and isopropyl alcohol were then used to further clean the crystal surface. The crystal was installed in the EQCM holder and put into a two liter glass cell with 0.5 M H<sub>2</sub>SO<sub>4</sub> solution purged with N<sub>2</sub>. The

potentiostat was used to polarize the platinum crystal at -1.2 V for 5 minutes to clean and activate the electrode. The crystal was then removed from the H<sub>2</sub>SO<sub>4</sub> solution and rinsed with deionized water. Another glass cell with two liters of 1 wt% NaCl solution was prepared and deoxygenated with CO<sub>2</sub> for 2 hours. This solution was heated to 80°C. Once the temperature was stable, the pH of the solution was adjusted to 6.6 by addition of NaHCO<sub>3</sub>. The EQCM probe with the cleaned platinum quartz crystal was inserted into the solution and polarized at -700 mV for 30 minutes. Additional Fe<sup>2+</sup> ions were added to the solution before or after the immersion of the platinum sample to create an iron carbonate supersaturation value of 300 to accelerate iron carbonate layer precipitation. This resulted in two different morphologies of iron carbonate that will be discussed later. The Fe<sup>2+</sup> concentration and pH of the solution were monitored during layer formation. After 24 hours or when the mass change on the EQCM stabilized, the layer formation was considered to be complete. A jet flow was started to create a well defined flow condition on the specimen surface. The solution pH was then adjusted by adding deoxygenated diluted HCl solution to reach an undersaturated condition in order to study iron carbonate dissolution. During the dissolution process, the solution pH and ferrous ion concentration were monitored regularly. The solution pH was adjusted as often as necessary. The test was considered to be finished when the mass became stable.

#### 5.4.4.2 Results and discussion

##### 5.4.4.2.1 Iron carbonate layer formation

Before conducting a dissolution test, a layer formation test was done to confirm that a realistic iron carbonate layer could be built on platinum crystal. The SEM image of

the unpolished platinum crystal surface is shown in Figure 81. The rough surface was favorable for nucleation of iron carbonate. Figure 82 shows a layer formation experiment monitored by EQCM with a platinum coated quartz crystal. The quartz crystal was polarized at -700 mV in advance to simulate the potential of a carbon steel specimen under the same condition. After being polarized for 30 minutes, additional ferrous ions were added to the solution to achieve a high supersaturated condition regarding iron carbonate. A  $1340 \mu\text{g}/\text{cm}^2$  increase in mass was observed due to the precipitation of iron carbonate on the surface over 24 hours. Simultaneously, the saturation level also decreased due to the consumption of the ferrous ions by precipitation. SEM images were taken after the layer formation on the specimen surface, in order to check the morphology of the layer, as shown in Figure 83. It can be seen from the image that a very compact layer of iron carbonate was formed on the surface, mainly composed of prism shaped iron carbonate.

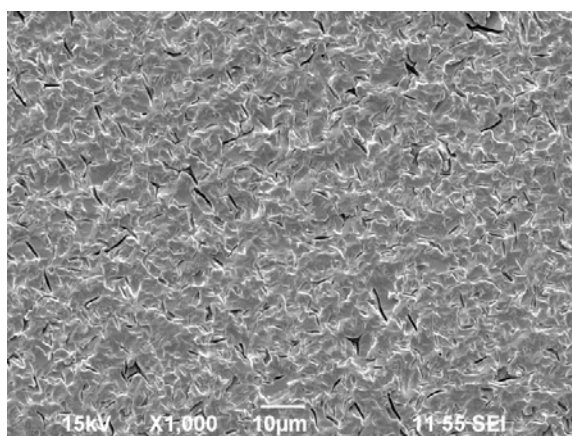


Figure 81. Blank surface of unpolished platinum coated quartz crystal at X1000.

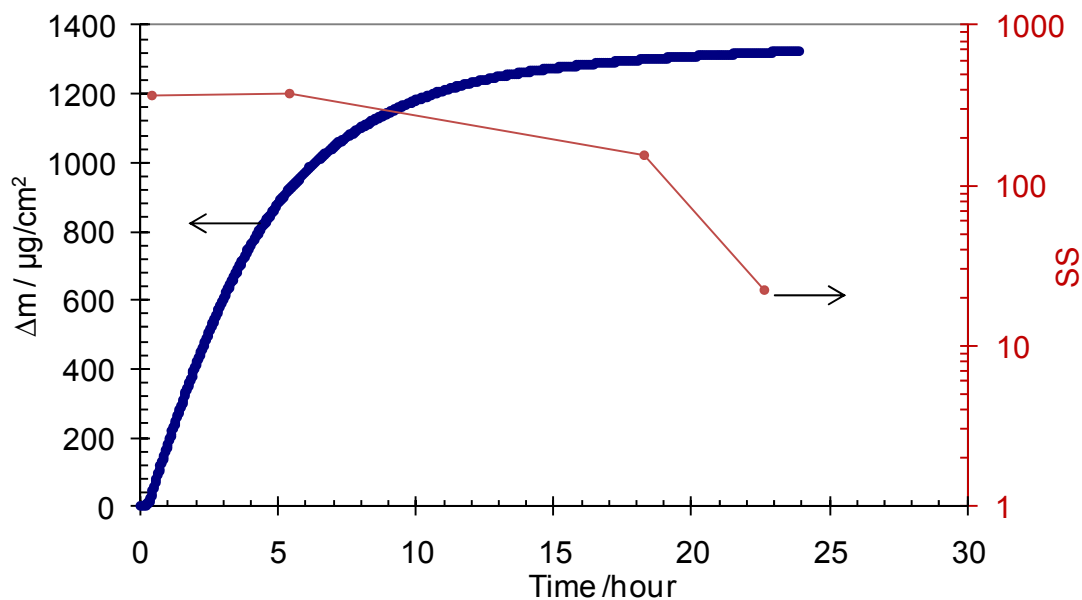


Figure 82. Mass change of platinum quartz crystal monitored by EQCM during prism shaped iron carbonate layer formation test, pH 6.6, initial SS=300, 80°C, polarized at -700 mV, 1 wt% NaCl, stagnant. Polarization was started before additional ferrous ion was added to the solution.

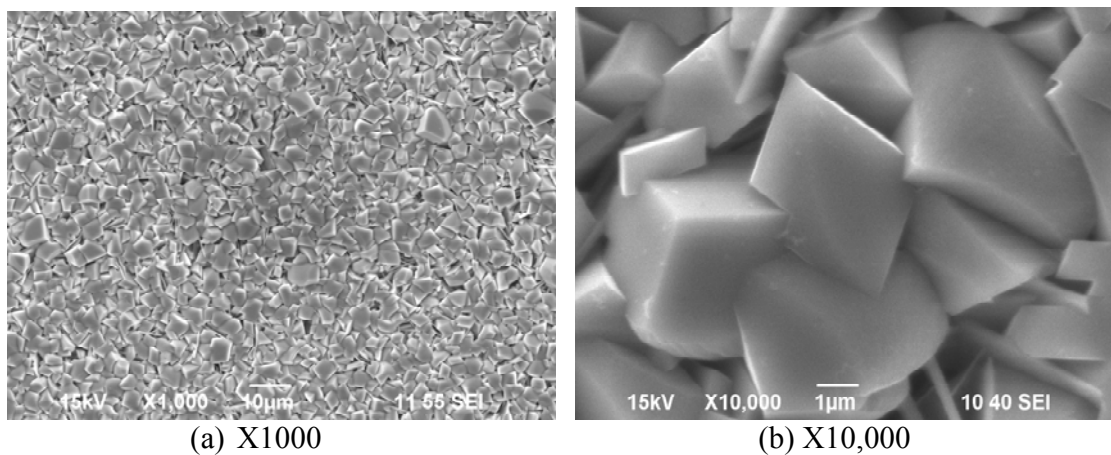


Figure 83. SEM images of specimen surface after prism shaped iron carbonate layer formation on platinum quartz crystal, pH 6.6, initial SS=300, 80°C, polarized at -700 mV, 1 wt% NaCl, stagnant. Polarization was started before additional ferrous ion was added to the solution.

Iron carbonate was also formed with a slightly different test procedure, in which the additional  $\text{Fe}^{2+}$  ions were added to the solution before the immersion of the platinum coated crystal in the test solution. A mass change curve during layer formation following this test procedure is shown in Figure 84. The mass increased due to the precipitation of iron carbonate on the surface. A jet flow at 1.3 m/s was started when the mass became stabilized. There was no significant effect of jet flow on mass observed during the test as shown in Figure 84.

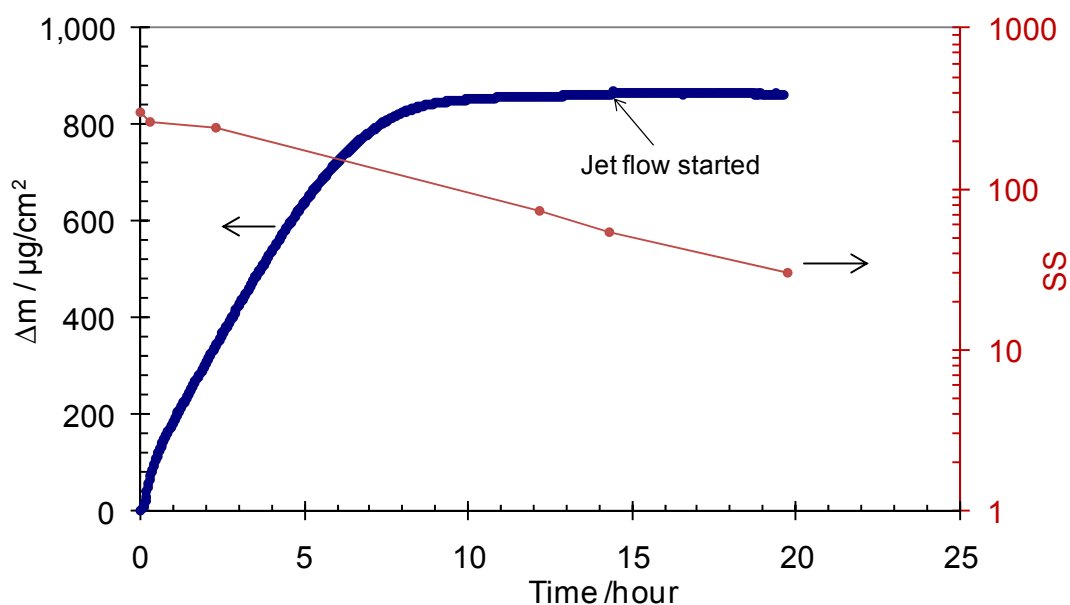


Figure 84. Mass change of platinum-coated quartz crystal monitored by EQCM for plate shaped iron carbonate layer formation test, pH 6.6, initial SS=300, polarized at -700 mV, 80°C, 1 wt% NaCl. Polarization was started after additional ferrous ion was added to the solution.

Figure 85 shows the SEM images of the layer after the test was finished. As seen in there, most of the iron carbonate which formed during the test was plate shaped iron

carbonate crystal. The composition of this plate shaped iron carbonate was confirmed by Fajardo (2011) using Raman spectroscopy and X-ray photoelectron spectroscopy (XPS) analysis.

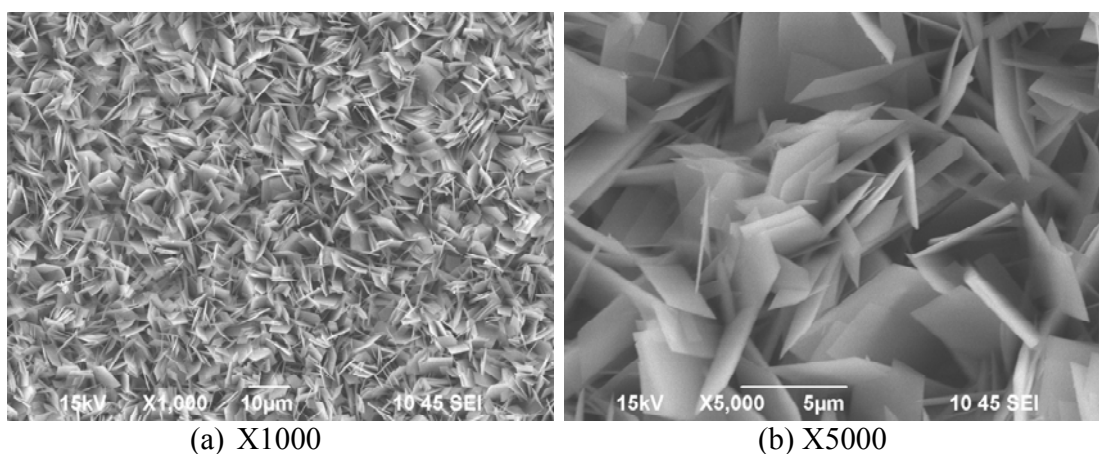


Figure 85. SEM images of specimen surface after plate shaped iron carbonate layer formation on platinum coated quartz crystal, pH 6.6, initial SS=300, polarized at -700 mV, 80°C, 1 wt% NaCl. Polarization was started after additional ferrous ion was added to the solution.

The different morphology observed in the tests was attributed to the change of test procedure. When prism shaped iron carbonate was obtained, platinum had been polarized for 30 minutes before ferrous ions were added to the solution. This enabled the pH of the surface to be stabilized and similar to that of carbon steel. However, when the additional ferrous ions were added before polarization was started, the platinum surface underwent a sudden increase of pH which caused a very high supersaturation until the pH was stabilized. As introduced in Chapter 2, high supersaturation is favorable for homogeneous nucleation and therefore iron carbonate nucleated all over the surface and formed plate shaped iron carbonate crystal. In the other case, the supersaturation was not as high and

probably heterogeneous nucleation happened followed by prism shaped crystal growth on these nucleation sites. Although the hypothesis still needs to be further proven, the formation of the two types of iron carbonate enables dissolution study of the prism shaped and plate shaped iron carbonate separately.

#### 5.4.4.2.2 Iron carbonate layer dissolution

As a layer of prism shaped iron carbonate could be formed successfully on the platinum-coated quartz crystal surface, a dissolution test could now be conducted to study the mechanism of its dissolution.

Figure 86 shows the mass change monitored during a layer formation and dissolution test. Similar to the previous test shown in Figure 82, the mass increased initially due to the precipitation of iron carbonate. When the mass became stable, a jet flow at 1.3 m/s was started. The mass slightly fluctuated due to the change of the flow condition, but stabilized with time. The pH of the solution was then adjusted to the lower value to create an undersaturated condition with respect to iron carbonate. The dissolution rate of iron carbonate can be obtained by calculating the slope of the mass change curve. The saturation level of iron carbonate during the dissolution process was calculated based on the measurement of pH and ferrous ion concentration. It was noted that as the saturation level increased, the dissolution rate decreased, as expected.

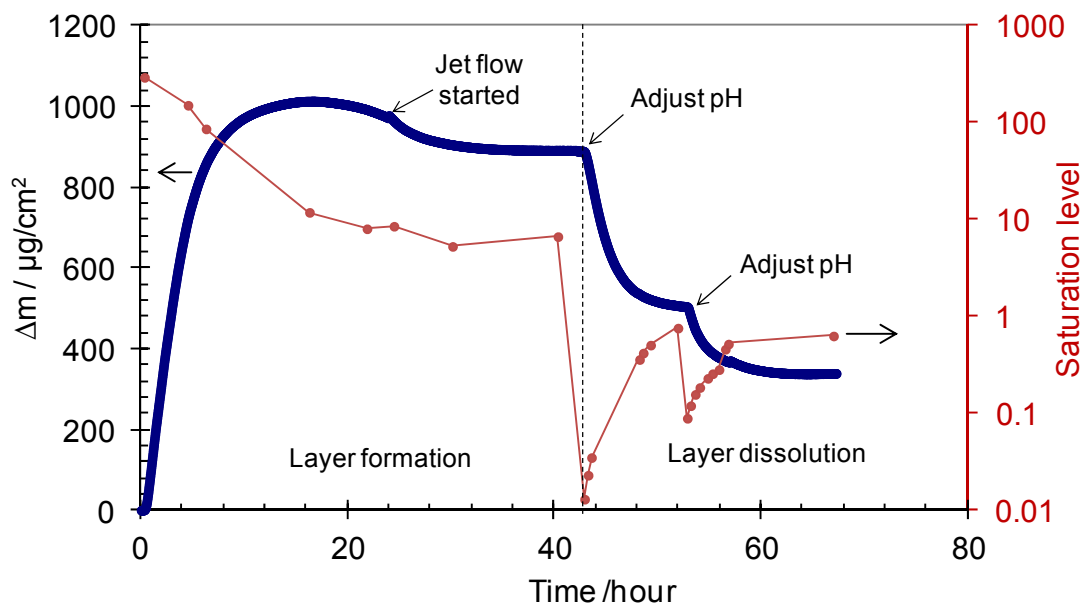


Figure 86. Mass change of the platinum quartz crystal monitored by EQCM in prism shaped iron carbonate layer formation and dissolution test, layer formation pH 6.6, initial SS=300, layer dissolution pH 5.0~5.5, 80°C, 1 wt% NaCl, jet flow rate 1.3 m/s.

Figure 87 shows the SEM and EDS images of the sample surface after the dissolution test. As can be seen in these images, most of the iron carbonate crystals were dissolved away and only some remnants of prisms remained on the specimen surface. Some platinum substrate was exposed due to iron carbonate layer dissolution.

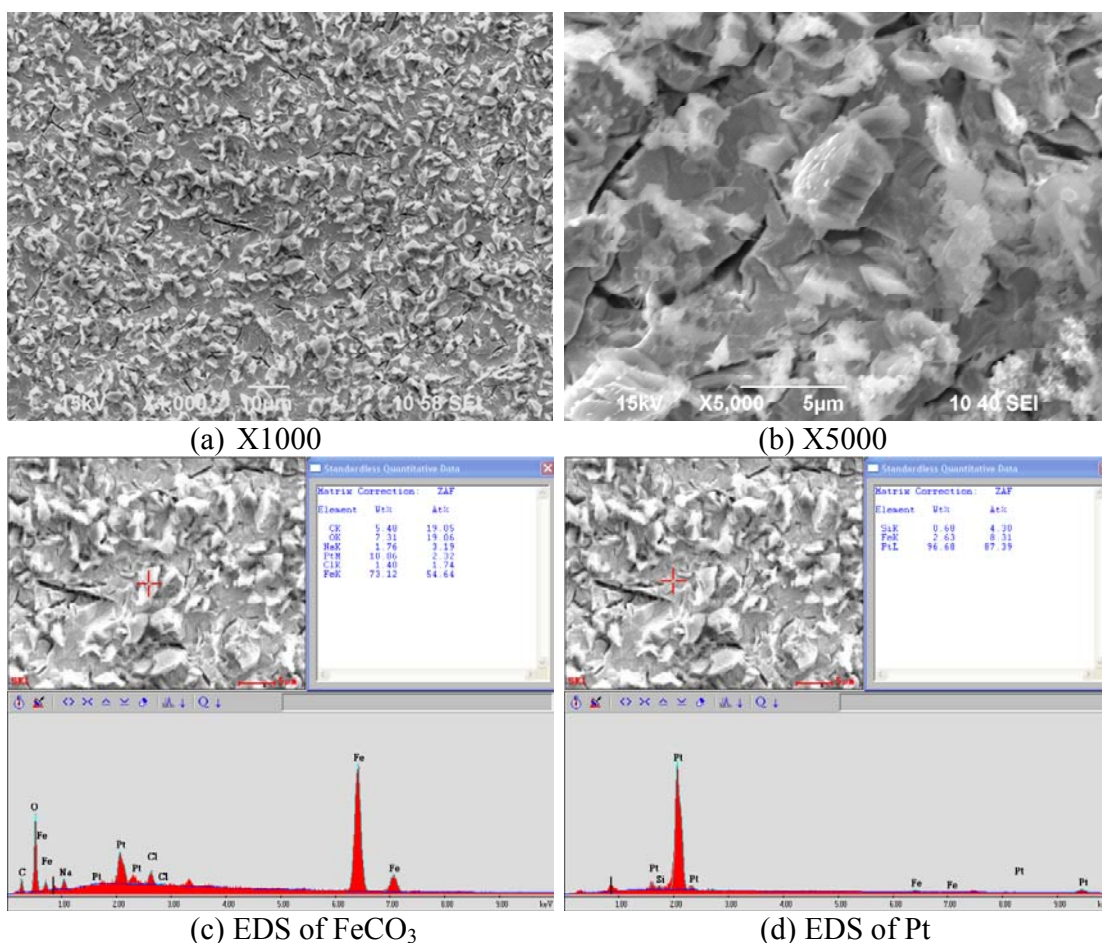


Figure 87. SEM and EDS images of the specimen surface after prism shaped iron carbonate formation and dissolution on platinum-coated quartz crystal, layer formation: pH 6.6, initial SS=300, layer dissolution: pH 5.0~5.5, 80°C, 1 wt% NaCl, jet flow rate 1.3 m/s.

Plate shaped iron carbonate was formed following the previously described test procedure and dissolution tests were conducted as shown in Figure 88. Following the formation of plate shaped iron carbonate layer, the solution pH was adjusted by adding HCl in order to create an undersaturated condition. The mass decreased immediately due to FeCO<sub>3</sub> dissolution. A jet flow was started during the dissolution process. There was no significant effect of the flow on the observed dissolution process. The mass decreased to

zero very fast and remained stable thereafter. Compared to the dissolution process of prism shaped iron carbonate, the dissolution rate appeared to be much higher for plate shaped iron carbonate.

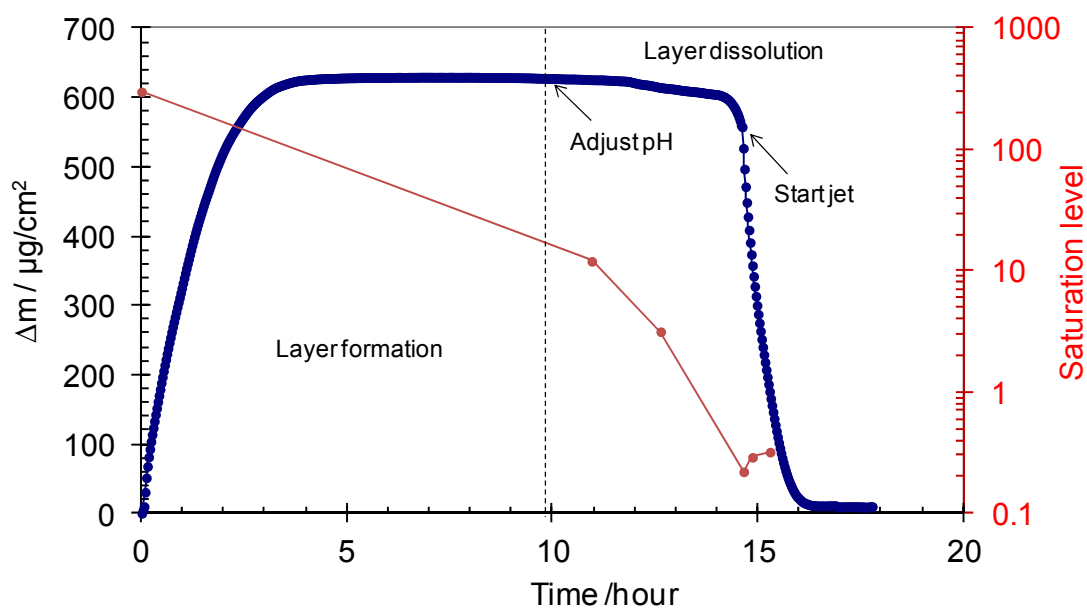


Figure 88. Mass change of the platinum-coated quartz crystal monitored by EQCM for plate shaped iron carbonate layer formation and dissolution test, layer formation pH 6.6, initial SS=300, film dissolution pH 5.0~5.5, 80°C, 1 wt% NaCl, jet flow rate 1.3 m/s.

### 5.5 Proposed mechanism of iron carbonate layer dissolution

Dissolution tests following the same procedure as described in section 5.4.4.1.3 were conducted several times and different jet flow velocity was also tested for prism shaped iron carbonate dissolution, in order to examine the effect of mass transfer on the dissolution process. For each test, the dissolution rate could be calculated by estimating the slope of the mass change curve. The obtained dissolution rate in all those tests was plotted versus saturation level in Figure 89.

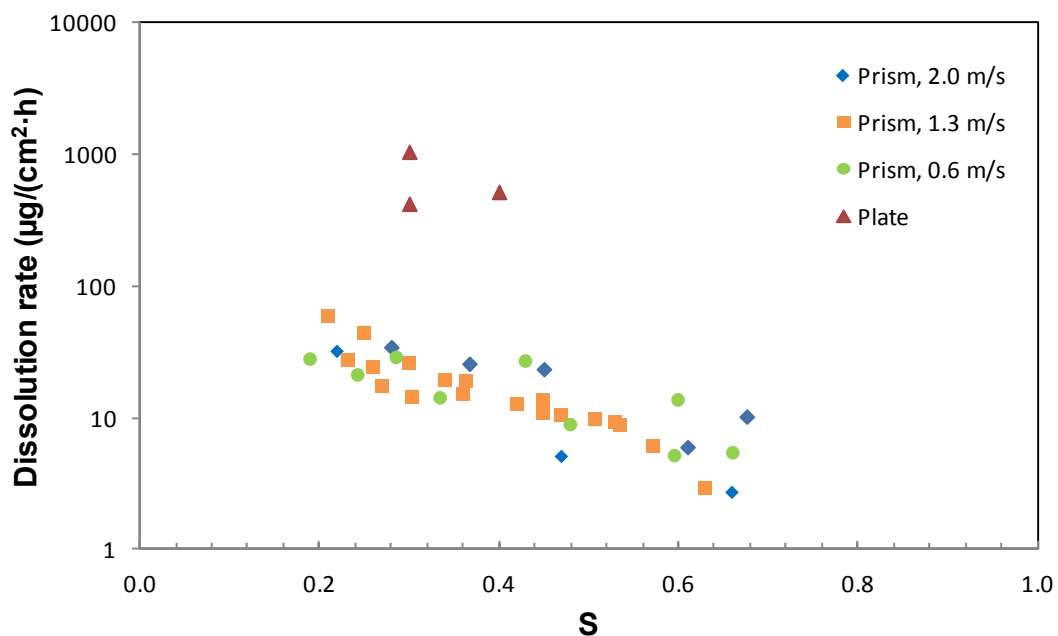
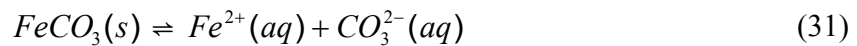
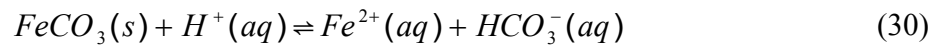


Figure 89. Dissolution rate change versus saturation level of iron carbonate as monitored by EQCM with platinum coated quartz crystal. Jet velocity for dissolution of prism shaped crystal was 2.0 m/s, 1.3 m/s and 0.6 m/s respectively. Jet velocity for dissolution of plate shaped crystal was 1.3 m/s.

From the plot it was shown that compared with the prism shaped iron carbonate, the dissolution rates of plate shaped iron carbonate were at least one order of magnitude higher. This was also in agreement with the observation in the qualitative study of iron carbonate dissolution by SEM, as reported in section 5.2. It was noticed that the change of jet velocity did not affect the dissolution rate significantly for prism shaped iron carbonate, which means that the dissolution process does not depend on the mass transfer rate. This is an indication of a surface reaction controlled process.

As introduced in Chapter 2, studies were made on iron carbonate dissolution kinetics in the geological field using siderite. Dissolution of siderite was proposed to

proceed through two parallel reactions (Pokrovsky & Schott, 2002; Duckworth & Martin, 2004a,b; Testemale, et al., 2009):



When the solution is far from equilibrium ( $S \ll 1$ ), the overall dissolution rate can be described by:

$$r = k_{f1}c_{H^+}^n + k_{f2} \quad (32)$$

where  $r$  is the overall reaction rate of iron carbonate dissolution,  $k_{f1}$  and  $k_{f2}$  are the forward reaction rate constants of reactions (30) and (31) respectively,  $n$  is the order of the reaction.  $c_{H^+}$  is the concentration of  $H^+$ .

When the solution pH was higher, Equation (32) could not be used to characterize the dissolution process as the backward (precipitation) reactions must be considered. In this case, the overall reaction rate can be expressed as:

$$r = k_{f1}c_{H^+} - k_{b1}c_{Fe^{2+}}c_{HCO_3^-} + k_{f2} - k_{b2}c_{Fe^{2+}}c_{CO_3^{2-}} \quad (33)$$

where  $k_{b1}$  and  $k_{b2}$  are the backward reaction rate constants of reactions (30) and (31) respectively.  $c_{Fe^{2+}}$ ,  $c_{HCO_3^-}$  and  $c_{CO_3^{2-}}$  are the concentrations of  $Fe^{2+}$ ,  $HCO_3^-$  and  $CO_3^{2-}$ .

It was pointed out that when pH was above 5.0, dissolution of iron carbonate is not pH-dependant (Pokrovsky & Schott, 2002) and dissolution of iron carbonate was dominated by reaction (31). The current study was done at a medium pH level (5.0 to 6.0) at 80°C, the contribution from the backward reaction of reaction (31) also became

significant. Therefore, only reaction (31) was considered further when characterizing iron carbonate dissolution kinetics. So, the dissolution rate can be expressed as:

$$r = k_{f2} - k_{b2}c_{Fe^{2+}}c_{CO_3^{2-}} \quad (34)$$

After transformation, Equation (33) can be written as:

$$r = k_{f2}(1 - S) \quad (35)$$

$$\log(r) = \log(k_{f2}) + \log(1 - S) \quad (36)$$

Therefore, the parameters of the dissolution kinetics expression can be obtained by fitting the slope and intercept of the line ( $\log(r) \sim \log(1-S)$ ). As shown in Figure 90, the parameters in Equation (36) can be obtained by linear regression. The dissolution kinetics expression for prism shaped iron carbonate appeared to be:

$$r = (0.0045 \pm 0.0014)(1 - S)^{(2.3 \pm 0.5)} \quad (37)$$

where the unit of  $r$  is  $\text{mol} \cdot \text{m}^{-2} \cdot \text{h}^{-1}$ , and the unit of  $k_{f2}$  is also  $\text{mol} \cdot \text{mol}^{-2} \cdot \text{h}^{-1}$ .

The order of reaction is approximately 2, which does not strictly follow either of the theoretical mechanisms presented above (30) and (31). This is rather common and suggests a more complex pathway for iron carbonate dissolution. For the same reasons, the rates presented by Equation (37) are not directly comparable to the ones given in Table 1, even if this should be possible in a purely theoretical sense.

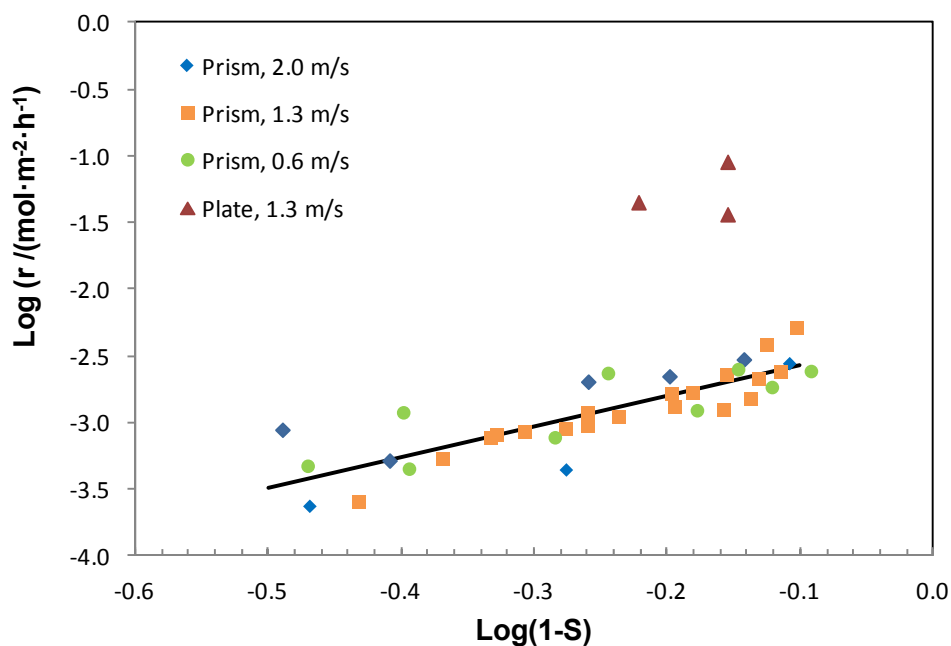


Figure 90. Dissolution rate change versus saturation level of iron carbonate as monitored by EQCM with platinum coated quartz crystal.

The rates obtained using Equation (37) are one to two orders higher compared to the ones observed in the studies related to the geological field (Duckworth & Martin, 2004b; Golubev, et al., 2009; Pokrovsky & Schott, 2002; Tang & Martin, 2011; Testemale, et al., 2009), which could be explained by the different origin of iron carbonate as well as the differences in the experimental conditions (saturation level, temperature, and etc.).

However, due to the limited dissolution rate data of plate shaped iron carbonate, it would not be realistic to develop a model for plate shaped iron carbonate in this project. Furthermore, it is thought that this morphology is transitional in nature and therefore is of less practical importance.

## 5.6 Summary

In this Chapter, the dissolution behavior of iron carbonate was studied. Qualitative tests conducted using SEM showed that the iron carbonate layer would be dissolved when exposed to an undersaturated condition. The dissolution rate was faster at lower pH as expected. In addition, it was also observed that plate shaped iron carbonate dissolve preferably compared to prism shaped iron carbonate crystals.

Quantitative tests were conducted in order to quantify the dissolution process of iron carbonate. Different experimental configurations were employed. With rotating cylinder electrode setup, it was detected that protective layer of iron carbonate formed on steel surface could be damaged by dissolution and the corrosion rate increased as a result. With the direct measurement of mass change using EQCM, the dissolution rate of iron carbonate could be quantified directly. Dissolution tests were conducted with iron, gold and platinum coated quartz crystals. A mechanism of iron carbonate dissolution was proposed and the kinetics expression was obtained.

## CHAPTER 6: CONCLUSIONS AND FUTURE WORK

### 6.1 Conclusions

In this dissertation, the removal mechanisms of the protective iron carbonate layer in a single phase flow were studied. Two proposed mechanisms were investigated, using various experimental configurations. The key findings of the current work are summarized below.

- In the small scale experiments, no effect of hydrodynamic force was detected on the protectiveness of iron carbonate layer, with both rotating cylinder electrode setup and jet impingement setup.
- Mechanical effect of flow on the protective iron carbonate layer was also tested in a medium scale flow loop (thin channel flow cell system) under a realistic flow condition. The experimental results further confirmed that the protective layer cannot be damaged mechanically by hydrodynamic forces only.
- When carbon steel covered with a protective iron carbonate layer was exposed to intense turbulent flow, a thin yet adherent layer remained on the steel surface which provided protection to steel against corrosion.
- The adhesion strength between a protective iron carbonate layer and the steel substrate is of the order of  $10^6$  Pa.
- The protective iron carbonate layer cannot be removed by hydrodynamic forces of the flow alone.

- Chemical dissolution of the iron carbonate layer leads to exposure of the underlying steel substrate and an increase of the corrosion rate.
- Plate shaped iron carbonate is dissolved preferably compared with prism shaped iron carbonate.
- Iron carbonate dissolution studied by using the EQCM indicates a surface reaction controlled process mechanism.
- Iron carbonate dissolution kinetics was successfully quantified.

## **6.2 Recommendations for future work**

- Determine the effect of variation in the environmental factors, such as temperature, pH and CO<sub>2</sub> partial pressure, on the mechanical properties of protective iron carbonate layer.
- Investigate of the effect of steel composition and microstructure on the characteristics of the corrosion product layer.
- Further characterize the two morphologies of iron carbonate. Define the conditions favorable for the formation of each type of iron carbonate. Understand the role of each type of iron carbonate in the protectiveness of the layer.
- Further investigate the dissolution mechanism of two morphologies of iron carbonate.
- Investigate the spontaneous passivation behavior of carbon steel in CO<sub>2</sub> corrosion environment.

## REFERENCES

- Abduh, M. (2008). The 50 Major Engineering Failures <http://abduh137.wordpress.com/2008/04/25/the-50-major-engineering-failures-1977-2007-part-1/>
- Benezeth, P., Dandurand, J. L., & Harrichoury, J. C. (2009). Solubility product of siderite ( $\text{FeCO}_3$ ) as a function of temperature (25-250 °C). *Chemical Geology*, 265(1-2), 3-12.
- Berntsen, T., Seiersten, M., & Hemmingsen, T. (2011). *Effect of  $\text{FeCO}_3$  supersaturation and carbide exposure on the  $\text{CO}_2$  corrosion rate of carbon steel*. Paper presented at the NACE Corrosion/11, paper no. 11072.
- Bockris, J. O. M., Drazic, D., & Despic, A. R. (1961). The electrode kinetics of the deposition and dissolution of iron. *Electrochimica Acta*, 4, 325.
- Bonis, M. R., & Crolet, J. L. (1989). *Basics of the prediction of the risks of  $\text{CO}_2$  corrosion in oil and gas wells*. Paper presented at the NACE Corrosion/89, paper no. 466.
- Chokshi, K., Sun, W., & Nescic, S. (2005). *Iron carbonate film growth and the effect of inhibition in  $\text{CO}_2$  corrosion of mild steel*. Paper presented at the NACE Corrosion/05, paper no. 285.
- Crolet, J. L., Olsen, S., & Wilhelmsen, W. (1994). *Influence of a layer of undissolved cementite on the rate of the  $\text{CO}_2$  corrosion of carbon steel*. Paper presented at the NACE Corrosion/94, paper no. 4.

- Crolet, J. L., Thevenot, N., & Nestic, S. (1998). Role of conductive corrosion products in the protectiveness of corrosion layers. *Corrosion*, 54(3), 194-203.
- Dawson, J. L., & Shih, C. C. (1987). *Electrochemical testing of flow-accelerated corrosion using jet impingement rigs*. Paper presented at the NACE Corrosion/87, paper no. 453.
- de Moraes, F. D., Shadley, J. R., Chen, J., & Rybicki, E. F. (2000). *Characterization of CO<sub>2</sub> corrosion product scales related to environmental conditions*. Paper presented at the NACE Corrosion/2000, paper no. 30.
- de Waard, C., & Lotz, U. (1993). *Prediction of CO<sub>2</sub> corrosion of carbon steel*. Paper presented at the NACE Corrosion/93, paper no. 93069.
- de Waard, C., Lotz, U., & Dugstad, A. (1995). *Influence of liquid flow velocity on CO<sub>2</sub> corrosion: a semi-empirical model*. Paper presented at the NACE Corrosion/95, paper no. 95128.
- de Waard, C., & Milliams, D. E. (1975a). Carbonic acid corrosion of steel. *Corrosion*, 31, 177-181.
- de Waard, C., & Milliams, D. E. (1975b). *Prediction of carbonic acid corrosion in natural gas pipelines*. Paper presented at the First International Conference on the Internal and External Protection of Pipes, paper no. F1.
- Dresel, P. E. (1989). *The dissolution kinetics of siderite and its effect on acid mine drainage*. Doctoral Dissertation, Pennsylvania State University.
- Duckworth, O. W., & Martin, S. T. (2004a). Dissolution rates and pit morphologies of rhombohedral carbonate minerals. *American Mineralogist*, 89(4), 554-563.

- Duckworth, O. W., & Martin, S. T. (2004b). Role of molecular oxygen in the dissolution of siderite and rhodochrosite. *Geochimica et Cosmochimica Acta*, 68(3), 607-621.
- Dugstad, A. (1992). *The importance of FeCO<sub>3</sub> supersaturation on the CO<sub>2</sub> corrosion of carbon steels*. Paper presented at the NACE Corrosion/92, paper no. 14.
- Dugstad, A. (2006). *Fundamental aspects of CO<sub>2</sub> metal loss corrosion - Part I: Mechanism*. Paper presented at the NACE Corrosion/06, paper no. 06111.
- Dugstad, A., Hemmer, H., & Siersten, M. (2001). Effect of steel microstructure on corrosion rate and protective iron carbonate film formation. *Corrosion*, 57(4), 369-378.
- Eisenberg, M., Tobias, C. W., & Wilke, C. R. (1954). Ionic mass transfer and concentration polarization at rotating electrodes. *Journal of The Electrochemical Society*, 101, 306-319.
- Fajardo, V. (2011). *Localized CO<sub>2</sub> corrosion in the presence of organic acids*. Master Thesis, Ohio University.
- Fang, H. (2006). *Low Temperature and High Salt Concentration effects on General CO<sub>2</sub> Corrosion for Carbon Steel*. Master Thesis, Ohio University.
- Gao, K., Yu, F., Pang, X., Zhang, G., Qiao, L., Chu, W., et al. (2008). Mechanical properties of CO<sub>2</sub> corrosion product scales and their relationship to corrosion rates. *Corrosion Science*, 50(10), 2796-2803.
- Gao, M., Pang, X., & Gao, K. (2011). The growth mechanism of CO<sub>2</sub> corrosion product films. *Corrosion Science*, 53(2), 557-568.

- Giralt, F., & Trass, O. (1975). Mass transfer from crystalline surfaces in a turbulent impinging jet - Part 1: Transfer by erosion. *The Canadian Journal of Chemical Engineering*, 53(5), 505-511.
- Giralt, F., & Trass, O. (1976). Mass transfer from crystalline surfaces in a turbulent impinging jet - Part 2: Erosion and diffusional transfer. *The Canadian Journal of Chemical Engineering*, 54(3), 148-155.
- Golubev, S. V., Bénézech, P., Schott, J., Dandurand, J. L., & Castillo, A. (2009). Siderite dissolution kinetics in acidic aqueous solutions from 25 to 100 °C and 0 to 50 atm pCO<sub>2</sub>. *Chemical Geology*, 265(1-2), 13-19.
- Gray, L. G. S., Anderson, B. G., Danysh, M. J., & Tremaine, P. R. (1989). *Mechanism of carbon steel corrosion in brines containing dissolved carbon dioxide at pH 4*. Paper presented at the NACE Corrosion/89, paper no.464.
- Gray, L. G. S., Anderson, B. G., Danysh, M. J., & Tremaine, P. R. (1990). *Effect of pH and temperature on the mechanism of carbon steel corrosion by aqueous carbon dioxide*. Paper presented at the NACE Corrosion/90, paper no. 90040.
- Greenberg, J., & Tomson, M. (1992). Precipitation and dissolution kinetics and equilibria of aqueous ferrous carbonate vs temperature. *Applied Geochemistry* 7, 185-190.
- Han, J., Brown, B., & Nesic, S. (2010). Investigation of the galvanic mechanism for localized carbon dioxide corrosion propagation using the artificial pit technique. *Corrosion*, 66(9), 1-12.

- Han, J., Nescic, S., Yang, Y., & Brown, B. (2011). Spontaneous passivation observations during scale formation on mild steel in CO<sub>2</sub> brines. *Electrochimica Acta*, 56(15), 5396-5404.
- Han, J., Yang, Y., Brown, B., & Nescic, S. (2007). *Electrochemical investigation of localized CO<sub>2</sub> corrosion on mild steel*. Paper presented at the NACE Corrosion/07, paper no. 07323.
- Han, J., Yang, Y., Brown, B., & Nescic, S. (2008). *Roles of passivation and galvanic effects in localized CO<sub>2</sub> corrosion of mild steel*. Paper presented at the NACE Corrosion/08, paper no. 08332.
- Hurlen, T., Gunvaldsen, S., Tunold, R., Blaker, F., & Lunde, P. G. (1984). Effects of carbon dioxide on reactions at iron electrodes in aqueous salt solutions. *Journal of Electroanalytical Chemistry*, 180, 511-526.
- Johnson, M. L., & Tomson, M. (1991). *Ferrous carbonate precipitation kinetics and its impact on CO<sub>2</sub> corrosion*. Paper presented at the NACE Corrosion/91, paper no. 2689.
- Kanazawa, K. K., & Gordon, J. G. (1985). Frequency of a quartz microbalance in contact with liquid. *Analytical Chemistry*, 57(8), 1770-1771.
- Kermani, M. B., & Morshed, A. (2003). Carbon dioxide corrosion in oil and gas production - A compendium. *Corrosion*, 59(8), 659-683.
- Lasaga, A. C. (1998). *Kinetic Theory in the Earth Sciences*. Princeton, NJ: Princeton University Press.

- Li, W. (2011). *Investigation of pseudo-passive layer formation in CO<sub>2</sub> corrosion*. Master Thesis, Ohio University.
- Morse, J. W. (1983). The kinetics of calcium carbonate dissolution and precipitation. *Reviews in Mineralogy and Geochemistry*, 11(1), 227-264.
- Morse, J. W., & Arvidson, R. S. (2002). The dissolution kinetics of major sedimentary carbonate minerals. *Earth-Science Reviews*, 58(1-2), 51-84.
- Nancollas, J. H. (1979). The growth of crystals in solution. *Advances in Colloid and Interfacial Science*, 10, 215-252.
- Nesic, S. (2007). Key issues related to modeling of internal corrosion of oil and gas pipelines-A review. *Corrosion Science*, 49, 4308-4338.
- Nesic, S., & Lee, J. (2003). A mechanistic model for carbon dioxide corrosion of mild steel in the presence of protective iron carbonate films - Part 3: Film growth model. *Corrosion*, 59(7), 616-628.
- Nesic, S., & Lunde, L. (1994). Carbon dioxide corrosion of carbon steel in two-phase flow. *Corrosion*, 50(9), 717-727.
- Nesic, S., & Postlethwaite, J. (1996). An electrochemical model for prediction of CO<sub>2</sub> corrosion. *Corrosion*, 52, 280-293.
- Nesic, S., Thevenot, N., Crolet, J. L., & Drazic, D. (1996). *Electrochemical properties of iron dissolution in the presence of CO<sub>2</sub>-basics revisited*. Paper presented at the NACE Corrosion/96, paper no. 96003.
- Nesic, S., Wang, S., Cai, J., & Xiao, Y. (2004). *Integrated CO<sub>2</sub> corrosion-multiphase flow model*. Paper presented at the NACE Corrosion/04, paper no. 04626.

- Nordsveen, M., Nestic, S., Nyborg, R., & Stangeland, A. (2003). A mechanistic model for carbon dioxide corrosion of mild steel in the presence of protective iron carbonate films - Part 1: Theory and verification. *Corrosion*, 59(5), 443-456.
- Nyborg, R. (2002). *Overview of CO<sub>2</sub> corrosion models for wells and pipelines*. Paper presented at the NACE Corrosion/02, paper no. 02233.
- Oddo, J. E., & Tomson, M. B. (1999). *The prediction of scale and CO<sub>2</sub> corrosion in oil field systems*. Paper presented at the NACE Corrosion/99, paper no. 41.
- Plummer, L. N., Parkhurst, D. L., & Wigley, T. M. L. (1979). Critical Review of the Kinetics of Calcite Dissolution and Precipitation *Chemical Modeling in Aqueous Systems* (Vol. 93, pp. 537-573): American Chemical Society.
- Pokrovsky, O. S., & Schott, J. (2002). Surface Chemistry and Dissolution Kinetics of Divalent Metal Carbonates. *Environmental Science & Technology*, 36(3), 426-432.
- Pots, B. F. M. (1995). *Mechanistic models for the prediction of CO<sub>2</sub> corrosion rates under multiphase flow conditions*. Paper presented at the NACE Corrosion/95, paper no. 95137.
- Remita, E., Tribollet, B., Sutter, E., Vivier, V., Ropital, F., & Kittel, J. (2008). Hydrogen evolution in aqueous solutions containing dissolved CO<sub>2</sub>: Quantitative contribution of the buffering effect. *Corrosion Science*, 50(5), 1433-1440.
- Ruzic, V., Veidt, M., & Nestic, S. (2006a). Protective iron carbonate films - Part 1: Mechanical removal in single-phase aqueous flow. *Corrosion*, 62(5), 419-432.

- Ruzic, V., Veidt, M., & Nestic, S. (2006b). Protective iron carbonate films - Part 2: Chemical removal by dissolution in single-phase aqueous flow. *Corrosion*, 62(7), 598-611.
- Sauerbrey, G. (1959). Verwendung von Schwingquarzen zur Wägung dünner Schichten und Microwägung. *Z. Phys.*, 155, 206.
- Schmitt, G., Gudde, T., & Strobel-Effertz, E. (1996). *Fracture mechanical properties of CO<sub>2</sub> corrosion product scales and their relation to localized corrosion*. Paper presented at the NACE Corrosion/96, paper no.9.
- Schmitt, G., & Horstemeier, M. (2006). *Fundamental aspects of CO<sub>2</sub> metal loss corrosion - Part II: Influence of different parameters on CO<sub>2</sub> corrosion mechanisms*. Paper presented at the NACE Corrosion/06, paper no. 06112.
- Schmitt, G., & Mueller, M. (1999). *Critical wall shear stresses in CO<sub>2</sub> corrosion of carbon steel*. Paper presented at the NACE Corrosion/99, paper no. 44.
- Schmitt, G., Mueller, M., & Strobel-Effertz, E. (1999). *Understanding localized CO<sub>2</sub> corrosion of carbon steel from physical properties of iron carbonate scales*. Paper presented at the NACE Corrosion/99, paper no. 38.
- Schmitt, G., & Rothmann, B. (1978a). Studies on the corrosion mechanism of unalloyed steel in oxygen-free carbon dioxide solutions, Part 1: Kinetics of the liberation of hydrogen. *Werkstoffe Und Korrosion*, 28, 154-162.
- Schmitt, G., & Rothmann, B. (1978b). Studies on the corrosion mechanism of unalloyed steel in oxygen-free carbon dioxide solutions, Part 2: Kinetics of iron dissolution. *Werkstoffe Und Korrosion*, 29, 153-166.

- Sun, W. (2006). *Kinetics of iron carbonate and iron sulfide scale formation in CO<sub>2</sub>/H<sub>2</sub>S corrosion*. Doctoral Dissertation, Ohio University.
- Sun, W., & Netic, S. (2008). Kinetics of corrosion layer formation: Part 1 - Iron carbonate layers in carbon dioxide corrosion. *Corrosion*, 64(4), 334-346.
- Sun, W., Netic, S., & Woollam, R. C. (2009). The effect of temperature and ionic strength on iron carbonate (FeCO<sub>3</sub>) solubility limit. *Corrosion Science*, 51(6), 1273-1276.
- Tang, Y., & Martin, S. T. (2011). Siderite dissolution in the presence of chromate. *Geochimica et Cosmochimica Acta*, 75(17), 4951-4962.
- Testemale, D., Dufaud, F., Martinez, I., Benezeth, P., Hazemann, J.-L., Schott, J., et al. (2009). An X-ray absorption study of the dissolution of siderite at 300 bar between 50 °C and 100 °C. *Chemical Geology*, 259(1-2), 8-16.
- van Cappellen, P., Charlet, L., Stumm, W., & Wersin, P. (1993). A surface complexation model of the carbonate mineral-aqueous solution interface. *Geochimica et Cosmochimica Acta*, 57(15), 3505-3518.
- van Hunnik, E. W. J., Pots, B. F. M., & Hendriksen, E. L. J. A. (1996). *The formation of protective FeCO<sub>3</sub> corrosion product layers in CO<sub>2</sub> corrosion*. Paper presented at the NACE Corrosion/96, paper no. 6.
- Videm, K., & Dugstad, A. (1989a). Corrosion of carbon steel in an aqueous carbon dioxide environment - Part 1: Solution effects. *Materials Performance*, 28(3), 63-67.

- Videm, K., & Dugstad, A. (1989b). Corrosion of carbon steel in an aqueous carbon dioxide environment - Part 2: Film formation. *Materials Performance*, 28(4), 46-50.
- Xia, Z., Chou, K. C., & Szklarska-Smialowska, Z. (1989). Pitting corrosion of carbon steel in CO<sub>2</sub>-Containing NaCl brine. *Corrosion*, 45(8), 636-642.
- Yang, Y., Brown, B., & Nescic, S. (2008). *Application of EQCM to the study of CO<sub>2</sub> corrosion*. Paper presented at the 17th International Corrosion Congress, paper no. 4071.
- Yang, Y., Brown, B., Nescic, S., Gennaro, M. E., & Molinas, B. (2010). *Mechanical strength and removal of a protective iron carbonate layer formed on mild steel in CO<sub>2</sub> corrosion*. Paper presented at the NACE Corrosion/10, paper no. 10383.

## **APPENDIX A: ADDITIONAL TESTS OF MECHANICAL EFFECT OF FLOW CONDUCTED WITH ROTATING CYLINDER ELECTRODE<sup>4</sup>**

In addition to the tests shown in section 4.2, more results were obtained from the tests conducted in glass cell with the rotating cylinder electrode setup. Details are shown in the following chapter.

### **A.1 Experimental method**

#### *A.1.1 Test setup*

Tests were conducted using the same setup as shown in section 4.2.

#### *A.1.2 Test procedure*

The experimental procedure used in these tests was similar to the one shown in section 4.2. The only difference is that the solution pH was adjusted by adding deaerated hydrochloric acid after iron carbonate layer formation and right before the increase of the rotating speed to control the supersaturation of the solution just slightly supersaturated ( $SS \approx 2$ ).

#### *A.1.3 Test matrix*

Test matrix of the iron carbonate layer removal tests are shown in Table 16.

---

<sup>4</sup> The work presented in this section was published in the co-authored paper (Han, et al., 2007).

Table 16 Test matrix for layer formation and removal tests.

Parameter	Layer formation	Layer removal
Material	C1018 carbon steel	
Solution	1 wt% NaCl	
Temperature	80°C	
CO <sub>2</sub> partial pressure	0.52 bar	
pH	6.3	6.1
Supersaturation of FeCO <sub>3</sub>	300	2
Rotating speed	0	1000 rpm, 7000 rpm

## A.2 Results and discussion

The change of corrosion rate and corrosion potential during iron carbonate layer formation and removal process is shown in Figure 91. Corrosion rate decreased after additional ferrous ion source was added to the solution to reach supersaturation of 300. As the protective layer developed, corrosion rate kept decreasing and corrosion potential increased. Saturation level of the solution also decreased (to SS of 8) due to the consumption of ferrous ion. After the corrosion rate decreased to less than 0.1 mm/year, layer formation was finished and the solution pH was adjusted to reach saturation level of 2. Then the rotating speed was increased to 1000 rpm (wall-shear stress 2 Pa). Clearly it was shown that corrosion rate decreased due to the loss of protection from iron carbonate layer. As the test continued, the corrosion rate kept increasing and saturation level also increased due to the released ferrous ion from steel corrosion. After about 10 hours, the

increase of corrosion rate slowed down, which was because no more iron carbonate was removed and it even reformed due to the increased saturation level.

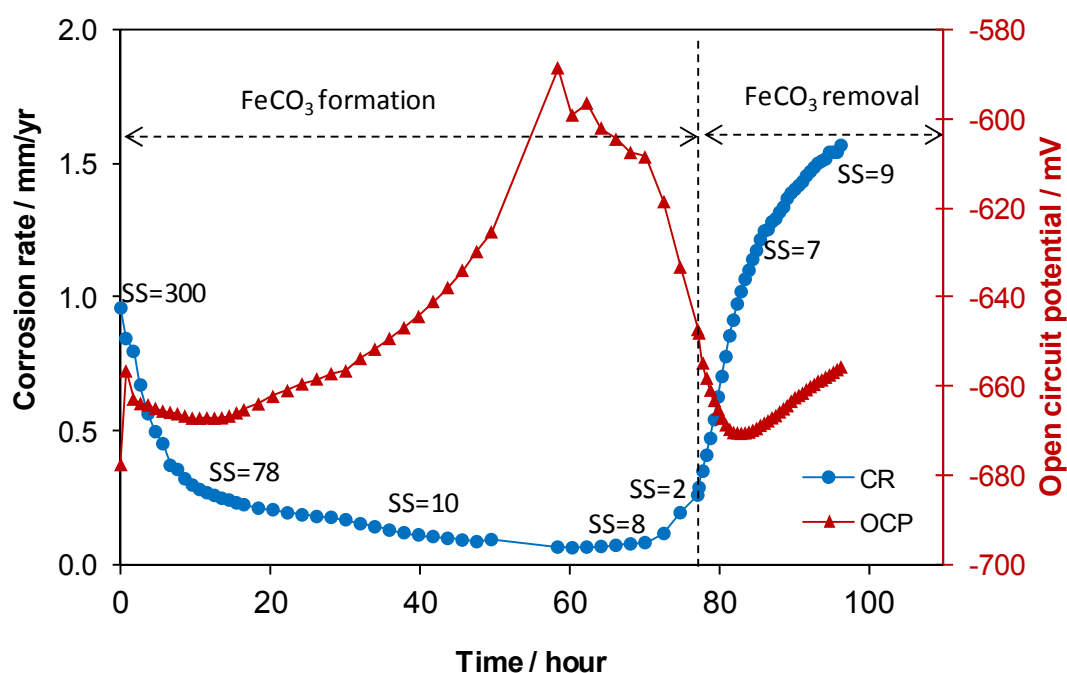


Figure 91. Change of corrosion rate and corrosion potential during protective iron carbonate layer formation and mechanical removal test, layer formation: initial pH 6.3, initial SS=300, stagnant; layer removal: initial pH 6.1, initial SS=2, 1000 rpm, T=80°C, pCO<sub>2</sub>=0.53 bar, 1 wt% NaCl.

The above analysis was confirmed by the comparison of SEM images before and after the increase of rotating speed, as shown in Figure 92 and Figure 93. It can be seen that there was much less iron carbonate remaining on the surface of the steel after exposure to flow, indicating that the increase of the corrosion rate in Figure 91 was due to the partial removal of the protective layer.

More tests were conducted with the same procedure at different rotating speed (4000 rpm and 7000 rpm) and similar phenomenon was observed. As in these tests, protective iron carbonate layer was prone to mechanical removal even at very low flow rate (1000 rpm). The procedure of pH adjustment during the tests might have initiated dissolution of iron carbonate layer. This was confirmed from the corrosion rate increase in Figure 91 between the time of supersaturation of 8 and supersaturation of 2. Therefore the corrosion rate increase did not reflect a “pure” effect of mechanical removal.

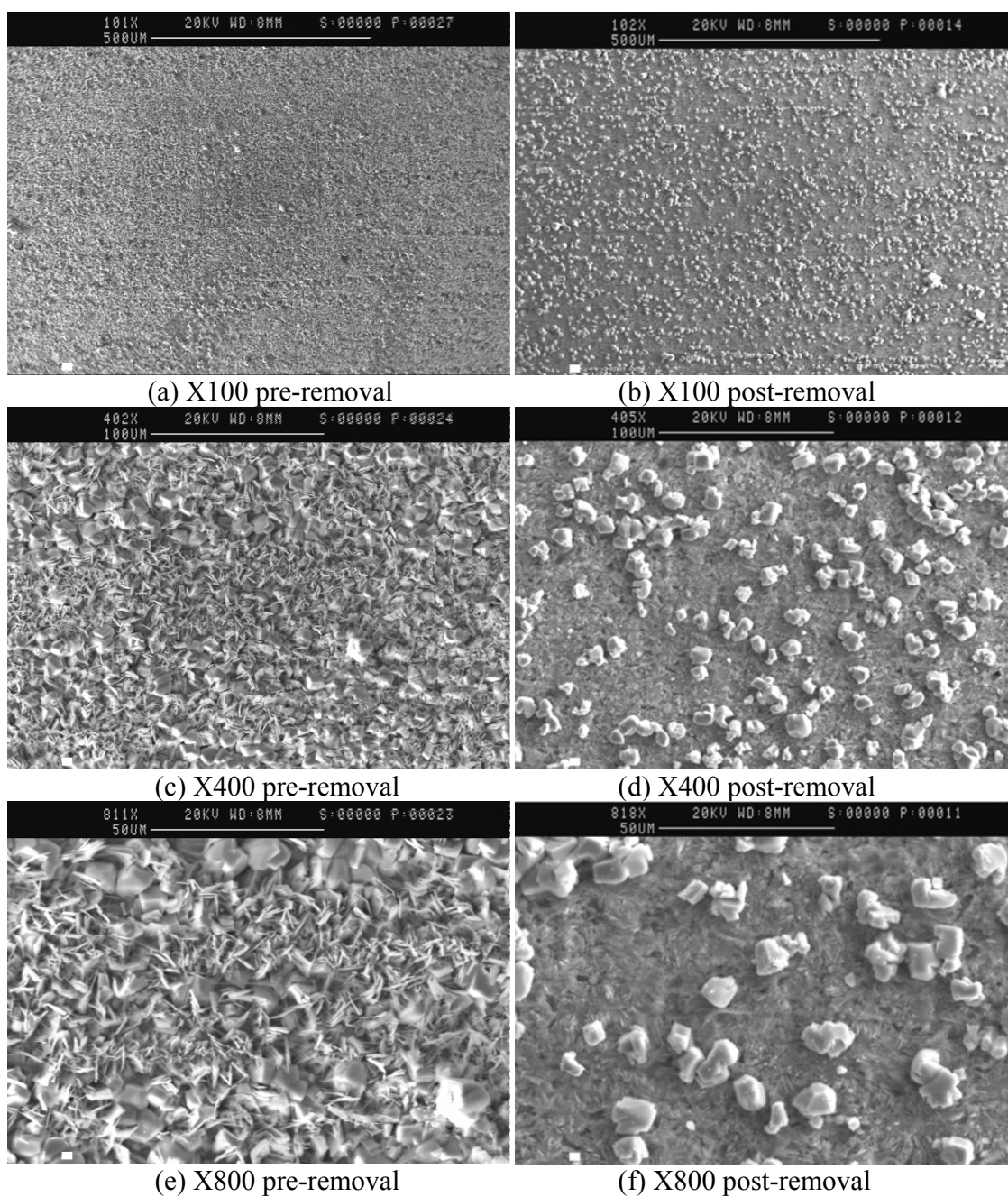


Figure 92. SEM images of top view of iron carbonate layer before and after removal process, layer formation: initial pH 6.3, initial SS=300, stagnant; layer removal: initial pH 6.1, initial SS=2, 1000 rpm, T=80°C, pCO<sub>2</sub>=0.53 bar, 1 wt% NaCl.

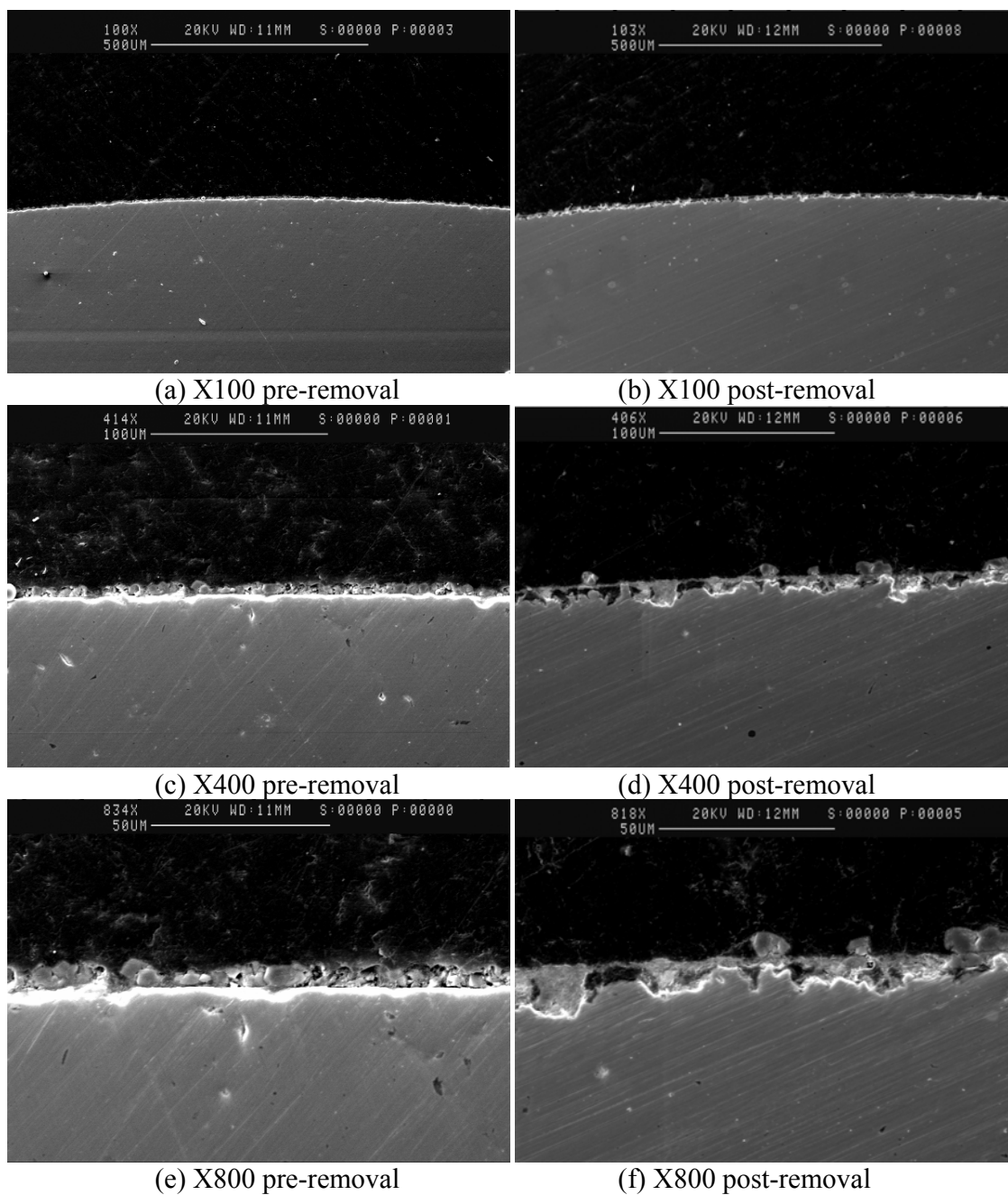


Figure 93. SEM images of cross section of iron carbonate layer before and after removal process, layer formation: initial pH 6.3, initial SS=300, stagnant; layer removal: initial pH 6.1, initial SS=2, 1000 rpm, T=80°C, pCO<sub>2</sub>=0.53 bar, 1 wt% NaCl.

**APPENDIX B: ADDITIONAL TESTS OF MECHANICAL EFFECT OF FLOW  
CONDUCTED WITH QUARTZ CRYSTAL MICROBALANCE AND JET  
IMPINGEMENT**

Experiments related to the mechanical flow effect on protective iron carbonate layer were also made in a glass cell using an EQCM and jet impingement setup, with iron coated quartz crystals.

**B.1 Experimental method**

*B.1.1 Test setup*

The test setup was the same setup as used in the iron carbonate dissolution study described in section 5.4.

*B.1.2 Test procedure*

A 1 wt% NaCl solution was prepared, deaerated with CO<sub>2</sub>, and heated to 80°C. Solution pH was adjusted to 6.6 by adding deaerated NaHCO<sub>3</sub> solution. The quartz crystal surface was cleaned using N<sub>2</sub> before being installed on crystal holder. The crystal was immersed into the solution after the frequency of quartz crystal gets stable in air. Specific amount of additional Fe<sup>2+</sup> was added to the solution according to the test matrix. The frequency change of the quartz crystal was recorded and potentiostat was used to measure the corrosion rate and corrosion potential with LPR. When the layer formation process finished, jet impingement speed was then adjusted to desired velocity. When the change of mass measured by EQCM got stable, the experiment was stopped and the crystal was taken out for surface analysis using SEM and EDS.

*B.1.3 Test matrix*

Test matrix of the iron carbonate layer removal tests are shown in the Table 17.

Table 17. Test matrix for layer formation and removal test with iron coated quartz crystal.

Parameter	Layer formation	Layer removal
Material	Iron coated quartz crystals	
Solution	1 wt% NaCl	
Temperature	80°C	
CO <sub>2</sub> partial pressure	0.52 bar	
pH	6.6	6.6
Supersaturation of FeCO <sub>3</sub>	600	Slightly saturated
Jet impingement velocity	0	4.7 m/s

## B.2 Results and discussion

Figure 94 shows the result of the iron carbonate layer formation and removal test. The mass increased and then became stable due to iron carbonate formation on the iron coated quartz crystal surface. The supersaturation of iron carbonate decreased but still remained above saturation. Then the jet flow with 4.7 m/s velocity was started. The mass started to decrease corresponding to the layer removal by the jet impingement. At the end of the test, the mass became stable and it was noticed that the mass change ended with a negative value. This means that during the iron carbonate layer removal, the iron underneath the layer was exposed to the flow and corroded away.

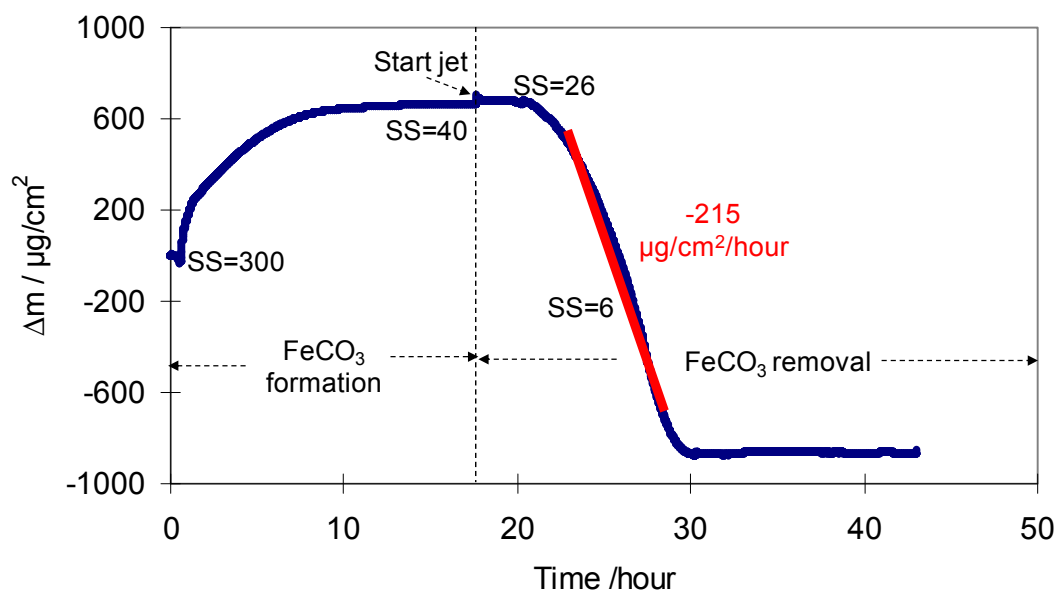


Figure 94. Mass change during iron carbonate layer formation and removal test with EQCM and jet impingement, layer formation: pH 6.6, initial SS=300; layer removal: pH 6.6, slightly supersaturated, jet velocity 4.7 m/s.

Figure 95 shows the corrosion rate and corrosion potential during the test. It can be seen that corrosion rate decreased rapidly as a layer of iron carbonate formed on the surface. After the jet impingement flow was started, corrosion rate increased, which indicated that the iron underneath the iron carbonate layer started to corrode at a higher corrosion rate. Therefore, the mass decrease on the crystal surface observed during layer removal process was not only due to the loss of iron carbonate layer, but also because of the corrosion of iron underneath the layer. The layer removal rate can be calculated by subtracting the mass loss due to corrosion, as measured by LPR, from the total mass loss. However, the measurement of corrosion rate was proven to be not reliable probably due to its small thickness and uneven corrosion.

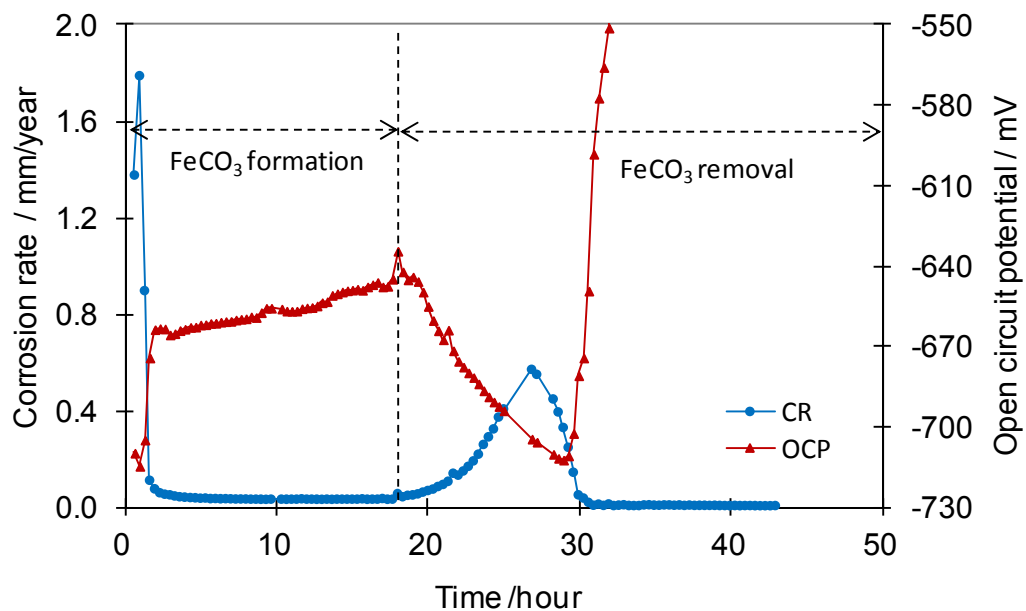


Figure 95. Change of corrosion rate and corrosion potential during iron carbonate layer formation and removal test with EQCM and jet impingement, layer formation: pH 6.6, initial SS=300; layer removal: pH 6.6, slightly supersaturated, jet velocity 4.7 m/s.

Figure 96 shows the EDS analysis of the quartz crystal surface after the test, and it proved that the entire iron carbonate layer was removed and all the underlying iron has been corroded away.

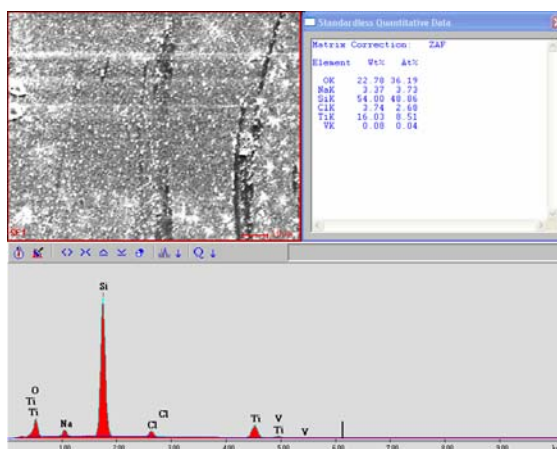


Figure 96. EDS analysis of quartz crystal surface after iron carbonate layer formation and removal test with EQCM and jet impingement, layer formation: pH 6.6, initial SS=300; layer removal: pH 6.6, slightly supersaturated, jet velocity 4.7 m/s.

Similar tests were conducted at different jet velocities (1.3 m/s and 8.4 m/s) and the same trend was observed. Although in these series of tests, the mechanical layer removal was detected and the removal rate was calculated from the mass change, there was an issue in these set of experiments which made them questionable. It remained unclear whether the adhesion force of the iron substrate to underlying quartz was greater or smaller than the adhesion force of iron carbonate layer to the iron substrate. All tests have shown that when iron carbonate layer was lost due to jet impingement, the iron substrate underlying layer was also lost. This indicates that the test results were not valid because we cannot determine the exact sequence of events. In addition this situation was complicated by the fact that the iron substrate gradually corroded away further impairing the adhesion between the iron layer and the quartz substrate as well as the iron carbonate.



**OHIO**  
UNIVERSITY

Thesis and Dissertation Services